МИСИС
УНИВЕРСИТЕТ

ISSN 1997-308X
eISSN 2412-8767

ИЗВЕСТИЯ ВУЗОВ
ПОРОШКОВАЯ МЕТАЛЛУРГИЯ И ФУНКЦИОНАЛЬНЫЕ ПОКРЫТИЯ

POWDER METALLURGY AND FUNCTIONAL COATINGS

2025
Том 19 № 6
Vol. No.
powder.misis.ru

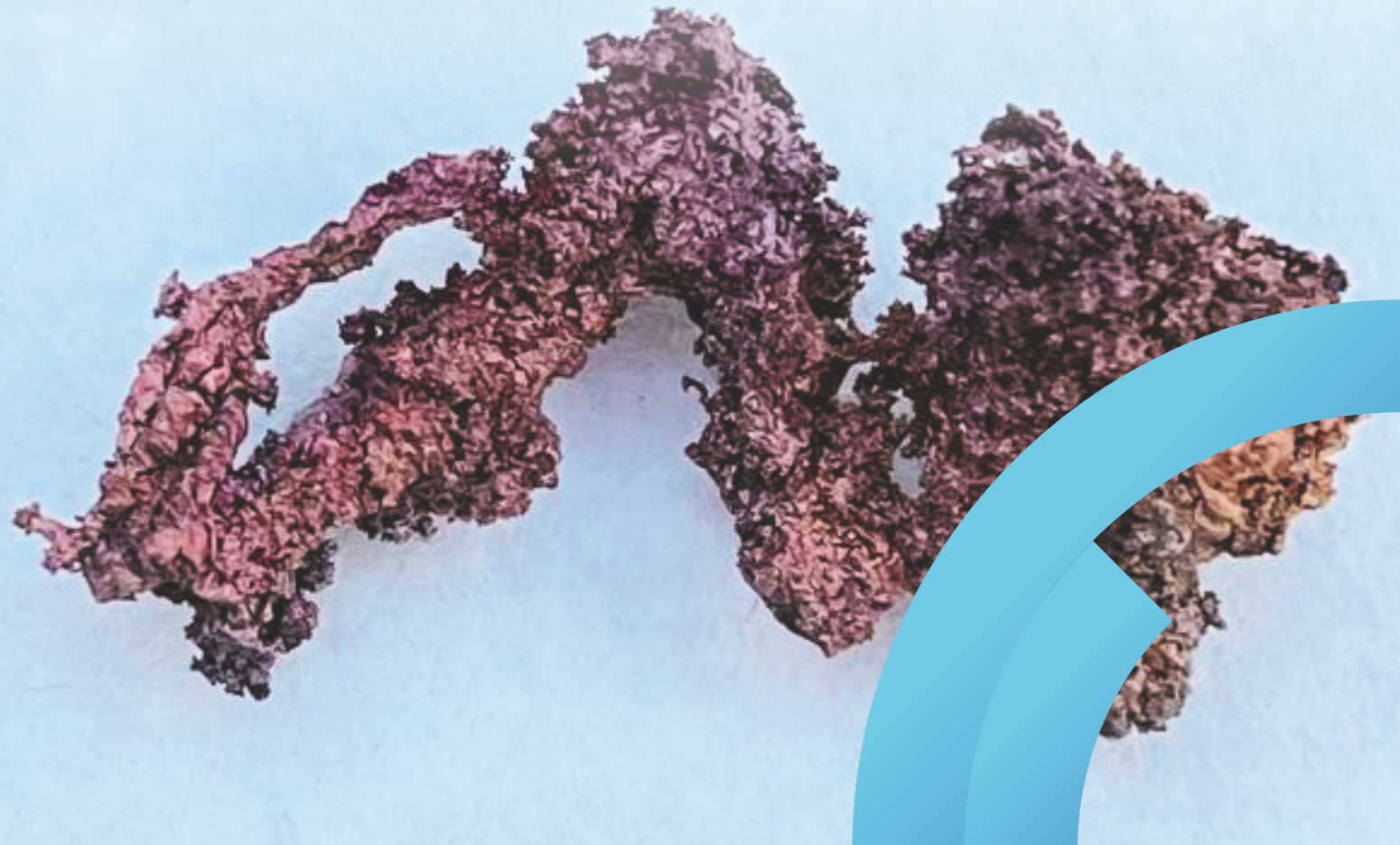

ISSN 1997-308X
eISSN 2412-8767

POWDER METALLURGY AND FUNCTIONAL COATINGS

Scientific and Technical Journal
Founded in 2007
Six issues per year

2025
Том Vol. 19 № No. 6

ИЗВЕСТИЯ ВУЗОВ ПОРОШКОВАЯ МЕТАЛЛУРГИЯ И ФУНКЦИОНАЛЬНЫЕ ПОКРЫТИЯ

Научно-технический журнал
Основан в 2007 г.
Выходит 6 раз в год

POWDER METALLURGY AND FUNCTIONAL COATINGS

ISSN 1997-308X
eISSN 2412-8767

Scientific and Technical Journal
Founded in 2007
Six issues per year

http://powder.misis.ru

Founder: MISIS University of Science and Technology

National University of Science and Technology "MISIS"
Address: 1 Bld, 4 Leninskiy Prosp., Moscow 119049, Russian Federation
http://www.misis.ru

Journal is included into the List of peer-reviewed scientific publications recommended by the Highest Attestation Commission of the Ministry of Education and Science of the Russian Federation for publishing the results of doctoral and candidate dissertations.
Abstracting/Indexing: Scopus, Russian Science Citation Index (RSCI), Ulrich's Periodicals Directory, VINITI Database (Abstract Journal).

Certificate of registration **No. FS77-27955** (12.04.2007)
Re-registration **PI No. FS77-79230** (25.09.2020)

Signed print 21.10.2025. Format 60×90 $^1/_8$
Offset paper No. 1. Digital printing. Quires 10.25
Order 23819. Free price
Printed in the printing house of the MISIS Publish House
1 Bld, 4 Leninskiy Prosp., Moscow 119049, Russian Federation
Phone/fax: +7 (499) 236-76-17

ИЗВЕСТИЯ ВУЗОВ
ПОРОШКОВАЯ МЕТАЛЛУРГИЯ
И ФУНКЦИОНАЛЬНЫЕ ПОКРЫТИЯ

НАУЧНО-ТЕХНИЧЕСКИЙ ЖУРНАЛ
ОСНОВАН В 2007 Г.
ВЫХОДИТ 6 РАЗ В ГОД

http://powder.misis.ru

ISSN 1997-308X
eISSN 2412-8767

Учредитель:

ФГАОУ ВО Национальный исследовательский технологический университет «МИСИС»
Адрес: 119049, Москва, Ленинский пр-т, 4, стр. 1
https://www.misis.ru

Журнал включен в Перечень рецензируемых научных изданий, рекомендованных ВАК Минобрнауки РФ для публикации результатов диссертаций на соискание ученых степеней.
Журнал включен в базы данных: Scopus, Russian Science Citation Index (RSCI), Ulrich's Periodicals Directory, РИНЦ, БД/РЖ ВИНИТИ.

Редакция журнала

Адрес: 119049, Москва,
Ленинский пр-т, 4, стр. 1. НИТУ МИСИС

Тел.: +7 (495) 638-45-35. ***Эл. почта:*** izv.vuz@misis.ru

Свидетельство о регистрации № **ФС77-27955** от 12.04.2007 г.
Перерегистрация 25.09.2020 г. **ПИ № ФС77-79230**

Ведущий редактор: О.В. Соснина
Выпускающий редактор: А.А. Кудинова
Дизайн и верстка: В.В. Расенець

Подписано в печать 21.10.2025. Формат 60×90 $^1/_8$
Бум. офсетная № 1. Печать цифровая. Усл. печ. л. 10,25
Заказ 23819. Цена свободная
Отпечатано в типографии Издательского Дома МИСИС
119049, г. Москва, Ленинский пр-т, 4, стр. 1
Тел./факс: +7 (499) 236-76-17

Contents

Содержание

Self-Propagating High-Temperature Synthesis
Самораспространяющийся высокотемпературный синтез

UDC 621.762
https://doi.org/10.17073/1997-308X-2025-6-5-15

Research article
Научная статья

Self-propagating high-temperature synthesis of TiC–CoCrNi cermet: Behavior and microstructure formation

A. S. Rogachev, A. R. Bobozhanov, N. A. Kochetov, D. Yu. Kovalev, S. G. Vadchenko, O. D. Boyarchenko, R. A. Kochetkov

Merzhanov Institute of Structural Macrokinetics and Materials Science of the Russian Academy of Sciences
8 Academician Osipyan Str., Chernogolovka, Moscow Region 142432, Russia

rogachev@ism.ac.ru

Abstract. Ceramic-metal composites (cermets) based on multicomponent phases are the newest research direction in the field of high-entropy and medium-entropy materials. Like traditional cermets, they consist of ceramic grains and a metal binder, with at least one of these phases being a high- or medium-entropy solid solution of three or more components in comparable concentrations. In this work, the possibility of producing $(100 - x)$TiC + xCoCrNi cermet in the range of $x = 0 \div 60$ wt. % by self-propagating high-temperature synthesis (SHS) is investigated for the first time. It is shown that the size of the CoCrNi binder particles added to the powder reaction mixture significantly affects the combustion patterns and the structure formation of the material. When using large granules (~1.5 mm), the combustion rate is higher compared to the combustion of mixtures with a fine binder, while the chemical compositions and combustion temperatures are similar.The relative difference in the average combustion rate increases from 30 % to two times with an increase in the binder content from 10 to 40 wt. %. This effect occurs due to the combustion wave "slippage" between the granules and is explained by the assumption of thermal micro-heterogeneity of the reacting medium. The use of a finer CoCrNi powder (~0.2÷0.5 mm) allows obtaining homogeneous macrostructure of SHS products without large cracks and chips, and a finer-grained microstructure. In this case, the interaction of the binder with the TiC ceramic phase that is forming in the SHS wave is observed, which is expressed in the dependence of the crystal cell parameter of the carbide phase on the binder content. The results can be used to control the microstructure and phase composition of multicomponent cermets obtained by the SHS method.

Keywords: self-propagating high temperature synthesis (SHS), cermet, titanium carbide, medium-entropy alloy

Acknowledgements: This research was supported by the Russian Science Foundation, project No. 25-13-00040.

For citation: Rogachev A.S., Bobozhanov A.R., Kochetov N.A., Kovalev D.Yu., Vadchenko S.G., Boyarchenko O.D., Kochetkov R.A. Self-propagating high-temperature synthesis of TiC–CoCrNi cermet: Behavior and microstructure formation. *Powder Metallurgy and Functional Coatings*. 2025;19(6):5–15. https://doi.org/10.17073/1997-308X-2025-6-5-15

Самораспространяющийся высокотемпературный синтез кермета TiC–CoCrNi: закономерности горения и структурообразования

А. С. Рогачев, А. Р. Бобожанов, Н. А. Кочетов, Д. Ю. Ковалев, С. Г. Вадченко, О. Д. Боярченко, Р. А. Кочетков

Институт структурной макрокинетики и проблем материаловедения им. А.Г. Мержанова РАН
Россия, 142432, Московская обл., г. Черноголовка, ул. Акад. Осипьяна, 8

rogachev@ism.ac.ru

Аннотация. Керамико-металлические композиты (керметы) на основе многокомпонентных фаз являются новейшим направлением исследований в области высоко- и среднеэнтропийных материалов. Как и традиционные керметы, они состоят из керамических зерен и связки (чаще всего металлической), при этом хотя бы одна из этих фаз является высоко- или среднеэнтропийным твердым раствором 3 и более компонентов в сопоставимых концентрациях. В настоящей работе впервые исследована возможность получения кермета $(100 - x)$TiC + xCoCrNi в диапазоне $x = 0 \div 60$ мас. % методом самораспространяющегося высокотемпературного синтеза (СВС). Показано, что размер частиц связки CoCrNi, которые добавляются в порошковую реакционную смесь, существенно влияет на закономерности горения и структурообразование материала. При использовании крупных гранул (~1,5 мм) скорость горения выше по сравнению с горением смесей с мелкой связкой при одинаковых химическом составе и температуре горения. Относительная разница в средней скорости горения возрастает от 30 до 100 % с увеличением содержания связки от 10 до 40 мас. %. Этот эффект возникает благодаря прохождению волны горения по реакционной смеси Ti + C между гранулами и находит объяснение в предположении тепловой микронеоднородности реагирующей среды. Использование более мелкого порошка CoCrNi (~0,2÷0,5 мм) позволяет получить однородную макроструктуру продуктов СВС без крупных трещин и сколов и более мелкозернистую микроструктуру. При этом наблюдается взаимодействие связки с формирующейся в волне СВС керамической фазой TiC, что выражается в зависимости параметра кристаллической ячейки карбидной фазы от содержания связки. Полученные результаты могут быть использованы для управления микроструктурой и фазовым составом многокомпонентных керметов, получаемых методом СВС.

Ключевые слова: самораспространяющийся высокотемпературный синтез (СВС), кермет, карбид титана, среднеэнтропийный сплав

Благодарности: Работа выполнена при поддержке Российского научного фонда, проект № 25-13-00040.

Для цитирования: Рогачев А.С., Бобожанов А.Р., Кочетов Н.А., Ковалев Д.Ю., Вадченко С.Г., Боярченко О.Д., Кочетков Р.А. Самораспространяющийся высокотемпературный синтез кермета TiC–CoCrNi: закономерности горения и структурообразования. *Известия вузов. Порошковая металлургия и функциональные покрытия*. 2025;19(6):5–15.
https://doi.org/10.17073/1997-308X-2025-6-5-15

Introduction

Over the past two decades, high-entropy materials have attracted considerable attention from materials scientists worldwide due to their unique combination of mechanical, electrical, magnetic, and other properties [1–3]. High-entropy materials are generally defined as single-phase disordered solid solutions containing five or more elements in equal or near-equal atomic concentrations [1]. Such a configuration provides high configurational (mixing) entropy, which is believed to stabilize the solid solution phase [1; 2]. Although the stabilizing effect of entropy has not been strictly proven – leading to some criticism of the term “high-entropy” – it remains a convenient designation for this new class of materials [1; 3]. The term distinguishes them from conventional multicomponent alloys, which are typically based on one or two principal elements, with the rest acting as minor alloying additions. Recent studies have revealed that alloys containing three or four principal elements (for example, CoCrFeNi or CoCrNi) can exhibit mechanical properties superior to those of five-component or more complex systems [4; 5]. Such compositions, which follow the same design principle as high-entropy materials – namely, comparable atomic concentrations of several elements in a single phase – but contain only three to four elements, are referred to as medium-entropy alloys (MEAs). Among these, the CoCrNi alloy has attracted special interest because it possesses the highest cryogenic impact toughness among all known materials [5–7]. At room temperature, its ultimate tensile strength reaches 1000 MPa with an elongation at fracture

of 70 %, and the crack-initiation fracture toughness (K_{J1c}) exceeds 200 MPa·m$^{1/2}$. At cryogenic temperatures, the mechanical performance further improves, with tensile strength exceeding 1.3 GPa, elongation of 90 %, and K_{J1c} = 275 MPa·m$^{1/2}$ [5].

Cermets (powder composite materials) based on multicomponent phases have recently emerged as a novel subclass within the family of high-entropy materials. Similar to conventional cermets, they consist of ceramic grains embedded in a metallic binder; however, in these systems, either the ceramic phase, the metallic binder, or both microstructural constituents can be high- or medium-entropy solid solutions. An example of the first approach is the $(Ti_{0.2}Zr_{0.2}Nb_{0.2}Ta_{0.2}Mo_{0.2})C_{0.8}$–Co, cermet, where the ceramic phase represents a high-entropy carbide – an equimolar solid solution of five transition-metal carbides [8]. The single-component metallic binder (Co), introduced in amounts of 7.7–15.0 vol. %, increased the fracture toughness (K_{1c}) up to 5.35 MPa·m$^{1/2}$ while maintaining high hardness (21.05 ± 0.72 GPa), making this material suitable for cutting tool applications. The influence of different metallic binders (Co, Ni, FeNi) on the properties of (Ta,Nb,Ti,V,W)C-based cermets has also been investigated, demonstrating that these materials can compete with WC-based cemented carbides in performance [9].

An example of the second approach is the SHS-derived TiC–CoCrFeNiMe cermet, where Me = Mn, Ti, or Al [10]. The content of the ductile high-entropy binder phase reached up to 50 wt. %[1], while hardness varied from 10 to 17 GPa. Using powder metallurgy techniques, other cermets with high-entropy alloy binders have been produced, such as WC–CoCrFeNiMn [11], Ti(C,N)–CoCrFeNiAl [12; 13], TiB_2–CoCrFeNiTiAl [14; 15], TiB_2–CoCrFeNiAl [16], TiB_2–TiC–CoCrFeNiTiAl [17] and other. Such materials are now recognized as a new class of cermets [18].

Finally, according to the third approach, a material of the composition (TiTaNbZr)C–TiTaNbZr as been obtained, in which both the ceramic phase (carbide) and the metallic binder are multicomponent. This material exhibits an excellent combination of mechanical properties, including a room-temperature flexural strength of 541 MPa, a compressive strength of 275 MPa at 1300 °C, and a fracture toughness of 6.93 MPa·m$^{1/2}$ [19].

The aim of the present study was to investigate the feasibility of synthesizing TiC–CoCrNi cermet by the self-propagating high-temperature synthesis method.

[1] Unless otherwise specified, all compositions are given in wt. %.

Materials and methods

Powder mixtures of the composition (100 – x) (Ti + C) + x(CoCrNi) with different binder contents (x = 0, 10, 20, 30, 40, 50, and 60 %) were prepared for the study. The following commercial powders were used: titanium grade PTM-1 (mean particle size d = 55 μm), carbon black P-804 (d = 1–2 μm), nickel NPE-1 (d = 150 μm), cobalt PK-1u (d < 71 μm), and chromium PKh-1M (d < 125 μm). The binder phase was introduced in the form of a CoCrNi alloy powder. To produce the alloy, an equiatomic mixture of powders (34.7 % Co + 30.7 % Cr + 34.6 % Ni) was loaded into steel vials of an Activator-2S planetary ball mill (Russia) together with steel grinding balls (6 mm in diameter) in a mass ratio of 20:1 (200 g of balls per 10 g of mixture). The vials were hermetically sealed and equipped with valves for vacuum pumping and gas filling. After evacuation to a residual pressure of 0.01 Pa, the vials were filled with argon to 0.6 MPa. Mechanical alloying was carried out for 60 min at a rotation speed of 694 rpm in an argon atmosphere with a rotational speed ratio between the vial and the supporting disk of K = 2. As a result of mechanical alloying, a single-phase face-centered cubic (FCC) CoCrNi alloy powder was obtained (Fig. 1, *a*) with a lattice parameter of a = 3.5697 ± 0.0017 Å. Its appearance is shown in Fig. 1, *b*.

The medium-entropy alloy powder was granulated by mixing it with a liquid binding agent – 4 % solution of polyvinyl butyral (PVB) in ethanol. The resulting paste was forced through a laboratory sieve with 1.6 mm mesh openings, dried in air for 10–12 h, and then sieved using a vibrating screen. Two fractions of granulated powder were used in the experiments. The coarse fraction (0.6–1.6 mm) was used as obtained (Fig. 1, *c*), while the fine fraction (<0.6 mm) was additionally ground in a mortar until its morphology matched that of the powder obtained directly after mechanical alloying (Fig. 1, *b*). This procedure provided two powders with markedly different particle sizes but identical phase composition (CoCrNi) and gasifying additive content (0.6–0.7 % PVB).

The reactive mixtures were prepared by mechanical mixing of Ti, C, and CoCrNi powders (fine or coarse fraction) without grinding to preserve the granule size. Cylindrical compacts (height 1.4–1.8 cm, diameter 1 cm, mass 2.5–4.0 g, porosity 40–45 %) were produced by double-sided cold pressing in detachable steel dies under a pressure of 120 kg/cm^2.

Combustion was performed in a constant-pressure chamber under argon atmosphere at P = 1 atm. The compact was placed on a boron nitride (BN) ceramic support and fixed on top with a BN ring

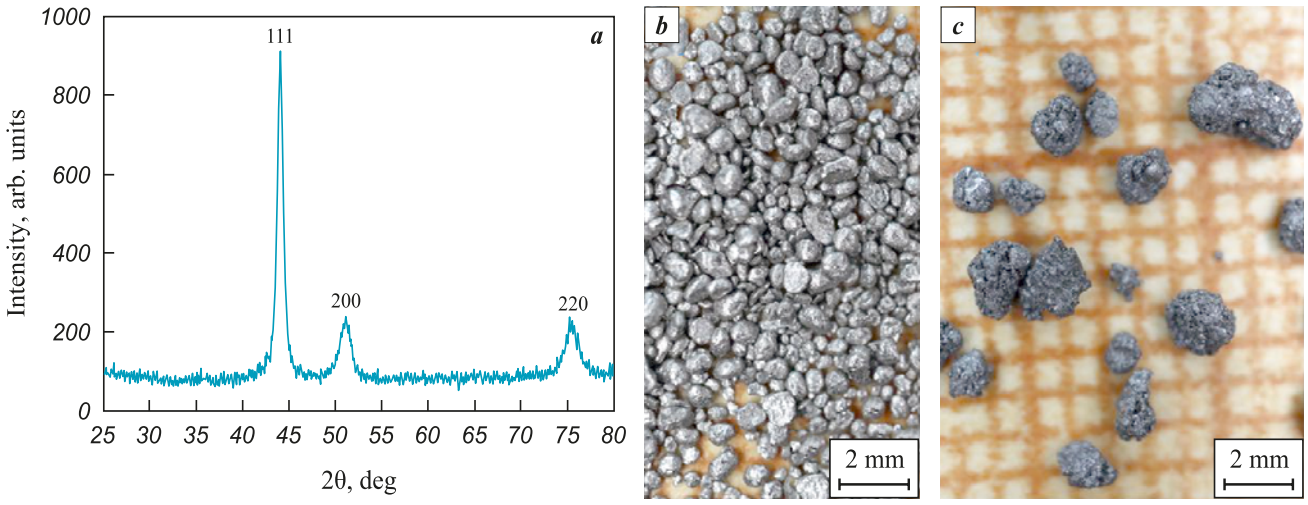

Fig. 1. *X*-ray diffraction pattern of the CoCrNi powder after mechanical alloying (***a***), its macroimage (***b***), and the appearance of the coarse granulated fraction (***c***)

Рис. 1. Рентгенограмма порошка после механического сплавления (***a***), его макрофотография (***b***) и внешний вид крупной фракции гранулированного порошка (***c***)

to prevent elongation during combustion. The SHS process was initiated at the upper surface of the compact using a heated tungsten coil through an ignition pellet of Ti + 2B composition to ensure stable ignition conditions. The process was recorded on video through a viewing window, and the average linear combustion velocity was determined frame-by-frame. The combustion temperature (T_c) was measured with a W-Re thermocouple (WR5/WR20) with a junction diameter of 0.2 mm, inserted 5 mm deep along the axis from the bottom of the compact.

Phase composition and crystal structure were analyzed using a DRON-3M *X*-ray diffractometer (Burevestnik, Russia). Microstructural observations were performed on an Ultra+ scanning electron microscope (Carl Zeiss, Germany) in secondary- and backscattered-electron modes.

Results

Fig. 2 shows the TiC samples before and after SHS. Samples produced from mixtures containing the fine CoCrNi powder binder underwent slight deformation during combustion but retained relatively homogeneous surface morphology (Fig. 2, *b*–*g*). The only exception was the sample with 10 % binder, which exhibited large surface cavities. A spiral pattern characteristic of the so-called spin combustion mode [20] appeared on the sample containing 60 % binder [20]. In contrast, all samples with coarse granulated binder powder exhibited severe cracking, with large cavities and cracks up to several millimeters long oriented along the compact axis (Fig. 2, *i*–*n*). The sample containing 60 % coarse binder burned only halfway and the reaction ceased. The differences in surface macrostructure became more evident at higher magnification (Fig. 3).

The dependences of the average linear combustion velocity on the binder content (Fig. 4, *a*) were markedly different for the fine and coarse CoCrNi powders. Compositions containing coarse granules burned significantly faster, with the relative difference in mean combustion velocity increasing from 30 to 100 % as the binder content increased from 10 to 40 %. The experimentally measured maximum temperature of the combustion products depended on the binder content but was nearly independent of the initial binder particle size introduced into the reactive mixture prior to combustion. This temperature was slightly below the calculated adiabatic value, which can be ascribed to heat losses from the compact to the fixture and the chamber environment, given the small specimen size. The combustion limit with respect to the concentration of the thermally inert binder was 50 % for the coarse granules and 60 % for the finer powder; beyond these levels, the reaction either extinguished or failed be initiated. The dependences of combustion velocity on maximum temperature deviated significantly from the theoretically predicted exponential behavior (Fig. 4, *b*). A formal estimation of the apparent activation energy from the logarithmic velocity–inverse temperature relation yielded E_a = 106 ± 14 kJ/mol for the fine CoCrNi powder and 23 ± 8 kJ/mol for the coarse powder.

The combustion front in mixtures containing the coarsely dispersed binder powder exhibited a more curved shape compared with that in mixtures containing the fine binder (Fig. 5). However, it should be noted

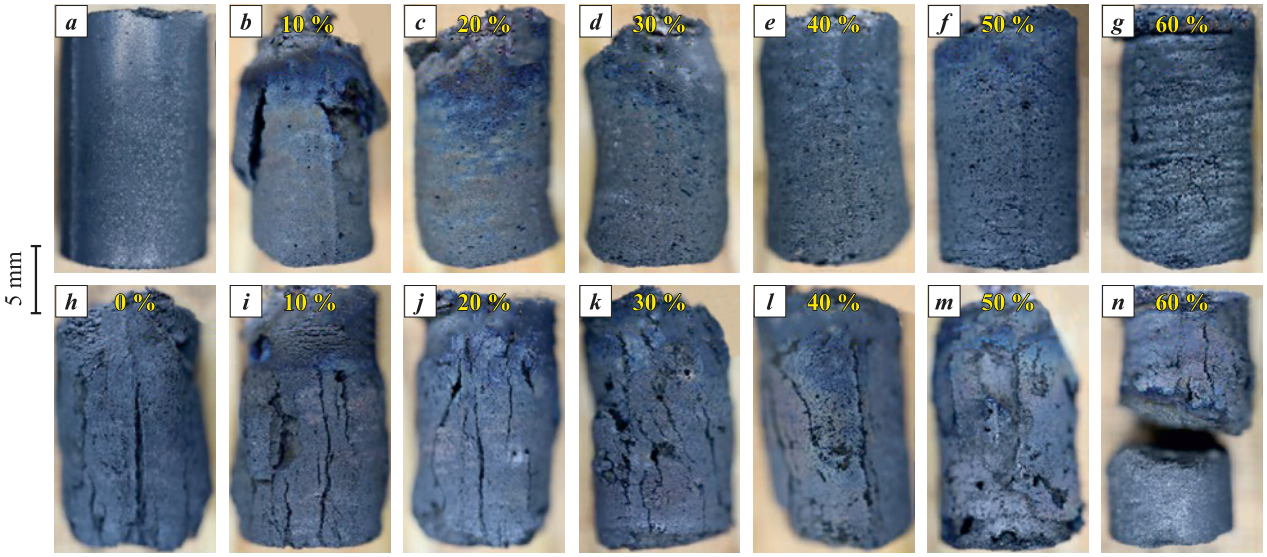

Fig. 2. Photographs of TiC samples before (***a***) and after SHS (***b***–***n***): TiC without binder (***h***); compositions with fine (***b***–***g***) and coarse (***i***–***n***) binder powders

Рис. 2. Фотографии образцов TiC – исходного (***a***) и после сгорания (***b***–***n***): TiC без связки (***h***), составы с мелкодисперсной (***b***–***g***) и крупнодисперсной (***i***–***n***) связкой

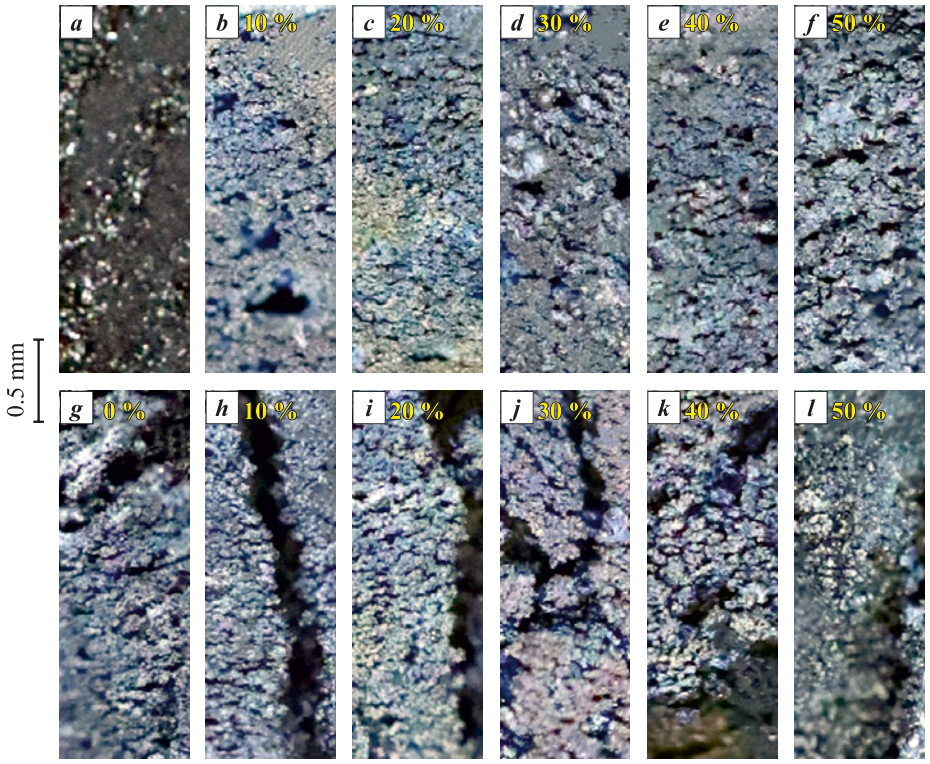

Fig. 3. Surface morphology of TiC samples before (***a***) and after SHS (***b***–***l***): TiC without binder (***g***), compositions with fine (***b***–***f***) and coarse (***h***–***l***) binder powders

Рис. 3. Фотографии поверхности образцов TiC – исходного (***a***) и после сгорания (***b***–***l***): TiC без связки (***g***), составы с мелкодисперсной (***b***–***f***) и крупнодисперсной (***h***–***l***) связкой

that front distortions and bright localized reaction zones were observed in all compositions.

X-ray diffraction analysis of the combustion products revealed two main phases: titanium carbide (FCC) and a solid solution with FCC structure corresponding to the metallic binder (Fig. 6). In samples synthesized from mixtures with fine CoCrNi powder, the relative intensity of the binder peaks increased

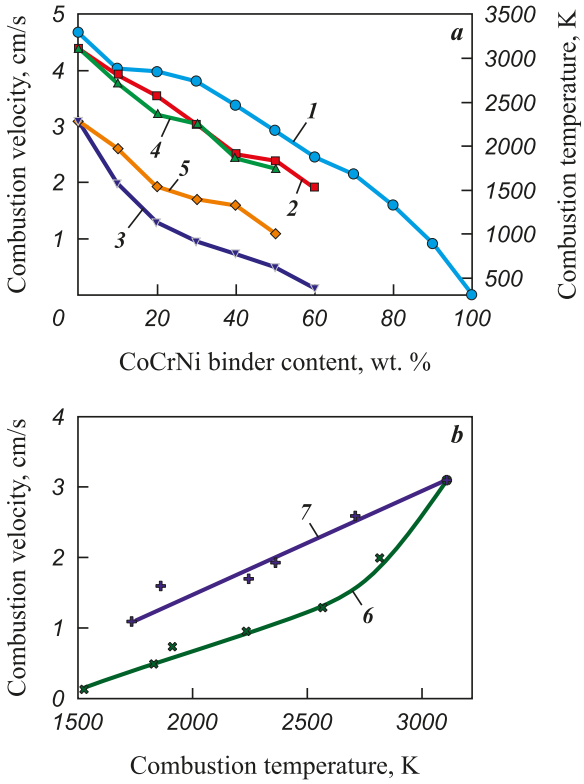

Fig 4. Dependences of combustion velocity and temperature on binder content (***a***) and combustion velocity on combustion temperature (***b***)

1 – calculated adiabatic combustion temperature; ***2*** and ***4*** – measured combustion temperatures for fine (***2***) and coarse (***4***) binders; ***3*** and ***5*** – combustion velocities for fine (***3***) and coarse (***5***) binders; ***6*** and ***7*** – combustion velocity of mixture with fine binder as a function of temperature; (***7***) – combustion velocities for fine (***6***) and coarse (***7***) binders as a function of temperature

Рис. 4. Зависимости скорости и температуры горения от содержания связки (***a***) и скорости горения от температуры процесса (***b***)

1 – расчетная адиабатическая температура горения; ***2*** и ***4*** – измеренные термопарой температуры горения смеси с мелкой (***2***) и крупной (***4***) связкой; ***3*** и ***5*** – скорости горения смеси с мелкой (***3***) и крупной (***5***) связкой; ***6*** и ***7*** – скорости горения смеси с мелкой (***6***) и крупной (***7***) связкой как функция температуры

monotonically with binder content. At high binder concentrations, weak reflections corresponding to a third phase – presumably chromium carbide – were detected in the samples (Fig. 6, *a*). In samples prepared with coarse granules, the diffraction results varied greatly: some showed almost no binder reflections, while others exhibited strong peaks from this phase. Unexpectedly, the lattice parameter of the titanium carbide phase was found to depend on the particle size of the CoCrNi powder added to the mixture (fine or coarse) (Fig. 7, *a*). This clearly indicates an interaction between the metallic binder and the ceramic TiC phase during SHS. For the metallic phase itself, despite some scatter, no significant dependence of lattice parameter on binder content was observed (Fig. 7, *b*).

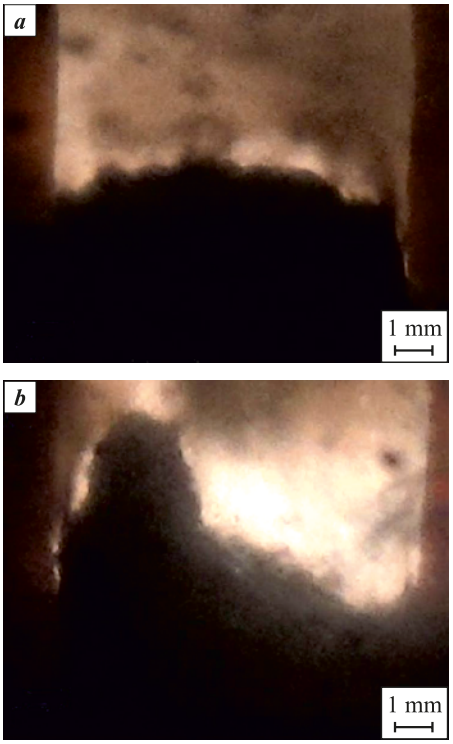

Fig. 5. Video frames of the combustion front for mixtures containing fine (***a***) and coarse (***b***) binder

Рис. 5. Видеокадры волны горения смеси с мелкой (***a***) и крупной (***b***) связкой

Microstructures of the synthesized cermets (fracture surfaces) are shown in Fig. 8 for the composition 60 % TiC + 40 % CoCrNi. Samples produced using fine medium-entropy alloy powder consisted of TiC grains 2–3 μm in size. The intergranular regions were filled with the binder phase (appearing bright in backscattered electron images, while TiC grains appeared dark due to atomic number contrast). Overall, these samples exhibited a uniform structure. In contrast, samples obtained using coarse granules contained areas with strongly varying TiC grain sizes: along with fine-grained regions, isolated areas with coarser grains (5–10 μm) were observed. The binder layers in these regions were thinner – the larger the TiC grains, the thinner the metallic binder layers, and in some cases, they were nearly absent. Since the compositions of both cermets were identical, the observed microstructural differences evidently arise from distinct combustion dynamics and structure formation mechanisms occurring behind the combustion front.

Discussion

All experimental results obtained in this study can be explained by assuming thermal micro-inhomogeneity of the reacting medium under SHS conditions. This medium consists of the exothermic Ti + C

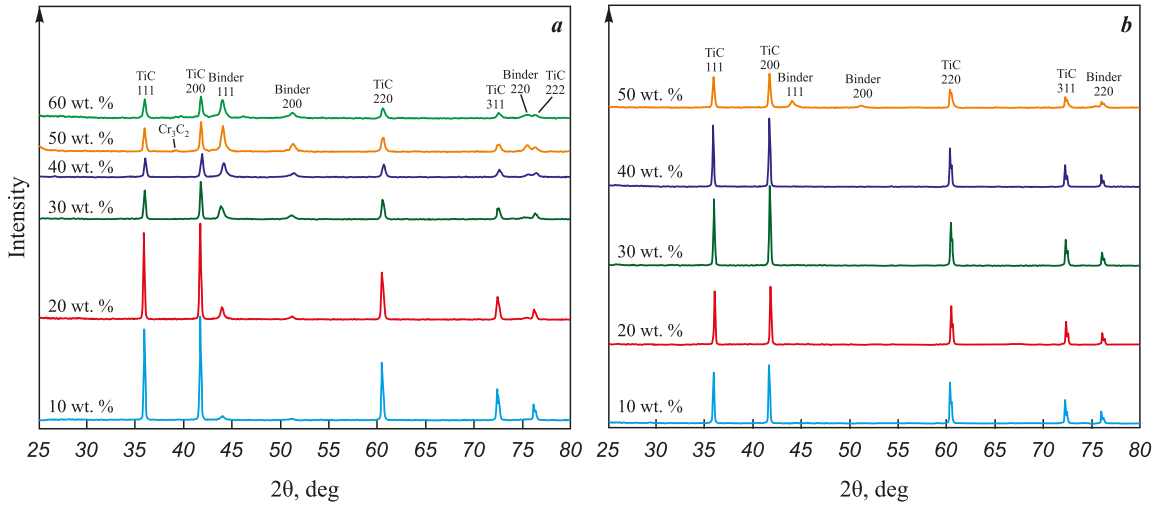

Fig. 6. *X*-ray diffraction patterns of SHS products with different binder contents introduced as fine (***a***) and coarse (***b***) granules

Рис. 6. Дифрактограммы продуктов СВС с разным содержанием связки, добавленной в виде мелких (***a***) и крупных (***b***) гранул

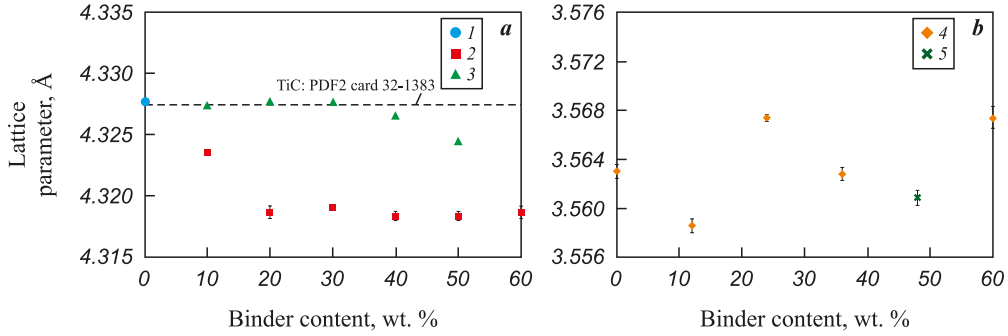

Fig. 7. Dependence of lattice parameters on binder content for titanium carbide (***a***) and metallic binder (***b***)
1 – TiC without binder; ***2–5*** – compositions with fine (***2***, ***4***) and coarse (***3***, ***5***) binder powders

Рис. 7. Зависимость параметров кристаллической решетки от содержания связки для карбида титана (***a***) и металлической связки (***b***)
1 – TiC без связки; ***2–5*** – связка вводилась в виде мелкого порошка (***2***, ***4***) и крупных гранул (***3***, ***5***)

mixture and the thermally inert diluent – the CoCrNi binder. The dependence of the combustion behavior on the particle size of the inert diluent was theoretically predicted in [21] and experimentally confirmed in [22]. The explanation of these dependencies can be summarized as follows. Fine diluent particles are completely heated within the combustion wave (in both the preheating and reaction zones) and therefore exert a strong influence on the propagation velocity of the wave. In this case, combustion proceeds under thermal homogenization conditions. In contrast, coarse diluent particles do not fully heat up within the combustion wave and thus exert a relatively weak effect on the reaction zone. The combustion wave propagates between the large particles, practically "ignoring" their presence, and the average combustion velocity in such systems is therefore higher. For example, in [22] the combustion of a Ti + C mixture diluted with chemically inert TiC particles (50 μm to 2.5 mm) was investigated. For the composition 70 % (Ti + C) + 30 % TiC, two distinct combustion modes were observed depending on the TiC particle size: at $d < 240$ μm the combustion velocity was 0.75 cm/s, then it increased and reached a new constant value of 2.4 cm/s for $d > 750$–800 μm. The dependencies obtained in the present study (Fig. 4) are consistent with these results. The main difference is that in our case, the diluent particles melt within the combustion wave and can infiltrate the pores between the TiC grains.

The effect of granulation on the combustion velocity of Ti + C and (Ti + C) + 20 % Cu compositions was studied in [23]. It was shown that the combustion velocity of granulated mixtures with a granule size of 0.6 mm was higher than that of ungranulated powder mixtures, and mixtures with 1.7 mm granules burned even faster. The explanation proposed in [23] was that impurity gases slow down combustion-front propaga-

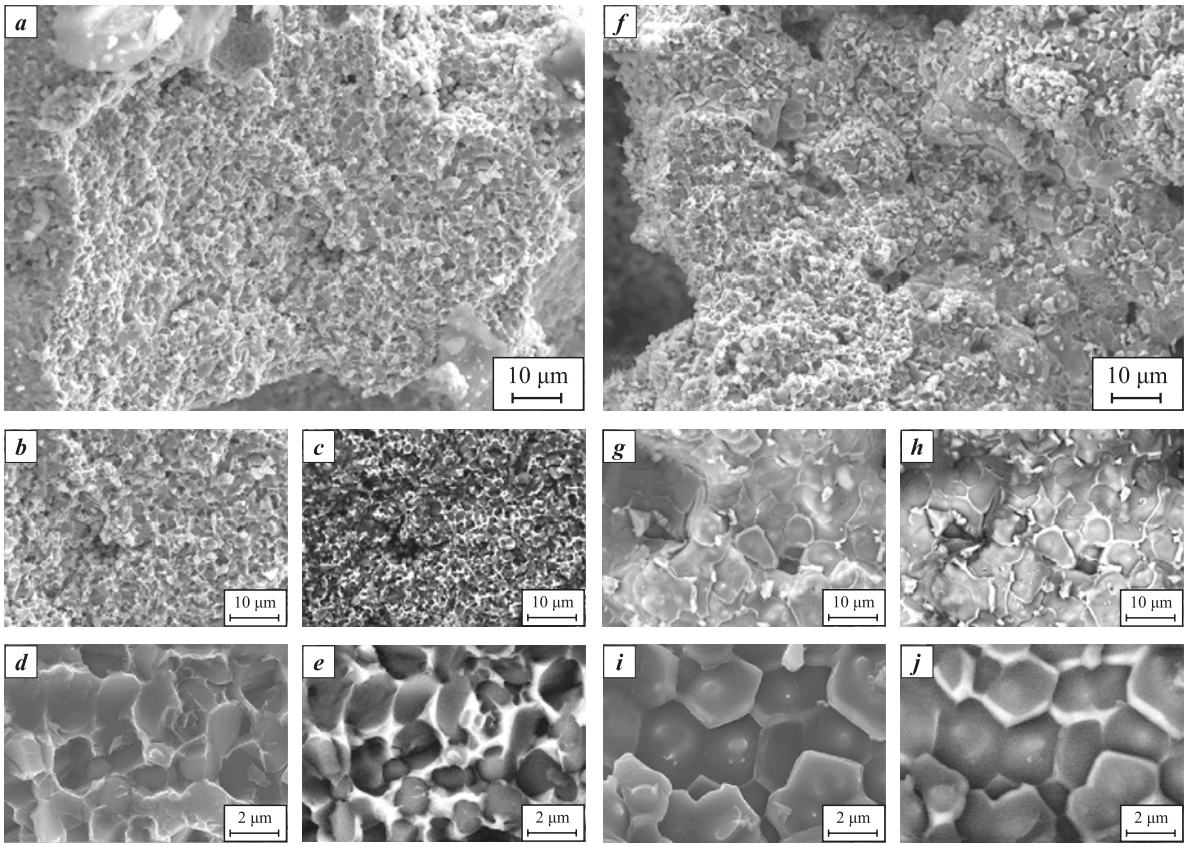

Fig. 8. Microstructures of cermets produced by SHS from reactive mixtures (60 % TiC + 40 % CoCrNi) with fine (***a***–***e***) and coarse (***f***–***j***) CoCrNi binder powder

a, ***b***, ***d***, ***f***, ***g***, ***i*** – secondary electron images; ***c***, ***e***, ***h***, ***j*** – backscattered electron images with atomic number contrast

Рис. 8. Микроструктуры керметов, полученных методом СВС из реакционных составов (60 % TiC + 40 % CoCrNi) с мелким (***a***–***e***) и крупным (***f***–***j***) порошком связки

a, ***b***, ***d***, ***f***, ***g***, ***i*** – изображения во вторичных электронах, ***c***, ***e***, ***h***, ***j*** – в обратнорассеянных электронах с контрастом по атомному номеру

tion. In the present work, however, only the inert diluent – not the entire reactive mixture – was granulated. Therefore, the increased combustion velocity in mixtures with coarse-grained diluent is more accurately explained in terms of the thermal micro-inhomogeneity model proposed in [21; 22]. It should also be noted that, in our experiments, the addition of the inert diluent led to a monotonic decrease in both combustion temperature and velocity (Fig. 4), in contrast to [23], where introducing 20 % Cu increased the combustion velocity relative to the undiluted Ti + C mixture.

Melting of particles and spreading of the resulting melts largely determine the macro- and microstructure of SHS products. Elongation of compacts and the formation of macroscopic cracks during combustion occur under the pressure of impurity gases – mainly hydrogen – released even in the combustion of nominally gas-free systems such as Ti + C [24–26]. Surface-tension (capillary) forces can counterbalance the gas pressure; in this case, the sample does not expand or crack, and in some cases may even shrink after SHS. During combustion of the Ti + C mixture, only titanium melts; the melt exists in a narrow region at the combustion front and is rapidly consumed in the reaction, forming solid TiC grains [26]. The expansion of the solid product leads to cracking (Figs. 2, *h* and 3, *g*). When fine metallic binder powder is added, it also melts in the combustion front, but the melt persists behind the front long enough for impurity gases to escape through fine pores. As a result, no cracking occurs (Figs. 2, *b*–*e* and 3, *b*–*e*). When the binder is added as coarse granules, however, they do not have time to melt and spread in the combustion zone, so the combustion wave propagates mainly through the Ti + C composition between the granules, leading to the formation of cracks (Figs. 2, *i*–*n* and 3, *i*–*m*).

The dependence of the microstructure and crystal structure of the SHS products on the particle size of the diluent is also related to the melting and spreading behavior of the metallic components. In cermet systems, the TiC grain size is determined by rapid growth behind the combustion wave, i.e., in the secon-

dary structure-formation zone [27–29]. In the undiluted Ti + C system, TiC grains grow faster than in Ti + C + metal-binder systems, since carbon diffusion in liquid Ti is faster than in Ti–Ni or similar melts (see, e.g., [27], Fig. 2.20, p. 80). Because the melting of coarse binder granules proceeds slowly, some regions between them allow the Ti + C composition to react and form relatively coarse TiC grains before the CoCrNi melt penetrates these regions. These coarse-grained areas are visible in the microstructure of the products synthesized from mixtures containing coarse binder granules (Figs. 8, *e–k*).

The TiC grains formed in these regions interact weakly with the binder; therefore, the lattice parameter of TiC remains nearly constant (4.3276 ± 0.0008 Å) when up to 30–40 % of coarse binder granules are added, being close to that of TiC synthesized without binder. When the binder is introduced as fine particles that melt directly in the reaction zone, the nucleation and growth of carbide grains occur in the Ti–Co–Cr–Ni molten bath. This results not only in a finer microstructure (Figs. 8, *a–d*) but also in the formation of a (Ti,Cr)C solid solution with a modified lattice parameter (Fig. 7, *a*). In addition, part of the carbon may react with chromium (see traces of Cr_3C_2 in Fig. 6, *a*), which decreases the carbon concentration in the main carbide phase and correspondingly reduces its lattice parameter.

Conclusion

The combustion and microstructure-formation behavior of $(100 - x)$TiC + xCoCrNi cermets (x = 0–60 %) synthesized by the self-propagating high-temperature synthesis method were investigated for the first time. It was demonstrated that the particle size of the CoCrNi binder strongly affects both the combustion process and the resulting structure. When coarse granules (~1.5 mm) were used, the combustion velocity was higher due to the “slip” of the combustion wave between the granules, and the ceramic grains were larger as a result of faster growth behind the combustion front.

The use of fine powder (~0.2–0.5 mm) produced SHS products with a more uniform macrostructure free of large cracks and chips, and with a finer microstructure. Interaction between the binder and the ceramic TiC phase formed in the SHS wave was observed. The experimentally observed regularities were explained in terms of the thermal micro-inhomogeneity of the reacting medium. The results obtained can be used to control the microstructure and phase composition of multicomponent cermets synthesized by the SHS method.

References / Список литературы

1. Miracle D.B., Senkov O.N. A critical review of high entropy alloys and related concepts. *Acta Materialia*. 2017;122:448–511. https://doi.org/10.1016/j.actamat.2016.08.081
2. Zhang Y. High-entropy materials. A brief introduction. Singapore: Springer Nature, 2019. 159 p. https://doi.org/10.1007/978-981-13-8526-1
3. Cantor B. Multicomponent high-entropy Cantor alloys. *Progress in Materials Science*. 2021;120:1–36. https://doi.org/10.1016/j.pmatsci.2020.100754
4. Gali A., George E.P. Tensile properties of high- and medium-entropy alloys. *Intermetallics*. 2013;39:74–78. https://doi.org/10.1016/j.intermet.2013.03.018
5. Gludovatz B., Hohenwarter A., Thurston K.V.S., Bei H., Wu Z., George E.P., Ritchie R.O. Exceptional damage-tolerance of a medium-entropy alloy CrCoNi at cryogenic temperatures, nature. *Communications*. 2016;7:1–8. https://doi.org/10.1038/ncomms10602
6. Laplanche G., Kostka A., Reinhart C., Hunfeld J., Eggeler G., George E. Reasons for the superior mechanical properties of mediumentropy CrCoNi compared to high-entropy CrMnFeCoNi. *Acta Materialia*. 2017;128:292–303. https://doi.org/10.1016/j.actamat.2017.02.036
7. Xu D., Wang M., Li T., Wei X., Lu Y. A critical review of the mechanical properties of CoCrNi-based medium-entropy alloys. *Microstructures*. 2022;2:1–32. https://doi.org/10.20517/microstructures.2021.10
8. Luo S.-C., Guo W.-M., Lin H.-T. High-entropy carbide-based ceramic cutting tools. *Journal of the American Ceramic Society*. 2023;106:933–940. https://doi.org/10.1111/jace.18852
9. Potschke J., Vornberger A., Gestrich T., Berger L.-M., Michaelis A. Influence of different binder metals in high entropy carbide based hardmetals. *Powder Metallurgy*. 2022;65(5):373–381. https://doi.org/10.1080/00325899.2022.2076311
10. Rogachev A.S., Vadchenko S.G., Kochetov N.A., Kovalev D.Yu., Kovalev I.D., Shchukin A.S., Gryadunov A.N., Baras F., Politano O. Combustion synthesis of TiC-based ceramic-metal composites with high entropy alloy binder. *Journal of the European Ceramic Society*. 2020;40(7):2527–2532. https://doi.org/10.1016/j.jeurceramsoc.2019.11.059
11. Velo I.L., Gotor F.J., Alcala M.D., Real C., Cordoba J.M. Fabrication and characterization of WC-HEA cemented carbide based on the CoCrFeNiMn high entropy alloy. *Journal of Alloys and Compounds*. 2018;746:1–8. https://doi.org/10.1016/j.jallcom.2018.02.292
12. Zhu G., Liu Y., Ye J., Fabrication and properties of Ti(C,N)-based cermets with multi-component AlCoCrFeNi high-entropy alloys binder. *Materials Letters*. 2013;113:80–82. https://doi.org/10.1016/j.matlet.2013.08.087
13. Zhu G., Liu Y., Ye J. Early high-temperature oxidation behavior of Ti(C,N)-based cermets with multi-component AlCoCrFeNi high-entropy alloy binder. *International Journal of Refractory Metals and Hard Materials*. 2014; 44:35–41. https://doi.org/10.1016/j.ijrmhm.2014.01.005

14. Ji W., Zhang J., Wang W., Wang H., Zhang F., Wang Y., Fu Zh. Fabrication and properties of TiB2-based cermets by spark plasma sintering with CoCrFeNiTiAl high-entropy alloy as sintering aid. *Journal of the European Ceramic Society*. 2015;35(3):879–886. https://doi.org/10.1016/j.jeurceramsoc.2014.10.024

15. Fu Zh., Koc R.. Ultrafine TiB_2–TiNiFeCrCoAl high-entropy alloy composite with enhanced mechanical properties. *Materials Science and Engineering: A*. 2017;702: 184–188. https://doi.org/10.1016/j.msea.2017.07.008

16. Zhang Sh., Sun Y., Ke B., Li Y., Ji W., Wang W., Fu Z. Preparation and characterization of TiB_2–(Supra-Nano-Dual-Phase) high-entropy alloy cermet by spark plasma sintering. *Metals*. 2018;58:1–10. https://doi.org/10.3390/met8010058

17. Fu Z., Koc R.. TiNiFeCrCoAl high-entropy alloys as novel metallic binders for TiB_2–TiC based composites. *Materials Science and Engineering: A*. 2018;735:302–309. https://doi.org/10.1016/j.msea.2018.08.058

18. A.G. de la Obra, Aviles M.A., Torres Y., Chicardi E., Gotor F.J. A new family of cermets: Chemically complex but microstructurally simple. *International Journal of Refractory Metals and Hard Materials*. 2017; 63:17–25. https://doi.org/10.1016/j.ijrmhm.2016.04.011

19. Chen X., Wang F., Zhang X., Hu S., Liu X., Humphry-Baker S., Gao M. C., He L., Lu Y., Cui B. Novel refractory high-entropy metal-ceramic composites with superior mechanical properties. *International Journal of Refractory Metals and Hard Materials*. 2024;119:106524. https://doi.org/10.1016/j.ijrmhm.2023.106524

20. Maksimov Yu.M., Pak A.T., Lavrenchuk N.V., Naiborodenko Yu.S., Merzhanov A.G. Spin combustion of gasless systems. *Fizika goreniya i vzryva*. 1979;15:156–159. (In Russ.).

Максимов Ю.М., Пак А.Т., Лавренчук Н.В., Найбороденко Ю.С., Мержанов А.Г. Спиновое горение безгазовых систем. *Физика горения и взрыва*. 1979;15:156–159.

21. Shkadinsky K.G., Krishenik P.M. Stationary combustion front in a mixture of fuel and inert. *Fizika goreniya i vzryva*. 1985;21(2):52–57. (In Russ.).

Шкадинский К.Г., Кришеник П.М. Стационарный фронт горения в смеси горючего с инертом. *Физика горения и взрыва*. 1985;21(2):52–57.

22. Maslov V.M., Voyuev S.I., Borovinskaya I.P., Merzhanov A.G. On the role of dispersion of inert diluents in gasless combustion processes. *Fizika goreniya i vzryva*. 1990;26(4):74–80. (In Russ.).

Маслов В.М. Воюев С.И, Боровинская И.П. Мержанов А.Г. О роли дисперсности инертных разбавителей в процессах безгазового горения. *Физика горения и взрыва*. 1990;26(4):74–80.

23. Seplyarsky B.S., Kochetkov R.A., Lisina T.G., Vasiliev D.S. Reason for the Increasing Burning Rate of a Ti + C Powder Mixture Diluted with Copper. *Combustion, Explosion, and Shock Waves*. 2023;59(3):344–352. https://doi.org/10.1134/S0010508223030097

Сеплярский Б.С., Кочетков Р.А., Лисина Т.Г., Васильев Д.С., Причина увеличения скорости горения порошковой смеси Ti + C при разбавлении медью. *Физика горения и взрыва*. 2023;59(3):100–108.

24. Merzhanov A.G., Rogachev A.S., Umarov L.M., Kiryakov N.V. Experimental study of the gas phase formed in the processes of self-propagating high-temperature synthesis. *Fizika goreniya i vzryva*. 1997;33(4):55–64. (In Russ.).

Мержанов А.Г., Рогачев А.С., Умаров Л.М., Кирьяков Н.В. Экспериментальное исследование газовой фазы, образующейся в процессах самораспространяющегося высокотемпературного синтеза. *Физика горения и взрыва*. 1997;33(4):55–64.

25. Mukasyan A.S., Rogachev A.S., Varma A. Microscopic mechanisms of pulsating combustion in gasless systems. *AIChE Journal*. 1999;45(12):2580–2585. https://doi.org/10.1002/aic.690451214

26. Kamynina O.K., Rogachev A.S., Umarov L.M. Deformation dynamics of a reactive medium during gasless combustion. *Combustion, Explosion and Shock Waves*. 2003;39(5):548–551. https://doi.org/10.1023/A:1026161818701

Камынина О.К., Рогачев А.С., Умаров Л.М. Динамика деформации реагирующей среды при безгазовом горении. *Физика горения и взрыва*. 2003;39(5):69–73.

27. Levashov E.A., Rogachev A.S., Kurbatkina V.V., Maksimov Yu.M., Yukhvid V.I. Advanced materials and technologies of self-propagating high-temperature synthesis: Study guide. Moscow: MISIS, 2011. 378 p. (In Russ.).

Левашов Е.А., Рогачев А.С., Курбаткина В.В., Максимов Ю.М., Юхвид В.И. Перспективные материалы и технологии самораспространяющегося высокотемпературного синтеза: Учеб. пос. М.: ИД МИСИС, 2011. 378 с.

28. Rogachev A.S., Mukasyan A.S. Combustion for the synthesis of materials: introduction to structural macrokinetics (monograph). Moscow: Fizmatlit, 2012. 398 p. (In Russ.).

Рогачев А.С., Мукасьян А.С. Горение для синтеза материалов: введение в структурную макрокинетику (монография). М.: Физматлит, 2012. 398 с.

29. Borovinskaya I.P., Gromov A.A., Levashov E.A., Maksimov Yu.M., Mukasyan A.S., Rogachev A.S. (eds.). Concise encyclopedia of SHS. Netherlands, Amsterdam: Elsevier, 2017. 438 p.

Information about the Authors

Alexander S. Rogachev – Dr. Sci. (Phys.-Math.), Professor, Chief Researcher, Laboratory of Microheterogeneous Process Dynamics, Merzhanov Institute of Structural Macrokinetics and Materials Science, Russian Academy of Sciences (ISMAN)
ORCID: 0000-0003-1554-0803
E-mail: rogachev@ism.ac.ru

Anis R. Bobozhanov – Postgraduate Student, Junior Researcher, Laboratory of Microheterogeneous Process Dynamics, ISMAN
ORCID: 0009-0008-7021-7156
E-mail: bobozhanov.anis@mail.ru

Nikolai A. Kochetov – Cand. Sci. (Phys.-Math.), Senior Researcher, Laboratory of Microheterogeneous Process Dynamics, ISMAN
ORCID: 0000-0002-1497-6624
E-mail: kolyan_kochetov@mail.ru

Dmitry Yu. Kovalev – Dr. Sci. (Phys.-Math.), Chief Researcher, Laboratory of *X*-ray Structural Studies, ISMAN
ORCID: 0000-0002-8285-5656
E-mail: kovalev@ism.ac.ru

Sergey G. Vadchenko – Cand. Sci. (Phys.-Math.), Leading Researcher, Laboratory of Microheterogeneous Process Dynamics, ISMAN
ORCID: 0000-0002-2360-2114
E-mail: vadchenko@ism.ac.ru

Olga D. Boyarchenko – Cand. Sci. (Phys.-Math.), Researcher, Laboratory of Physical Materials Science, ISMAN
ORCID: 0000-0002-7543-7608
E-mail: boyarchenko@ism.ac.ru

Roman A. Kochetkov – Cand. Sci. (Phys.-Math.), Senior Researcher, Laboratory of Combustion of Disperse Systems, ISMAN
ORCID: 0000-0003-4364-7464
E-mail: numenor@ism.ac.ru

Сведения об авторах

Александр Сергеевич Рогачев – д.ф.-м.н., проф., гл. науч. сотрудник лаборатории динамики микрогетерогенных процессов, Институт структурной макрокинетики и проблем материаловедения им. А.Г. Мержанова Российской академии наук (ИСМАН)
ORCID: 0000-0003-1554-0803
E-mail: rogachev@ism.ac.ru

Анис Рахмонович Бобожанов – аспирант, мл. науч. сотрудник лаборатории динамики микрогетерогенных процессов, ИСМАН
ORCID: 0009-0008-7021-7156
E-mail: bobozhanov.anis@mail.ru

Николай Александрович Кочетов – к.ф-м.н., ст. науч. сотрудник лаборатории динамики микрогетерогенных процессов, ИСМАН
ORCID: 0000-0002-1497-6624
E-mail: kolyan_kochetov@mail.ru

Дмитрий Юрьевич Ковалев – д.ф.-м.н., гл. науч. сотрудник лаборатории рентгеноструктурных исследований, ИСМАН
ORCID: 0000-0002-8285-5656
E-mail: kovalev@ism.ac.ru

Сергей Георгиевич Вадченко – к.ф-м.н., вед. науч. сотрудник лаборатории динамики микрогетерогенных процессов, ИСМАН
ORCID: 0000-0002-2360-2114
E-mail: vadchenko@ism.ac.ru

Ольга Дмитриевна Боярченко – к.ф.-м.н., науч. сотрудник лаборатории физического материаловедения, ИСМАН
ORCID: 0000-0002-7543-7608
E-mail: boyarchenko@ism.ac.ru

Роман Александрович Кочетков – к.ф-м.н., ст. науч. сотрудник лаборатории горения дисперсных систем, ИСМАН
ORCID: 0000-0003-4364-7464
E-mail: numenor@ism.ac.ru

Contribution of the Authors

A. S. Rogachev – defining the aim and concept of the study, literature analysis, writing and revising the manuscript.
A. R. Bobozhanov – searching and analyzing literature sources, participation in alloy preparation, writing part of the manuscript.
N. A. Kochetov – conducting SHS experiments with Ti + C + (CoCrNi) mixtures, obtaining combustion products, measuring combustion velocity and maximum synthesis temperatures.
D. Yu. Kovalev – performing *X*-ray diffraction analysis, processing the results, and editing the manuscript.
S. G. Vadchenko – calculating thermodynamic parameters of the combustion process and the composition of the products.
O. D. Boyarchenko – analyzing the microstructure (SEM) and elemental composition (EDS) of alloy samples, participation in manuscript revision.
R. A. Kochetkov – preparing and granulating the initial mechanically activated mixtures.

Вклад авторов

А. С. Рогачев – определение цели и концепции работы, анализ источников, написание и корректировка текста статьи.
А. Р. Бобожанов – поиск литературных источников по теме, их анализ, участие в получении сплава, написание части текста.
Н. А. Кочетов – проведение экспериментов по СВС смеси Ti + C + (CoCrNi), получение продуктов горения, измерение скорости и максимальных температур синтеза.
Д. Ю. Ковалев – выполнение рентгеноструктурного анализа, обработка результатов, редактирование текста.
С. Г. Вадченко – расчет термодинамических параметров процесса горения и состава продуктов.
О. Д. Боярченко – анализ микроструктуры (СЭМ) и элементного состава (ЭДА) образцов сплава, участие в правках текста статьи.
Р. А. Кочетков – подготовка и гранулирование исходных механоактивированных смесей.

Received 29.08.2025
Revised 08.09.2025
Accepted 11.09.2025

Статья поступила 29.08.2025 г.
Доработана 08.09.2025 г.
Принята к публикации 11.09.2025 г.

Self-Propagating High-Temperature Synthesis
Самораспространяющийся высокотемпературный синтез

UDC 621.762 : 621.777 + 620.178.15 + 544.45
https://doi.org/10.17073/1997-308X-2025-6-16-26

Research article
Научная статья

Influence of mechanical activation of titanium and boron on the densification and combustion of Ti + 2B powder mixtures

Yu. V. Bogatov, **V. A. Scherbakov**

Merzhanov Institute of Structural Macrokinetics and Materials Science of the Russian Academy of Sciences
8 Akademican Osip'yan Str., Chernogolovka, Moscow Region 142432, Russia

xxbroddy@gmail.com

Abstract. The influence of mechanical activation (MA) of titanium and boron powders in a ball mill on the combustion behavior of Ti + 2B mixtures has been investigated. Experimental dependences of the combustion temperature and combustion-wave velocity on the density of compacts prepared from starting and mechanically activated powders were obtained. It was shown that the dependences of these parameters on the compact density exhibit pronounced maxima. With increasing density, the rise in combustion temperature is governed by the growth of the Ti–B reaction-interface area, whereas its subsequent decrease is associated with an increase in the Ti–Ti contact area. Mechanical activation exerts opposite effects on the reactants: it reduces the specific surface area of titanium powder, thereby decreasing the Ti–B contact area, but at the same time destroys the arch-like structure of amorphous boron and disperses its agglomerates, which increases the reaction-interface area. The overall result is an increase in the maximum combustion temperature to 2900 °C. It was experimentally established that, at compaction pressures above 30 MPa, mechanically activated boron exhibits limited plasticity, enabling consolidation of Ti + 2B mixtures to relative densities of 0.7–0.8. A correlation was found between electrical resistivity and combustion temperature: the highest combustion temperatures correspond to a resistivity range of $R \approx 10^{5.0} – 10^{5.5}$ Ω·cm, while a further decrease in resistivity – related to the growth of the Ti–Ti contact area – leads to a reduction in the combustion temperature.

Keywords: mechanical activation, titanium and boron powders, powder properties, compaction, Ti + 2B reactive mixture, combustion temperature, combustion-wave velocity

For citation: Bogatov Yu.V., Scherbakov V.A. Influence of mechanical activation of titanium and boron on the densification and combustion of Ti + 2B powder mixtures. *Powder Metallurgy and Functional Coatings*. 2025;19(6):16–26. https://doi.org/10.17073/1997-308X-2025-6-16-26

Влияние механической активации титана и бора на уплотнение и горение смесей Ti + 2B

Ю. В. Богатов, **В. А. Щербаков**

Институт структурной макрокинетики и проблем материаловедения им. А.Г. Мержанова РАН
Россия, 142432, Московская обл., г. Черноголовка, ул. Акад. Осипьяна, 8

xxbroddy@gmail.com

Аннотация. В работе исследовано влияние механической активации (МА) порошков титана и бора в шаровой мельнице на процесс горения в композиции Ti + 2B. Получены экспериментальные зависимости температуры и скорости горения шихтовых образцов, спрессованных из исходных и активированных реагентов. Показано, что зависимости этих параметров от плотности прессованных образцов имеют ярко выраженный максимум. Установлено, что с ростом плотности шихтовых прессовок повышение температуры горения обусловлено увеличением площади контакта между частицами титана и бора (Ti–B), а ее снижение – с увеличением площади контакта между частицами титана (Ti–Ti). Установлено, что МА оказывает разнонаправленное действие на реагенты: она снижает удельную поверхность порошка Ti, уменьшая площадь

контакта Ti–B, но одновременно разрушает аморфную структуру бора, диспергируя его агломераты, что увеличивает реакционную поверхность. Результирующим эффектом является повышение максимальной температуры горения до 2900 °C. Экспериментально обнаружено, что при уплотнении выше давления 30 МПа порошок бора после МА способен проявлять пластические свойства, что позволило консолидировать порошковые смеси Ti + 2B до плотности 0,7–0,8. Обнаружена корреляция между уровнем электрического сопротивления и температурой горения: максимальные значения температуры горения соответствовали уровню удельного электросопротивления шихтовых прессовок $R \approx 10^{5,0} – 10^{5,5}$ Ом·см, ниже которого температура горения снижалась, что связано с увеличением площади контактной поверхности между частицами титана.

Ключевые слова: механическая активация, свойства порошков титана и бора, прессование, реакционная смесь Ti + 2B, температура и скорость горения

Для цитирования: Богатов Ю.В., Щербаков В.А. Влияние механической активации титана и бора на уплотнение и горение смесей Ti + 2B. *Известия вузов. Порошковая металлургия и функциональные покрытия*. 2025;19(6):16–26. https://doi.org/10.17073/1997-308X-2025-6-16-26

Introduction

Titanium diboride, owing to its unique properties – including ultrahigh melting point, high hardness, and strong neutron absorption capability – is widely used in mechanical engineering, metallurgy, and the nuclear industry [1–7]. A promising route for producing dense TiB_2 ceramics is SHS compaction (SHS – self-propagating high-temperature synthesis) [8; 9]. However, achieving high-density TiB_2 ceramics by this method is challenging due to the insufficiently developed stage of preparing the reactive mixtures prior to synthesis. Earlier studies on obtaining dense TiB_2 focused primarily on combustion processes [10–15] and hot pressing of reaction products [16; 17]. In contrast, the preparatory treatment of reactive mixtures received limited attention, despite its substantial influence on combustion parameters, morphology, microstructure, and ceramic properties [18; 19].

It was shown in [20] that mechanical activation of the reactants increases the combustion temperature, enhances structural integrity, and reduces both residual porosity and TiB_2 grain size. Our earlier works [18; 19] demonstrated that the combustion temperature (T_c) of Ti + 2B mixtures can be increased to the adiabatic level (3190 °C [20]) by increasing the reaction interface between titanium and boron particles. The main technological approaches for increasing T_c included selecting titanium powders with a high specific surface area (1.0–1.5 m^2/g) [18] and mechanical activation of the reactants during mixing [19].

Despite these positive results, several issues concerning the conditions for preparing the reactive mixtures and the mechanisms by which these conditions affect combustion behavior remain unresolved. Changes in the characteristics of the reactants during mechanical treatment in a ball mill, as well as during compaction, and the influence of these changes on combustion parameters have not been sufficiently investigated.

The aim of the present work was to study the influence of mechanical activation of the initial reactants – titanium and boron – on the physical and technological properties and combustion behavior of Ti + 2B powder mixtures.

Materials and methods

Titanium powder grade PTM (TU 14-22-57-92) and amorphous boron powder (TU 113-12-132-83) were used in the experiments. Their characteristics – including the content of main components, oxygen and hydrogen levels, bulk density (Θ_b), tap density (Θ_t), and particle-size distribution (d) – are presented in Table 1.

Mechanical activation of the starting powders was performed in a 2.5 L ball mill at a drum rotation speed of 60 rpm, with a charge-to-ball mass ratio of M_{ch}/M_{ball} = 1:15. The milling media were ShKh15 bearing steel balls, 25 mm in diameter. Titanium and boron powders were mixed in the stoichiometric molar ratio Ti + 2B, corresponding to the following mass

Table 1. **Characteristics of the powder reactants**

Таблица 1. **Характеристики порошковых реагентов**

Reactant	Composition, wt. %			Bulk density, Θ_b, rel. units	Tap density, Θ_t, rel. units	d, μm
	Main component	[O]	[H]			
Ti	97	0.6	0.3	0.32	0.35	<50.0
B	93	4.1	0.6	0.14	0.21	<0.2

fractions in the mixtures: 69 wt. % Ti and 31 wt. % B. Mixtures were prepared using both the initial powders (Ti_{ini} and B_{ini}), and powders mechanically activated in the ball mill – titanium for 40 h (Ti_{MA}) and boron for 30 h (B_{MA}).

To avoid introducing uncontrolled changes in the powder characteristics during mixing, all mixtures were prepared by manual blending in a ceramic mortar. In total, four mixtures were obtained: *1* – ($Ti_{исх}$ + 2B_{ini}), *2* – (Ti_{MA} + 2B_{ini}), *3* – (Ti_{ini} + 2B_{MA}) and *4* – (Ti_{MA} + 2B_{MA}).

The bulk density (Θ_b) was measured according to GOST 19440-94 (ISO 3923-1-79), and the tap density (Θ_t) according to GOST 25279-93 (ISO 3953-85). Each value represents the average of 3–5 measurements. The relative increase in density after tapping was calculated as

$$\Delta\Theta_t = \frac{\Theta_t - \Theta_b}{\Theta_b} \cdot 100\ \%.$$

The relative density of the mixture was calculated using the densities of titanium (4.5 g/cm^3), amorphous boron (1.8 g/cm^3), and the theoretical density of the Ti + 2B mixture (3.08 g/cm^3).

The specific surface area of the powders was evaluated using nitrogen adsorption (BET method). The relative measurement uncertainty did not exceed 6 %. Titanium (25 g), boron (15 g), and their reactive mixtures (20 g) were compacted in a 30-mm die at pressures of 5–170 MPa to achieve a relative density of 0.50–0.88. Axial elastic springback after unloading was measured in accordance with GOST 29012-91 (ISO 4492-85).

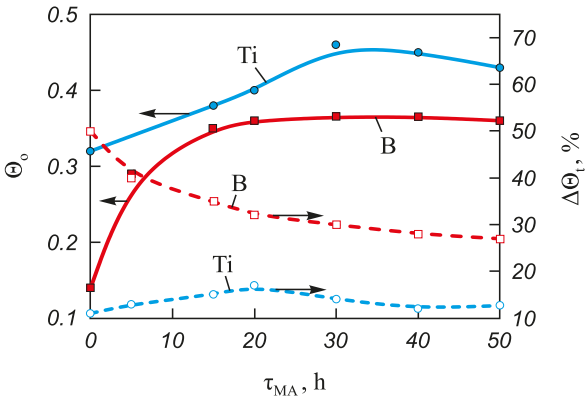

Fig. 1. Dependance of bulk density and change in tap density on mechanical activation time for Ti and B powders

Рис. 1. Зависимости насыпной плотности и изменение плотности при утряске от времени МА для порошков Ti и B

The electrical resistance (R) of the pressed samples (30 mm in diameter, 10–15 mm in height) was measured by a two-point method using a V7-40/4 digital voltmeter. Sample height served as the measurement baseline.

The maximum combustion temperature (T_{max}) and the average combustion front velocity (U_c) were determined using 200 μm tungsten–rhenium thermocouples following the methodology described in [18]. Thermocouple signals were recorded with an analog-to-digital converter and stored on a computer; the sampling frequency was 1 kHz. The reported combustion temperature and combustion velocity values represent the average of three experiments. The measurement error did not exceed 3 %.

Experimental results

Mechanical activation of titanium and boron powdera

Important characteristics of powders are the bulk density and the relative increase in density on tapping, which are governed by interparticle friction and depend on particle shape and surface roughness [21]. Their variation with mechanical activation time MA (Fig. 1).

Initially, titanium particles have a dendritic, sponge-like morphology with both open and closed porosity (Fig. 3, *a*), and a bulk density of Θ_b = 0.32. The smooth particle surface results in a minimal increase in density on tapping ($\Delta\Theta_t$ = 11 %). During treatment with the grinding media, fragmentation and smoothing of the Ti particle shape occur. In the first stage of mechanical activation (up to 20 h), two processes proceed simultaneously: milling-induced fragmentation of large sponge-like titanium particles and rounding of dendritic particles. The first process leads to a more uniform distribution of the smaller fragments between the larger particles, an increase in bulk density, and an increase in the specific surface area S_{sp} of the titanium powder (Fig. 2). The resulting irregular, angular fragments have a more defective surface compared to the starting particles, which increases $\Delta\Theta_t$ to 17 %. The second process – rounding of the Ti particles – also increases the bulk density but reduces the specific surface area of the particles. As a result, in the first stage (0–20 h of MA) the value of S_{sp} emains almost unchanged, while Θ_b and $\Delta\Theta_t$ increase (Fig. 1).

Figure 2 also shows the evolution of the electrical resistivity (R) of the titanium powder as a function of mechanical activation time. The higher initial resistivity of the starting titanium powder ($R \approx 10^{8.5}$ Ω·cm) is associated with the presence of an oxide film on

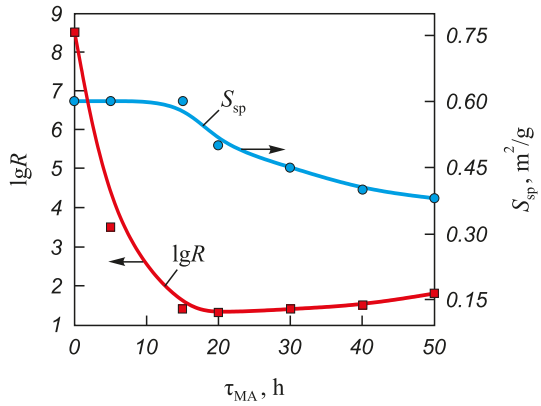

Fig. 2. Dependance of specific surface area and electrical resistivity of titanium powder on mechanical activation time

Рис. 2. Зависимости удельной поверхности и удельного электросопротивления порошка титана от времени МА

the Ti particle surface. During 5–15 h of MA this film is destroyed, which increases the true contact area between titanium particles and reduces the resistivity to $R \approx 10^{1.5}$ Ω·cm. Fragmentation of the large sponge-like Ti particles is essentially completed after 20–30 h of MA. Rounding of the titanium particles and smoothing of their shape continue, accompanied by an intensive increase in the number of surface defects (Fig. 3, *c*). As a result, the powder characteristics deteriorate: Θ_b decreases from 0.46 to 0.43, $\Delta\Theta_t$ decreases to 13 %, S_{sp} decreases to 0.35 m²/g, while R increases to $\approx 10^{1.9}$ Ω·cm in the interval from 20 to 50 h of MA (Fig. 2). This behavior is attributed to a decrease in the real contact area between titanium particles (see Fig. 1) caused by the increased defectiveness of the particle surfaces (Fig. 3, *c*).

The starting boron powder forms an arch-like packing structure, which is easily destroyed during tapping. This arching effect is associated with the formation of pores in the powder bed whose dimensions exceed the size of the largest particles. Such a packing structure results in a low bulk density of boron ($\Theta_b = 0.14$) and a high relative increase in density on tapping ($\Delta\Theta_t = 50$ %) (see Fig. 1). The starting powder contains agglomerates 1–2 μm in size composed of individual boron particles 0.1–0.3 μm in diameter (Fig. 4, *a*). As shown in our measurements, the specific surface area remains practically unchanged during interaction with the steel balls, staying within 8–9 m²/g. However, the tendency to form arch-like

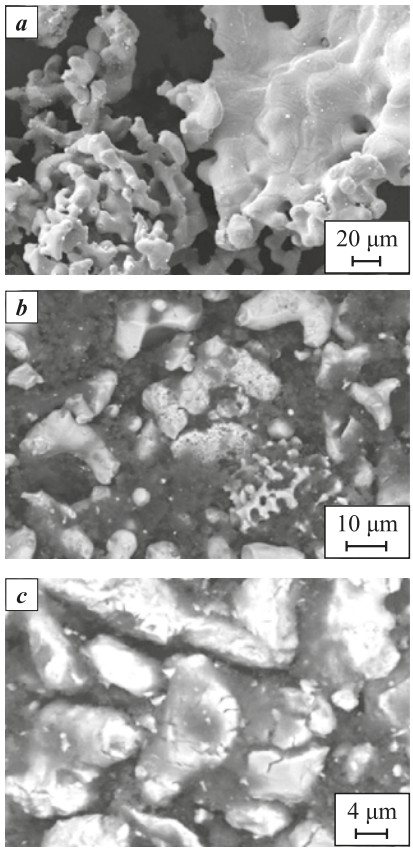

Fig. 3. Micrographs of the starting titanium powder (***a***) and after 20 h (***b***) and 50 h of (***c***) of mechanical activation

Рис. 3. Микрофотографии исходного порошка титана (***a***) и после МА 20 ч (***b***) и 50 ч (***c***)

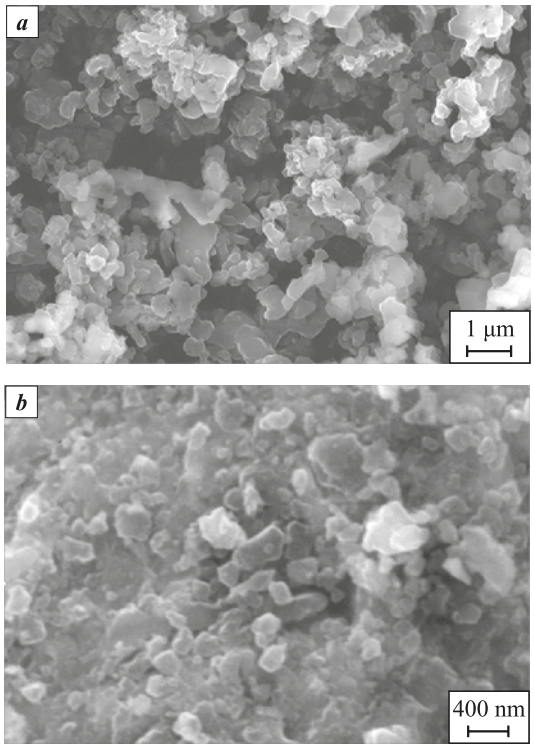

Fig. 4. Micrographs of the starting boron powder (***a***) and after mechanical activation (***b***)

Рис. 4. Микрофотографии исходного порошка бора (***a***) и после МА (***b***)

structures decreases, and the agglomerates of boron particles are gradually destroyed (Fig. 4, *b*), which reduces $\Delta\Theta_t$ to 27 % and increases Θ_b to 0.37 (Fig. 1). Individual boron particles 0.2–0.3 μm in size are visible in Fig. 4, *b*.

Compaction of elemental powders and their mixtures

Powder densification is conventionally divided into three stages [21; 22]: structural, elastic, and plastic deformation. For real powder systems this classification is approximate, and in practice the transition from structural deformation to elastoplastic deformation is usually gradual. Fig. 5 shows the dependence of density, axial elastic springback, and specific electrical resistivity of titanium compacts on the applied pressure. The compaction curve of mechanically activated titanium lies above that of the starting powder (Fig. 5, *a*). This behavior is explained by the higher bulk density of Ti_{MA} (Θ_b = 0.45), compared with Ti_{ini} (Θ_b = 0.32).

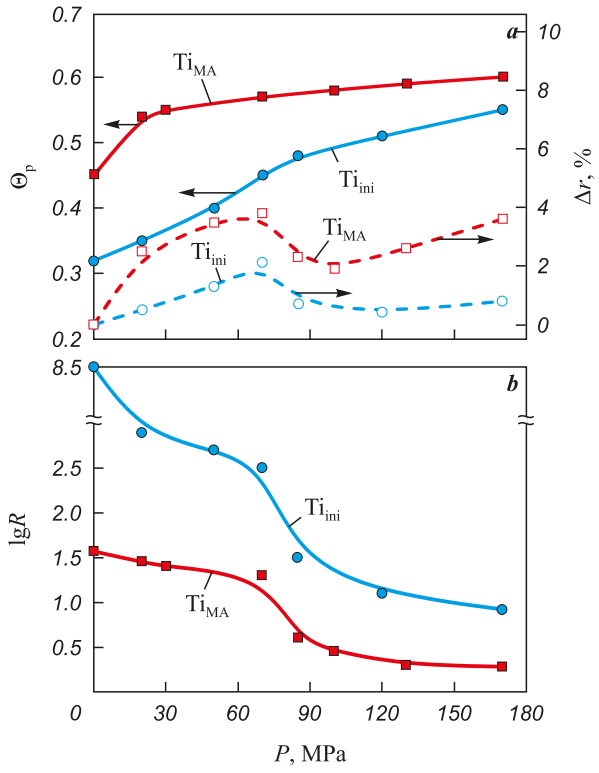

Fig. 5. Dependence of relative density and axial elastic springback (***a***), and specific electrical resistivity (***b***), on the compaction pressure for the starting and mechanically activated titanium powders

Рис. 5. Зависимости относительной плотности, упругого последействия (***a***) и удельного электросопротивления (***b***) от давления прессования порошков исходного титана и после МА

One way to determine the onset of plastic deformation is to analyze the pressure dependence of axial elastic springback (Δr) together with the compaction curve. The appearance of elastic springback with increasing compaction pressure indicates that the structural deformation stage has ended and the elastoplastic deformation stage has begun. The initial increase in Δr is caused by the accumulation of elastic stresses at interparticle contacts, where the bonding strength is still low. As the applied pressure increases and exceeds the yield strength of the particles, the plastic deformation stage begins; at this stage Δr decreases because the rate of bond strengthening between particles becomes higher than the rate of elastic stress accumulation. With further pressure increase, Δr begins to rise again, as the rate of elastic stress build-up at contacts once more exceeds the rate of bond strengthening [21].

Figure 5, *a* shows the axial springback as a function of pressure for the starting and mechanically activated titanium powders. The plastic deformation stage, indicated by a decrease in Δr, begins above 85 MPa. The higher true contact area between Ti_{MA} particles compared with Ti_{ini} results in higher elastic stresses (elastic springback). The value of Δr is determined by the contact area between titanium particles, where these stresses are generated. The larger the contact area, the higher Δr at the same compaction pressure [21].

The contact surface area between particles determines the electrical conductivity of titanium powders. Within the investigated pressure range, the electrical resistivity of Ti_{MA} compacts is lower than that of Ti_{ini} (Fig. 5, *b*), due to the rounding of the particles during mechanical activation and the resulting increase in the true contact area. At the onset of the plastic deformation stage ($P \approx 85$ MPa), a pronounced decrease in lg$R$ is observed, which is associated with the accelerated growth of the interparticle contact area (Fig. 5, *b*).

Figure 6 shows the evolution of relative density and axial elastic springback as a function of compaction pressure for the starting and mechanically activated boron powders. The compactability of B_{MA} is higher than that of B_{ini}. The shape of the Δr curve for B_{MA} corresponds to curves typical of ductile powders, such as titanium (see Fig. 5, *a*). In the range P = 30–50 MPa, a decrease in Δr is observed for B_{MA}, indicating the onset of the plastic deformation stage. With further pressure increase above 60 MPa, the elastic springback of B_{MA} rises again, similar to the behavior observed for titanium powders.

The springback curve for B_{ini} lies above that for B_{MA}. This reflects the stronger elastic response of B_{ini} during compaction. Up to about 85 MPa (Fig. 6), the compaction energy is spent mainly on breaking

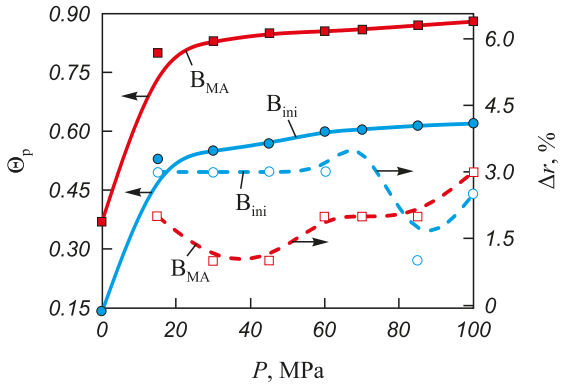

Fig. 6. Dependence of relative density and axial elastic springback on the compaction pressure for the starting and mechanically activated boron powders

Рис. 6. Зависимости относительной плотности прессовок и упругого последействия от давления прессования исходного порошка бора и после МА

the arches and agglomerates that define the structural packing of the starting boron powder. For this reason, the plastic deformation stage in B_{ini} begins later than in B_{MA}, at pressures exceeding 85 MPa.

Compaction of Ti + 2B mixtures

Titanium and boron powders – both starting and mechanically activated for 40 h (Ti_{MA}) and 30 h (B_{MA}), respectively – were used for preparing the mixtures. Since mixing in a ball mill may introduce uncontrolled changes in powder characteristics, the mixtures were blended manually in a ceramic mortar to avoid such effects.

Fig. 7 shows the evolution of relative density and axial elastic springback for compacts produced from mixtures *1–4* as a function of compaction pressure. In mixtures *1* and *2*, which contain B_{ini}, the loading volume of boron exceeds that of titanium by factors of 2.6 and 3.6, respectively (Table 2). Therefore, curves *1*, 2 and *5*, *6* are governed primarily by the elastic properties of the starting boron powder. When the volume fraction of boron is reduced in mixtures *3* and *4* (50/50 and 58/42, respectively), the mixtures can be consolidated to higher relative densities, $\Theta_p = 0.8$.

A sample calculation of the component loading volumes for mixture *1* is shown below:

- mass of Ti powder in 100 g of mixture: 69 g;
- bulk density of Ti_{ini} (Θ_{Ti}): $0.32 \cdot 4.5 = 1.44$ g/cm^3 (4.5 g/cm^3 is the density of Ti);
- titanium volume (V_{Ti}) in 100 g of mixture: 69 g / 1.44 g/cm^3 = 47.9 cm^3;
- mass of boron powder in 100 g of mixture (Ti + 2B): 31 g;
- bulk density of B_{ini} (Θ_B): $0.14 \cdot 1.8 = 0.25$ g/cm^3 (1.8g/cm^3 is the density of amorphous boron);
- boron volume (V_B) in 100 g of mixture *1*: 31 g / 0.25 g/cm^3 = 124 cm^3;
- volume ratio B/Ti in 100 g of mixture: VB/VTi = = 124 / 47.9 ≈ 2.6;
- ratio of the volume fractions of the components (B/Ti) in the mixture: 72/28 %.

The calculated values for mixtures *2–4* are presented in Table 2.

The shape of the elastic springback curves for mixtures *1* and *2* (curves *5*, *6* in Fig. 7), where one of the components is B_{ini}, indicates that elastic deformation dominates across the entire pressure range, and the plastic deformation stage is essentially absent.

Table 2. **Characteristics of mixtures *1–4***

Таблица 2. **Характеристики смесей *1–4***

Mixture No.	Composition	Θ_{Ti}, g/cm^3	Θ_B, g/cm^3	V_B/V_{Ti}	B/Ti, vol. %
1	$Ti_{ini} + 2B_{ini}$	1.44	0.25	2.6	72/28
2	$Ti_{MA} + 2B_{ini}$	2.03	0.25	3.6	78/22
3	$Ti_{ini} + 2B_{MA}$	1.44	0.67	1.0	50/50
4	$Ti_{MA} + 2B_{MA}$	2.03	0.67	1.4	58/42

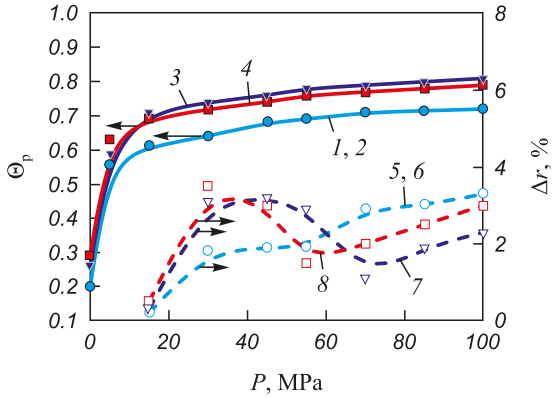

Fig. 7. Dependence of relative density (***1–4***) and axial elastic springback (***5–8***) on the compaction pressure for Ti + 2B mixtures
1, ***5*** – $Ti_{ini} + 2B_{ini}$; ***2***, ***6*** – $Ti_{MA} + 2B_{ini}$;
3, ***7*** – $Ti_{ini} + 2B_{MA}$; ***4***, ***8*** – $Ti_{MA} + 2B_{MA}$

Рис. 7. Зависимости относительной плотности (***1–4***) и упругого последействия (***5–8***) для прессовок из смесей Ti + 2B от давления прессования
1, ***5*** – $Ti_{ini} + 2B_{ini}$; ***2***, ***6*** – $Ti_{MA} + 2B_{ini}$;
3, ***7*** – $Ti_{ini} + 2B_{MA}$; ***4***, ***8*** – $Ti_{MA} + 2B_{MA}$

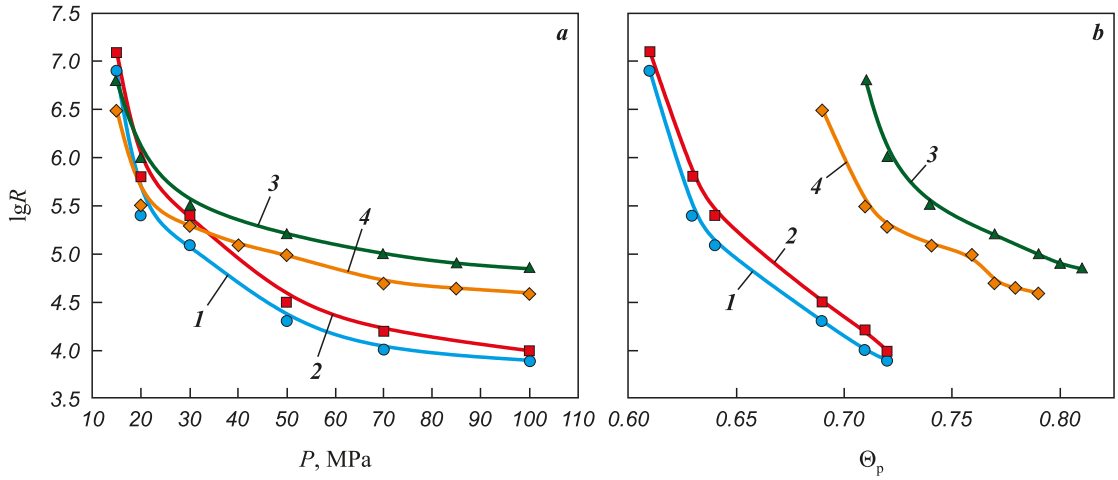

Рис. 8. Зависимости удельного электросопротивления от давления прессования (***a***) и относительной плотности смесей Ti + 2B *1–4* (***b***)

Fig. 8. Dependence of specific electrical resistivity on compaction pressure (***a***) and relative density of Ti + 2B mixtures *1–4* (***b***)

When B_{MA} is used, a decrease in Δr is observed at P = 50–70 MPa (Fig. 7), which can be interpreted as the onset of the plastic deformation stage. In this pressure interval, plastic deformation can occur only in boron particles, because the yield strength of titanium lies above 85 MPa (Fig. 5). At pressures above 30 MPa (Fig. 6), B_{MA} particles exhibit limited plasticity and may act as a lubricant during the compaction of larger titanium particles. Mixtures containing B_{MA} can be consolidated to higher relative densities, Θ_p = 0.7–0.8 (Fig. 7). This conclusion is supported by electrical resistivity measurements. As seen in Fig. 8, *b*, samples compacted from mixtures *3* and *4* exhibit higher electrical resistivity at higher densities compared with those made from mixtures *1* and *2*. This behavior is likely associated with the ability of boron – after acquiring limited plasticity as a result of mechanical activation – to spread between titanium particles at pressures above 30 MPa, thereby suppressing the growth of the Ti–Ti contact area.

Combustion of Ti + 2B mixtures

Previous studies [12; 13] have shown that the combustion temperature of Ti + 2B mixtures depends on the reaction-interface area between the starting components Ti and B: the larger the interparticle contact area, the higher the temperature within the combustion wave. The maximum attainable contact area is limited by the specific surface area of the coarser component – in this case, titanium powder (S_{sp} = 0.4–0.6 m^2/g). Therefore, the higher the specific surface area of the titanium powder, the larger the Ti–B reaction interface and the higher the combustion temperature. The reaction-interface area also depends on the density of the compacted mixtures. However, as shown in [12; 13], increasing density enhances combustion temperature only until the Ti–Ti contact area begins to grow rapidly; this enhanced heat dissipation from the reaction zone may lower the combustion temperature.

Figure 9 shows the dependence of combustion temperature and combustion-wave velocity on the relative density (Θ_p) of samples compacted from mixtures *1–4*. Samples produced from mixtures *3* and *4*, which contain B_{MA}, burn at higher temperatures ($T_{max} \approx 2800 \div 2900$ °C) The maxima of for mixtures containing B_{MA} (curves *3* and 4) occur at higher densities (Θ_p = 0.72 and 0.74) compared with mixtures containing B_{ini} (Θ_p = 0.64, curves *1* and *2*). The rise in T_c to its maximum value results from the increased Ti–B contact area with increasing density. The decrease in T_c beyond the maximum coincides, for all mixtures, with a drop in electrical resistivity below $R \approx 10^5$ Ω·cm, which indicates intensive growth of the Ti–Ti contact area (see Fig. 8). The maximum combustion temperatures for mixtures *1–4* correspond to resistivity values $\lg R \approx 5.0 \div 5.5$; at lower values of R, T_c decreases.

Fig. 9, *b* shows the combustion-wave velocities. The maxima of T_c and U_c for mixtures *3* and *4* occur at different density values, whereas for mixtures *1* and *2* both maxima coincide at Θ_p = 0.64. In the density interval $\Theta_p = 0.56 \div 0.70$, compacts *1* and *2* burn with higher velocities (9.5–10 cm/s) than compacts *3* and *4* (4.8–5.5 cm/s), which correspond to a higher density interval Θ_p (0.6–0.78).

The combustion-wave velocity is strongly affected by the conditions of off-gas escape. Increasing the com-

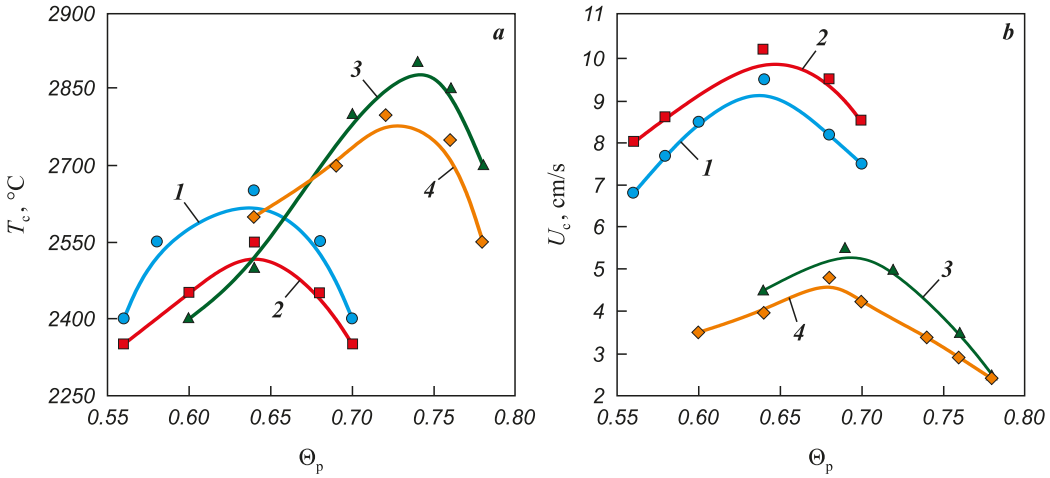

Fig. 9. Dependence of combustion temperature and combustion-wave velocity (***a***) on the relative density of samples compacted from mixtures *1–4* (***b***)

Рис. 9. Зависимости температуры и скорости горения (***a***) от относительной плотности образцов, спрессованных из смесей *1–4* (***b***)

pact density hinders removal of impurity gases released in the combustion wave, thereby reducing the combustion-wave velocity.

Discussion of results

The results demonstrate a pronounced dependence of the combustion parameters of Ti + 2B powder compacts on the conditions used for preparing the charge. The combustion temperature and combustion-wave velocity are critically important for controlling the SHS-compaction process, which ultimately governs the microstructure and properties of the resulting TiB_2 ceramic. The higher the combustion temperature – and, consequently, the temperature during hot pressing – the denser and more refined the microstructure of the TiB_2 ceramic obtained. The maximum attainable reaction-interface area between titanium and boron particles, which determines the combustion temperature, depends primarily on the specific surface area of the titanium powder. The larger this surface area, the greater the Ti–B reaction interface and the higher the combustion temperature that can be achieved during synthesis.

Mechanical activation of titanium powder in a ball mill, as shown earlier (Fig. 2), reduces its specific surface area and therefore can only decrease the combustion temperature. Thus, to achieve synthesis conditions that ensure the maximum combustion temperature, the mixing of titanium and boron powders in a ball mill must be performed under “mild” conditions, with minimal interaction between titanium and the milling media, while still ensuring homogeneous distribution of components within the mixture.

In contrast, mechanical activation of boron powder leads to the destruction of the arch-like packing structure, fragmentation of agglomerates, more homogeneous distribution of boron particles among titanium particles (as confirmed by electrical resistivity measurements, Fig. 8), and an increase in the reaction-interface area between the reactants. During compaction, B_{MA} particles act as a lubricant, allowing the charge compacts to reach relative densities of 0.70–0.75 without a significant increase in the Ti–Ti contact area ($\lg R \approx 5.0 \div 5.5$). For this reason, preliminary mechanical activation of boron before mixing with titanium yields a positive effect by increasing the combustion temperature.

The dependencies of combustion temperature and combustion-wave velocity on compact density (Fig. 9) show distinct maxima. For mixtures *1* and *2* containing B_{ini}, T_c maximum is reached at $\Theta_p = 0.64$, whereas for mixtures *3* and *4* the maxima occur at $\Theta_p = 0.72–0.74$. The electrical resistivity of the charge compacts at the combustion temperature maxima corresponds to $\lg R \approx 5.0 \div 5.5$ (Figs. 8 and 9), indicating identical Ti–Ti contact areas for all mixtures at these points. Mixtures *3* and *4*, at the same Ti–Ti contact area as mixtures *1* and 2 (as indicated by $\lg R \approx 5.0 \div 5.5$), but at higher density, likely possess a larger Ti–B reaction-interface area. Thus, maximum combustion temperatures are achieved at elevated Ti–B contact area and minimal Ti–Ti contact area. When the Ti–Ti contact area increases and the electrical resistivity drops below 10^5 Ω·cm, the combustion temperature decreases (Fig. 9, *a*). This decrease may be caused by enhanced heat removal from the reaction front, as well

as impeded off-gas evacuation due to increased compact density and the formation of closed porosity.

The combustion-wave velocity is an important technological parameter in SHS-compaction because it defines the available time window for initiating hot pressing. It was shown in [23] that U_c depends mainly on the off-gas removal conditions and only weakly on the combustion temperature (Fig. 9). The results of the present work confirm this conclusion. Although mixtures *3* and *4* exhibit higher combustion temperatures ($T_c^{max} \approx 2800$ and 2900 °C), their maximum combustion-wave velocities ($U_c^{max} \approx 4.8$ and 5.5 cm/s) are lower than those of mixtures *1* and *2* ($U_c^{max} \approx 9.5$ and 10.2 cm/s at $T_c^{max} \approx 2650$ and 2550 °C). This behavior is most likely related to the higher density of the compacts, which hinders the escape of impurity gases and therefore reduces the combustion-wave velocity. A critical density of about 0.8 was identified: compacted mixtures *3* and *4* with densities of 0.8 and higher could not be ignited.

Conclusions

1. It has been shown that preliminary mechanical activation of titanium and boron powders has a pronounced effect on the densification behavior and combustion characteristics of Ti + 2B mixtures. Mechanical activation reduces the specific surface area of the titanium powder, leading to a decrease in the Ti–B reaction-interface area and a corresponding reduction in the combustion temperature.

2. Mechanical activation of boron results in the destruction of its arch-like packing structure and fragmentation of its agglomerates, which increases the Ti–B reaction-interface area and raises the combustion temperature within the reaction front.

3. It was established that, at compaction pressures above 30 MPa, B_{MA} exhibits limited plasticity, which enables consolidation of Ti + 2B powder mixtures to relative densities of 0.7–0.8. The use of mechanically activated boron in the reactive mixtures with titanium increased the combustion temperature to 2900 °C.

4. The dependencies of combustion temperature and combustion-wave velocity on compact density exhibit distinct maxima. For mixtures containing B_{ini}, the maximum values of U_c and T_c were achieved at a relative density of 0.64. For mixtures with B_{MA}, the T_c maxima occurred at $\Theta_b = 0.72 \div 0.74$, and the U_c maximum at $\Theta_p = 0{,}68$.

5. No direct correlation between combustion temperature and combustion-wave velocity was found. Mixtures containing B_{MA} burn at a higher temperature (≈2900 °C) but with a lower combustion-wave velocity (≈5.5 cm/s) compared with mixtures containing B_{ini}, for which $T_c^{max} \approx 2650$ °C at $U_c^{max} \approx 10.2$ cm/s. The lower velocity in mixtures with B_{MA} is likely caused by hindered filtration and removal of impurity gases at higher compact densities.

6. A correlation was observed between electrical resistivity and combustion temperature: maximum T_c values correspond to a resistivity range of $R \approx 10^{5.0} – 10^{5.5}$ Ω·cm. A further decrease in resistivity below this range – associated with an increase in the Ti–Ti contact area – results in a reduction in the combustion temperature.

References / Список литературы

1. Munro R.G., Material properties of titanium diboride. *Journal of Research of the National Institute of Standards and Technology*. 2000;105(5):709–720. https://doi.org/10.6028/jres.105.057
2. Murthy T.S.R.Ch., Sonber J.K., Sairam K., Bedse R., Chakarvartty J. Development of refractory and rare earth metal borides & carbides for high temperature applications. *Materials Today: Proceedings*. 2016;3(9B):3104–3113. https://doi.org/10.1016/j.matpr.2016.09.026
3. Raju G.B., Basu B., Development of high temperature TiB_2-based ceramics. *Key Engineering Materials*. 2008;395:89–124. https://doi.org/10.4028/www.scientific.net/KEM.395.89
4. Mukhopadhyay A., Raju G.B., Basu B., Suri A.K., Correlation between phase evolution, mechanical properties and instrumented indentation response of TiB_2-based ceramics. *Journal of the European Ceramic Society*. 2009:29(3):505–516. https://doi.org/10.1016/j.jeurceramsoc.2008.06.030
5. Wang W., Fu Z., Wang H., Yuan R. Influence of hot-pressing sintering temperature and time on microstructure and mechanical properties of TiB_2 ceramics. *Journal of the European Ceramic Society*. 2002;22(7):1045–1049. https://doi.org/10.1016/S0955-2219(01)00424-1
6. Mroz C. Titanium diboride. *American Ceramic Society Bulletin*. 1995;74(6):158–159.
7. Cheloui H., Zhang Z., Shen X., Wang F., Lee S. Microstructure and mechanical properties of TiB–TiB_2 ceramic matrix composites fabricated by spark plasma sintering. *Materials Science and Engineering: A*. 2011;528(10-11):3849–3853. https://doi.org/10.1016/j.msea.2011.01.096
8. Merzhanov A.G. Solid-State Combustion. Chernogolovka: ISMAN, 2000. 224 p. (In Russ.).

   Мержанов А.Г. Твердопламенное горение. Черноголовка: ИСМАН, 2000. 224 с.
9. Pityulin A.N. Power compaction in SHS processes. In: *Selfpropagating high-temperature synthesis: Theory and practice*. Chernogolovka: Territoriya, 2001. P. 333–353. (In Russ.).

   Питюлин А.Н. Силовое компактирование в СВС процессах. В сб. науч. статей: *Самораспространяющийся*

высокотемпературный синтез: Теория и практика. Черноголовка: Территория, 2001. С. 333–353.

10. Akopyan A.G., Dolukhanyan S.K., Borovinskaya I.P. Interaction of titanium, boron and carbon in the combustion mode. *Fizika goreniya i vzryva*. 1978;(3):70–75. (In Russ.).

Акопян А.Г., Долуханян С.К., Боровинская И.П. Взаимодействие титана, бора и углерода в режиме горения. *Физика горения и взрыва*. 1978;(3):70–75.

11. Azatyan T.S., Maltsev V.M., Merzhanov A.G., Seleznev V.A. On the mechanism of propagation of the combustion wave in mixtures of titanium with boron. *Fizika goreniya i vzryva*. 1980;16(2):37–42. (In Russ.).

Азатян Т.С., Мальцев В.М., Мержанов А.Г., Селезнев В.А. О механизме распространения волны горения в смесях титана с бором. *Физика горения и взрыва*. 1980;16(2):37–42.

12. Lepakova O.K., Raskolenko L.G., Maksimov Yu.M. Investigation of titanium boride phases obtained by self-propagating high-temperature synthesis. *Neorganicheskie materialy*. 2000;36(6):690–697. (In Russ.).

Лепакова О.К., Расколенко Л.Г., Максимов Ю.М. Исследование боридных фаз титана, полученных методом самораспространяющегося высокотемпературного синтеза. *Неорганические материалы*. 2000;36(6):690–697.

13. Ponomarev M.A., Shcherbakov V.A., Shteinberg A.S. Regularities of combustion of thin layers of titanium–boron powder mixture. *Doklady AS USSR*. 1995;340(5): 642–645. (In Russ.).

Пономарев М.А., Щербаков В.А., Штейнберг А.С. Закономерности горения тонких слоев порошковой смеси титан–бор. *Доклады АН СССР*. 1995;340(5):642–645.

14. Tavadze G.F., Shteinberg A.S. Production of advanced materials by methods of self-propagating high-temperature synthesis. Berlin, Heidelberg: Springer, 2013. 156 p. https://doi.org/10.1007/978-3-642-35205-8

15. Vadchenko S.G., Boyarchenko O.D. Burning velocity of double-layer Ti + 2B strips: Influence of clearance space. *International Journal of Self-Propagating High-Temperature Synthesis*. 2018;27(2):103–106. https://doi.org/10.3103/S1061386218020164

16. Bogatov Yu.V., Levashov E.A., Blinova T.V., Pityulin A.N. Technological aspects of obtaining compact titanium diboride by SHS. *Izvestiya. Ferrous Metallurgy*. 1994;(3):51–55. (In Russ.).

Богатов Ю.В., Левашов Е.А., Блинова Т.В., Питюлин А.Н. Технологические аспекты получения компактного диборида титана методом СВС. *Известия вузов. Черная металлургия*. 1994;(3):51–55.

17. Shcherbakov V.A., Gryadnov A.N., Sachkova N.V., Samokhin A.V. SHS-compacting of ceramic composites based on titanium and chromium borides. *Pis'ma o materialakh*. 2015;5(1):20–23. (In Russ.). https://doi.org/10.22226/2410-3535-2015-1-20-23

Щербаков В.А., Грядунов А.Н., Сачкова Н.В., Самохин А.В. СВС-компактирование керамических композитов на основе боридов титана и хрома. *Письма о материалах*. 2015;5(1):20–23. https://doi.org/10.22226/2410-3535-2015-1-20-23

18. Bogatov Yu.V., Barinov V.Yu., Shcherbakov V.A. Influence of titanium powder morphology on SHS parameters and structure of compact titanium diboride. *Perspektivnye materialy*. 2020;(3):50–60. (In Russ.). https://doi.org/10.30791/1028-978X-2020-3-50-60

Богатов Ю.В., Баринов В.Ю., Щербаков В.А. Влияние морфологии порошков титана на параметры СВС и структуру компактного диборида титана. *Перспективные материалы*. 2020;(3):50–60. https://doi.org/10.30791/1028-978X-2020-3-50-60

19. Bogatov Yu.V., Shcherbakov V.A., Boyarchenko O.D. Preparation of dense TiB_2 by forced self-propagating high-temperature synthesis compaction with mechanical activation of reagents. *Inorganic Materials*. 2021;57(10):1061–1066. https://doi.org/10.1134/S0020168521100010

Богатов Ю.В., Щербаков В.А., Боярченко О.Д. Получение плотного TiB_2 методом силового СВС-компактирования с использованием механической активации реагентов. *Неорганические материалы*. 2021;57(10):1122–1127. https://doi.org/10.31857/S0002337X21100018

20. Levashov E.A., Rogachev A.S., Kurbatkina M., Yukhvid V.I. Perspective materials and technologies of self-propagating high-temperature synthesis. Moscow: MISIS, 2011. 378 p. (In Russ.).

Левашов Е.А., Рогачев А.С., Курбаткина М., Юхвид В.И. Перспективные материалы и технологии самораспространяющегося высокотемпературного синтеза. М.: Изд. дом МИСИС, 2011. 378 с.

21. Kiparisov S.S., Libenson G.A. Powder Metallurgy. Moscow: Metallurgiya. 1991. 432 p. (In Russ.).

Кипарисов С.С., Либенсон Г.А. Порошковая металлургия. М.: Металлургия. 1991. 432 с.

22. Tsemenko V.N. Deformation of powder media. SPb: SPbSTU, 2001. 104 p. (In Russ.).

Цеменко В.Н. Деформирование порошковых сред. СПб: Изд. СПбГТУ, 2001. 104 с.

23. Bogatov Yu.V., Shcherbakov V.A. Convective combustion of a mechanically activated Ti + C mixture under forced SHS compaction. *Combustion, Explosion, and Shock Waves*. 2023;59(3):353–361. https://doi.org/10.1134/S0010508223030103

Богатов Ю.В., Щербаков В.А. Конвективное горение механоактивированной смеси Ti + C в условиях силового СВС-компактирования. *Физика горения и взрыва*. 2023;59(3):109–117.

Information about the Authors

Yuri V. Bogatov – Cand. Sci. (Eng.), Senior Researcher, Laboratory of Energy-Assisted Physicochemical Processes, Merzhanov Institute of Structural Macrokinetics and Materials Science, Russian Academy of Sciences (ISMAN)
ORCID: 0000-0002-7329-2898
E-mail: xxbroddy@gmail.com

Vladimir A. Shcherbakov – Dr. Sci. (Phys.-Math.), Head of the Laboratory of Energy-Assisted Physicochemical Processes, ISMAN
ORCID: 0000-0001-5682-3792
E-mail: vladimir@ism.ac.ru

Сведения об авторах

Юрий Владимирович Богатов – к.т.н., ст. науч. сотрудник лаборатории энергетического стимулирования физико-химических процессов, Институт структурной макрокинетики и проблем материаловедения им. А.Г. Мержанова Российской академии наук (ИСМАН)
ORCID: 0000-0002-7329-2898
E-mail: xxbroddy@gmail.com

Владимир Андреевич Щербаков – д.ф.-м.н., зав. лабораторией энергетического стимулирования физико-химических процессов, ИСМАН
ORCID: 0000-0001-5682-3792
E-mail: vladimir@ism.ac.ru

Contribution of the Authors

Yu. V. Bogatov – conceptualization, experimental work, data analysis, writing and preparation of the manuscript.
V. A. Shcherbakov – discussion of the results, contribution to manuscript writing.

Вклад авторов

Ю. В. Богатов – определение цели работы, проведение экспериментов, написание статьи.
В. А. Щербаков – участие в обсуждении результатов и написание статьи.

Received 01.03.2025
Revised 20.05.2025
Accepted 23.05.2025

Статья поступила 01.03.2025 г.
Доработана 20.05.2025 г.
Принята к публикации 23.05.2025 г.

Self-Propagating High-Temperature Synthesis
Самораспространяющийся высокотемпературный синтез

UDC 621.762
https://doi.org/10.17073/1997-308X-2025-6-27-35

Research article
Научная статья

Effect of Si, Al, Cu, Cr, and $TiSi_2$ on the formation of the Ti_3SiC_2 MAX phase during self-propagating high-temperature synthesis in air

E. R. Umerov, **S. A. Kadyamov**, **D. M. Davydov**, **E. I. Latukhin**, **A. P. Amosov**

Samara State Technical University
244 Molodogvardeyskaya Str., Samara 443100, Russia

umeroff2017@yandex.ru

Abstract. This study examines how additions of Si, Al, Cu, and Cr powders to the stoichiometric 3Ti–Si–2C (at. %) charge influence the formation of the Ti_3SiC_2 MAX phase during self-propagating high-temperature synthesis (SHS) performed in air within a sand bed, without a sealed reactor or controlled atmosphere. The effect of partially or fully substituting elemental Ti and Si powders with $TiSi_2$ on the Ti_3SiC_2 yield is also assessed. Microstructural characterization of the SHS products was conducted using scanning electron microscopy equipped with energy-dispersive spectroscopy, and the phase composition was quantified by *X*-ray diffraction. An addition of 0.1 mol Si to the stoichiometric mixture increases the Ti_3SiC_2 content in the product to approximately 70 vol. %. Incorporating 0.1 mol Al decreases the Ti_3SiC_2 fraction to 39 vol. % and results in the formation of TiAl. In contrast, combining a silicon excess with 0.1 mol Al in the 3Ti–1.25Si–2C + 0.1Al system markedly enhances the Ti_3SiC_2 yield, reaching ~89 vol. %. For synthesis in the $TiSi_2$–C system, the share of the MAX phase decreases while secondary phases become more prevalent; the maximum Ti_3SiC_2 content in this system is 56 vol. %. When $TiSi_2$ fully replaces elemental silicon in the 2.5Ti–0.5$TiSi_2$–2C mixture, the Ti_3SiC_2 fraction drops to 20 vol. %.

Keywords: self-propagating high-temperature synthesis (SHS), reactorless SHS, Ti_3SiC_2 MAX phase, powders, microstructure, *X*-ray diffraction

Acknowledgements: The work was supported by the Russian Science Foundation, grant No. 24-79-10187, https://rscf.ru/project/24-79-10187/.

For citation: Umerov E.R., Kadyamov S.A., Davydov D.M., Latukhin E.I., Amosov A.P. Effect of Si, Al, Cu, Cr, and $TiSi_2$ on the formation of the Ti_3SiC_2 MAX phase during self-propagating high-temperature synthesis in air. *Powder Metallurgy and Functional Coatings*. 2025;19(6):27–35. https://doi.org/10.17073/1997-308X-2025-6-27-35

Влияние Si, Al, Cu, Cr и $TiSi_2$ на получение MAX-фазы Ti_3SiC_2 методом самораспространяющегося высокотемпературного синтеза на воздухе

Э. Р. Умеров, Ш. А. Кадямов, Д. М. Давыдов, Е. И. Латухин, А. П. Амосов

Самарский государственный технический университет
Россия, 443100, г. Самара, ул. Молодогвардейская, 244

umeroff2017@yandex.ru

Аннотация. В работе рассмотрено влияние добавок порошков Si, Al, Cu и Cr к стехиометрическому составу шихты 3Ti–Si–2C (ат. %) при получении MAX-фазы Ti_3SiC_2 в режиме самораспространяющегося высокотемпературного синтеза (СВС) на воздухе в засыпке из песка без применения закрытого реактора и специальной атмосферы или вакуума. Показано влияние частичной или полной замены элементных порошков шихты Ti и Si на $TiSi_2$ на выход Ti_3SiC_2. Проведен анализ микроструктуры полученных СВС-продуктов с помощью растрового электронного микроскопа с приставкой для энергодисперсионной спектрометрии. Исследованы качественный и количественный фазовые составы порошковых СВС-продуктов с помощью рентгеновского дифрактометра. Установлено, что добавка 0,1 моль порошка кремния к стехиометрическому составу шихты увеличивает количество MAX-фазы Ti_3SiC_2 в продукте до 70 % от объема. Введение 0,1 моль Al-порошка в исходную шихту приводит к уменьшению количества Ti_3SiC_2 до 39 % от объема и появлению новой фазы TiAl. При этом совместный избыток кремния вместе с добавкой 0,1 моль Al в системе 3Ti–1,25Si–2C + 0,1Al существенно повышают содержание Ti_3SiC_2 до ~89 об. %. Установлено, что при синтезе в системе $TiSi_2$–C в продуктах реакции доля MAX-фазы уменьшается, а количество побочных фаз возрастает. Максимальное содержание Ti_3SiC_2 в продукте при синтезе в системе $TiSi_2$–C достигает 56 % от общего объема. При увеличении количества $TiSi_2$ до полной замены элементного кремния в исходной шихте 2,5Ti–0,5$TiSi_2$–2C доля MAX-фазы Ti_3SiC_2 в продукте падает до 20 %.

Ключевые слова: самораспространяющийся высокотемпературный синтез (СВС), безреакторный синтез, MAX-фаза Ti_3SiC_2, порошки, структура, рентгенофазовый анализ

Благодарности: Исследование выполнено за счет гранта Российского научного фонда № 24-79-10187, https://rscf.ru/project/24-79-10187/.

Для цитирования: Умеров Э.Р., Кадямов Ш.А., Давыдов Д.М., Латухин Е.И., Амосов А.П. Влияние Si, Al, Cu, Cr и $TiSi_2$ на получение MAX-фазы Ti_3SiC_2 методом самораспространяющегося высокотемпературного синтеза на воздухе. *Известия вузов. Порошковая металлургия и функциональные покрытия*. 2025;19(6):27–35. https://doi.org/10.17073/1997-308X-2025-6-27-35

Introduction

The Ti_3SiC_2 MAX phase is a promising layered ternary carbide that combines key ceramic and metallic properties, including excellent oxidation resistance, high thermal and electrical conductivity, thermal-shock resistance, high-temperature plasticity, creep resistance, low density, and good machinability [1; 2]. These properties make Ti_3SiC_2 a potential alternative to conventional ceramics.

Many published synthesis approaches require expensive equipment, long high-temperature dwell times, and protective atmospheres, all of which increase the cost and complexity of MAX-phase production [3–6]. In contrast, the highly exothermic and economically efficient process of self-propagating high-temperature synthesis (SHS) significantly simplifies the fabrication route, requires no special hardware, and proceeds much faster than furnace sintering [7; 8]. A simple method for producing MAX-phase cermets was recently proposed, based on infiltrating molten metals into a porous Ti_3SiC_2 skeleton synthesized via SHS in air [9]. During Ti_3SiC_2 formation, the reaction temperature may reach 2260 °C [10], while the maximum adiabatic combustion temperature is reported to be 2735 °C [11].

Formation of Ti_3SiC_2 proceeds through several stages. Initially, TiC particles and a Ti–Si melt form simultaneously. At the next stage, TiC dissolves into the Ti–Si liquid, followed by crystallization of Ti_3SiC_2 platelets [12–14]. Because SHS evolves extremely rapidly – values below 3–4 s are typical for the first stage – post-ignition control of the process is practically impossible. Therefore, establishing optimal synthesis parameters is essential to maximize the purity of the final Ti_3SiC_2 product. Deviations from charge stoichiometry and insufficient high-temperature dwell associated with fast post-reaction cooling commonly

lead to increased fractions of secondary phases such as TiC and $TiSi_2$.

The reactions leading to TiC and the Ti–Si melt compete for the available titanium, as both intermediates form simultaneously within a single reactive system. Consequently, a deficiency of one intermediate and the excess of the other inevitably decreases the Ti_3SiC_2 yield in the SHS product.

TiC is frequently reported as the primary secondary phase in Ti_3SiC_2 synthesis, indicating an insufficient amount of Ti–Si melt available for MAX-phase platelet growth. Therefore, many studies [15–22] use chemical precursors instead of elemental Ti and Si powders. One such precursor is titanium disilicide ($TiSi_2$), which has the lowest crystallization temperature among Ti–Si compounds (1330 °C).

The Ti–Si melt crystallizes within the 1480–1570 °C range, where Ti_3SiC_2 formation becomes significantly slower. Additions of aluminum are known to reduce the crystallization temperature of the Ti–Si melt, thereby increasing the time during which TiC can react with the liquid and form the MAX phase during cooling. For example, the SHS system 3Ti–Si–2C–0.1Al (at. %) synthesized under argon after vacuum drying yielded a product containing 89 wt. %[1] Ti_3SiC_2 [23]. The authors noted that the addition of aluminum to the stoichiometric 3Ti + Si + 2C mixture suppresses the reaction responsible for TiC formation, which in turn increases the Ti_3SiC_2 yield. In the SHS system 3Ti + 1.2Si + 2C + 0.1Al, the Ti_3SiC_2 phase yield reached approximately 83 %, accompanied by 13 % TiC and 4 % Ti_5Si_3 in the product [24]. The beneficial role of a slight silicon excess has also been repeatedly emphasized [25–27], and may likewise be attributed to the crystallization behavior of the Ti–Si melt [28–30].

According to the Ti–Si phase diagram, at 50 at. % Si the crystallization temperature is 1570 °C; a slight Si excess reduces it to about 1480 °C, and at >67 at. % Si it decreases further to approximately 1330 °C.

Copper additions of 5–10 % to Ti and Si also reduce the melting temperatures of the corresponding binary systems [31; 32] and may therefore lower the crystallization temperature of the Ti–Si–Cu melt, potentially promoting an increased Ti_3SiC_2 yield. However, Ti_3SiC_2 is known to decompose in contact with molten Cu via Si deintercalation, forming Cu(Si) and TiC_x [33; 34].

Additions of 10 at. % Cr reduce the melting temperatures of Ti–Cr and Si–Cr alloys from 1670 to 1550 °C and from 1414 to 1305 °C, respectively [35; 36].

No data have been reported on the interaction of molten Cr with Ti_3SiC_2, which is attributed to the high melting temperature of chromium (1856 °C), while Ti_3SiC_2 begins to decompose at about 1450 °C [1].

Controlling the mechanism of Ti_3SiC_2 formation under SHS conditions offers the possibility of developing energy-efficient and technologically simple synthesis routes for MAX phases. Typically, SHS of Ti_3SiC_2 is carried out in sealed reactors under protective atmospheres or in vacuum, which significantly increases production costs and limits scalability. Therefore, the present study aims to identify a simpler and more accessible method for synthesizing Ti_3SiC_2 with minimal secondary phases. This work focuses on evaluating the effects of Si, Al, Cu, Cr, and $TiSi_2$ additions on Ti_3SiC_2 formation during reactor-free SHS in air under a sand bed.

Materials and methods

Powders used as starting reagents for synthesis included porous titanium powder TPP-7 with a coarse particle size ($d \sim 300$ μm, purity 98 %), technical carbon T900 ($d \sim 0.15$ μm, agglomerates up to 10 μm, purity 99.8 %), colloidal graphite C-2 ($d \sim 15$ μm, purity 98.5 %), silicon Kr0 ($d \sim 1$–15 μm, purity 98.8 %), aluminum PA-4 ($d \sim 100$ μm, purity 98 %), copper PMS-1 ($d \sim 100$ μm, purity 99.5 %), chromium Kh99N1 ($d \sim 100$ μm, purity 99.0 %), and titanium disilicide $TiSi_2$ ($d \sim 100$ μm, purity 99.0 %).

The starting powders were weighed on a laboratory balance with an accuracy of 0.01 g and mixed in a ceramic mortar for 5 min to obtain homogeneous mixtures corresponding to the following systems: 3Ti–Si–2C + 0.1Al, 3Ti–Si–2C + 0.1Cu, and 3Ti–Si–2C + 0.1Cr, as well as $TiSi_2$–C, where elemental Si and Ti were replaced by $TiSi_2$ in amounts of 15, 50, and 100 % (complete substitution), calculated for the formation of Ti_3SiC_2 MAX phase.

Cylindrical compacts with a diameter of 23 mm and a mass of 20 g were produced from the prepared powder mixtures by single-action pressing at 22.5 MPa. SHS (combustion) was initiated using an electrically heated Ni–Cr coil. The samples were synthesized by combustion in air under a sand layer, which reduces oxidation of the combustion products [25]. The general scheme of the experiment is shown in Fig. 1. As seen, the pressed powder mixture is completely isolated from the ambient air by the sand bed to limit oxidation of the reaction products. After the SHS reaction, secondary Ti_3SiC_2 formation processes proceed in the cooling sample, also under the sand layer.

Microstructural examination and chemical analysis were performed using a Tescan Vega3 (Czech Republic)

[1] Unless otherwise noted, all compositions are in mass percent (wt. %).

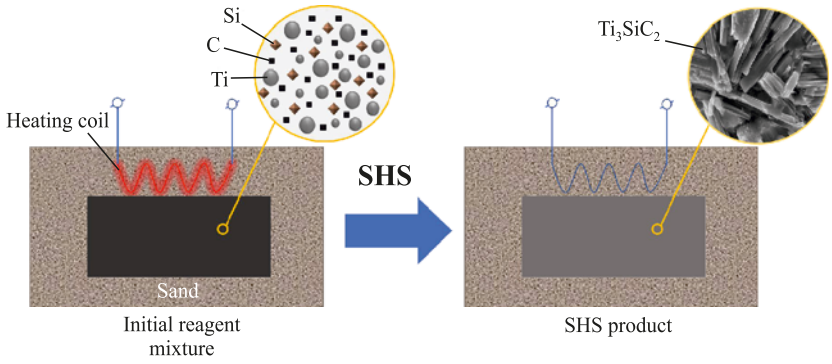

Fig. 1. Scheme for SHS of Ti_3SiC_2 under a sand layer

Рис. 1. Принципиальная схема синтеза Ti_3SiC_2 под слоем песка

scanning electron microscope equipped with an X-act energy-dispersive spectroscopy attachment. The phase composition was determined by *X*-ray diffraction using an ARL X'trA-138 diffractometer (Switzerland) with CuK_α radiation, operated in continuous-scan mode over 2θ = 5–80° at a scan rate of 2°/min. Quantitative phase analysis was carried out using the reference intensity ratio (RIR) method.

Results and discussion

The SHS reaction produces a porous skeleton, which has been repeatedly described in previous studies [9; 12; 25]. After mechanical pulverization, the SHS skeleton is converted into a fine powder, and its particle-size distribution is adjusted using sieves of the required mesh size.

To evaluate the possibility of increasing the Ti_3SiC_2 MAX-phase yield during SHS in air, a series of experiments was performed in which 10 % of Si, Cr, Al, or Cu was added to the 3Ti–1Si–2C charge composition.

In the sample obtained with an excess of silicon (Fig. 2, *a*), the unreacted titanium carbide is non-stoichiometric and corresponds approximately to $TiC_{0.6}$. Elemental analysis of the lighter Ti–Si regions showed an atomic ratio Si:Ti = 60:40, which is consistent with $TiSi_2$. The layered morphology and elemental ratios also confirm the presence of Ti_3SiC_2 regions. A similar microstructural pattern is observed when 10 % Cr is added (Fig. 2, *b*); however, in this case only trace amounts of Ti_3SiC_2 are present, while chromium is concentrated within the $TiSi_2$ phase. In the Cu-containing sample (Fig. 2, *d*), the light-grey regions contain predominantly copper and silicon in a ratio of about 50:15, along with up to 10 at. % carbon. No Ti_3SiC_2 MAX phase is detected, and the non-stoichiometric titanium carbide corresponds to $TiC_{0.5}$. Despite the presence of significant amounts of $TiSi_2$ in direct contact with $TiC_{0.5}$, Ti_3SiC_2 does not form under these conditions. These findings suggest that additions of 10 % Cu or Cr inhibit the formation of Ti_3SiC_2; however, the mechanism governing their influence on MAX-phase formation under SHS conditions requires further study. This may be due to the fact that Cu and Cr cannot occupy the *A*-site in MAX phases, and their presence in the Ti–Si melt hinders Ti_3SiC_2 structural formation.

In the sample containing aluminum (Fig. 2, *c*), thin dark-grey regions surrounding the Ti_3SiC_2 platelets were observed. EDS results indicate that these regions correspond to a mixture of $TiAl_2$ and $TiSi_2$. The crystallization temperature of $TiAl_2$ (1175 °C) is significantly lower than that of the Ti–Si melt (1330–1480 °C, depending on the Ti/Si ratio). Considering that Ti_3SiC_2 forms via the interaction of solid TiC with liquid Ti–Si, it can be inferred that Al reduces the crystallization temperature of the Ti–Si melt, extending the time during which the melt remains liquid under SHS conditions. This prolongs its interaction with TiC and allows Ti_3SiC_2 structure formation to continue for a longer duration, ultimately increasing the MAX-phase content in the SHS product.

These observations are consistent with previous findings reported in [25], where the addition of Al increased the Ti_3SiC_2 yield under reactor-based SHS conditions. The authors showed that a combined excess of 20 % Si and 10 % Al in the Ti:Si:C:Al = 3:1.2:2:0.1 system increases the Ti_3SiC_2 content from 64 to 83 %.

It is reasonable to assume that further optimization of the 3Ti–1*x*Si–2C–*y*Al system, with respect to both the silicon excess (*x*) and the aluminum addition (*y*), may produce even higher Ti_3SiC_2 yields during SHS in air. To verify this, several charge compositions containing different silicon excesses and Al additions were investigated. The results are presented in Table 1. A silicon excess of 15–25 % combined with 10 % Al substantially increases the Ti_3SiC_2 content, reaching a maximum of ~89 vol. % in the 3Ti–1.25Si–2C + 0.1Al system. Varying the Al amount in the absence of excess

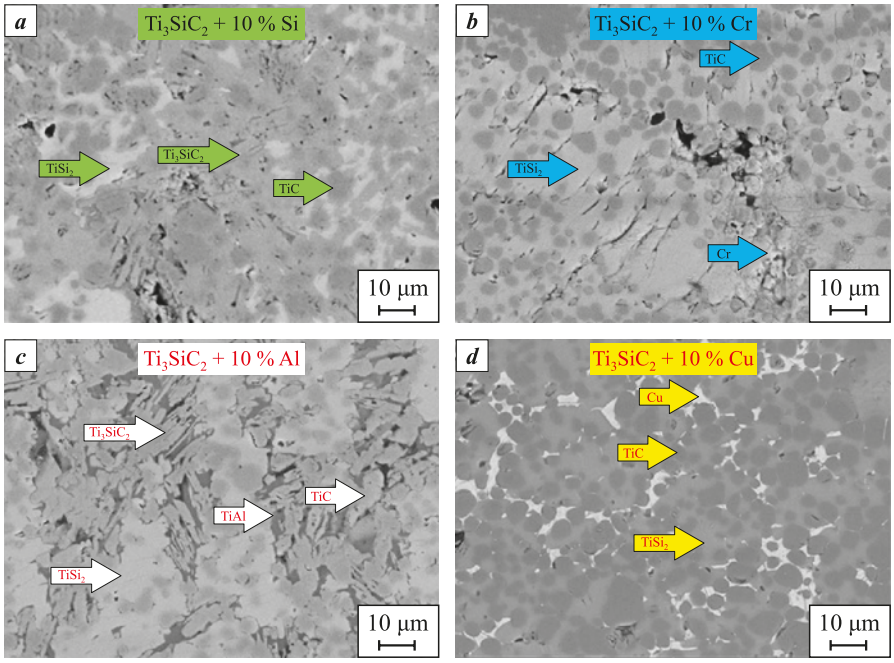

Fig. 2. Microstructures of the samples after introducing 10 % (0.1 mol) of Si (***a***), Cr (***b***), Al (***c***) and Cu (***d***) into the 3Ti–1Si–2C system

Рис. 2. Микроструктуры образцов после введения в систему 3Ti–1Si–2C по 10 % (0,1 моль) Si (***a***), Cr (***b***), Al (***c***) и Cu (***d***)

Si does not significantly affect the Ti_3SiC_2 yield, which remains within 38–47 vol. %. Microstructural images of the sample containing the maximum Ti_3SiC_2 content are shown in Fig. 3. The sample consists predominantly of characteristic, randomly oriented Ti_3SiC_2 platelets, while the pore surfaces are coated with a thin (10–15 μm) layer of densely packed equiaxed TiC particles. The width of most Ti_3SiC_2 platelets ranges from 2 to 5 μm, and their length varies between 10 and 50 μm.

Diffraction patterns of the SHS products with the highest and lowest Ti_3SiC_2 contents are shown in Fig. 4. Based on these data (Fig. 4, *a*), the intensity ratio of the main Ti_3SiC_2 peaks (39.5 and 42.4°) to the TiC peaks (36.0 and 41.8°) corresponds to approximately 80 vol. % Ti_3SiC_2. In Fig. 4, *b*, the TiC peaks are significantly more intense than those of Ti_3SiC_2, which is consistent with ~30 % Ti_3SiC_2 in the product. In addition, distinct graphite peaks (at ~26.5°) are observed in all samples listed in Table 1, as illustrated in Fig. 4, *b*. This indicates that part of the carbon does not completely react during SHS. Notably, the initially amorphous carbon black used as a reagent becomes crystallized into graphite during combustion, as described previously for Ti–C SHS systems [37; 38]. A slight shift of certain Ti_3SiC_2 peaks is also observed, which may indicate partial incorporation of Al into the Ti_3SiC_2 lattice during SHS, a phenomenon previously noted in the literature [23].

Phase composition of SHS products in the 3Ti–*x*Si–2C + *y*Al system

Содержание фаз в СВС-продукте системы 3Ti–*x*Si–2C + *y*Al

Charge composition	Ti_3SiC_2, vol. %	TiC, vol. %
3Ti–1.00Si–2C	36	64
3Ti–1.15Si–2C + 0.1Al	88	12
3Ti–1.20Si–2C + 0.1Al	78	22
3Ti–1.25Si–2C + 0.1Al	89	11
3Ti–1.00Si–2C + 0.05Al	38	62
3Ti–1.00Si–2C + 0.08Al	61	39
3Ti–1.00Si–2C + 0.12Al	47	53

Porous SHS skeletons were also synthesized using $TiSi_2$ as a chemical reagent to replace elemental Ti and Si in quantities of 10, 50, and 100 %. Analysis of the XRD patterns revealed that such substitution results in an increased amount of secondary phases compared to the Ti_3SiC_2 MAX phase (Fig. 5). A new secondary phase, SiC, also appears. The maximum Ti_3SiC_2 content in this series – 56 % – was obtained when silicon was replaced by 10 % $TiSi_2$. However, increasing the $TiSi_2$ fraction to 100 % reduced the Ti_3SiC_2 content to 20 %. For comparison, SHS conducted using elemental Ti, Si, and C powders in the stoichiometric 3Ti–1Si–2C charge composition yields up to 66 % Ti_3SiC_2 [25]. This reduction may be attributed to insufficient temperature in the $TiSi_2$-containing SHS systems, which shortens the lifetime of the Ti–Si melt and prevents the Ti_3SiC_2 structure-formation process from fully completing.

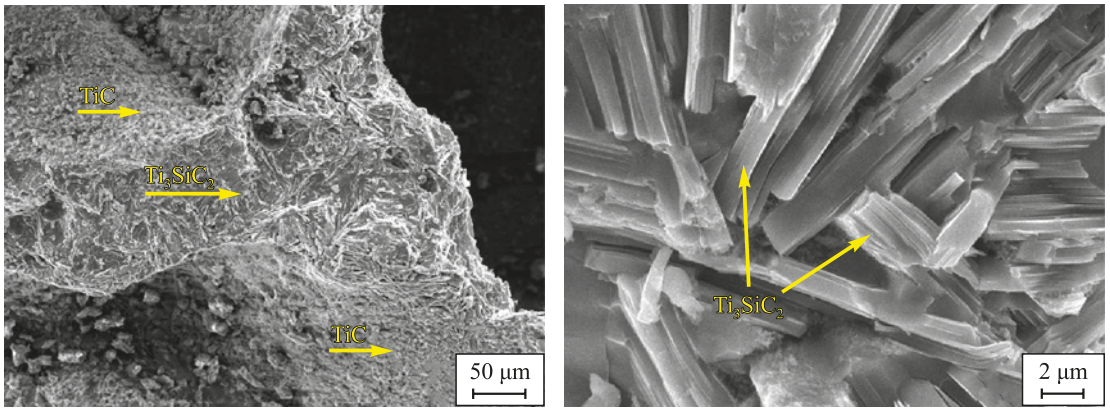

Fig. 3. SEM images of the microstructure of the sample synthesized from the 3Ti–1.25Si–2C + 0.1Al system

Рис. 3. СЭМ-изображения микроструктуры образца, синтезированного из системы 3Ti–1,25Si–2C + 0,1Al

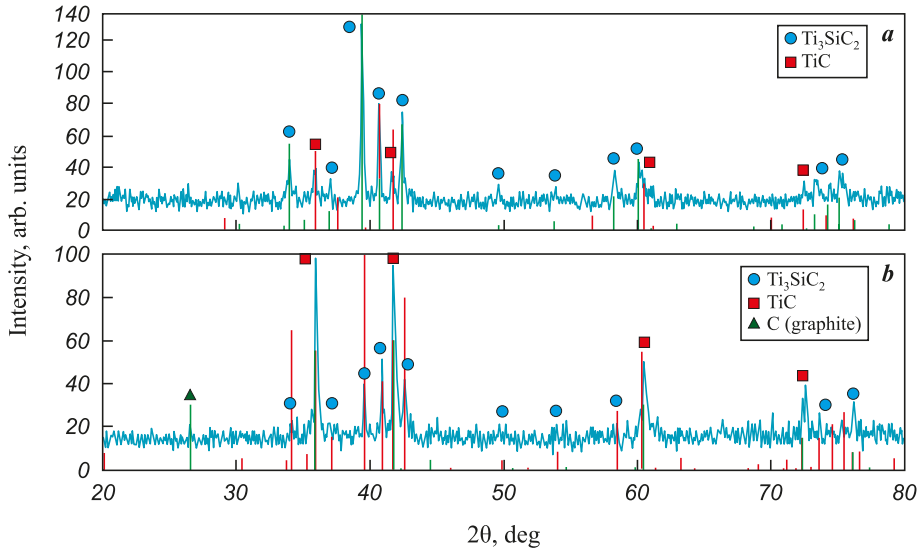

Fig. 4. XRD patterns of the 3Ti–1.25Si–2C + 0.1Al (***a***) and 3Ti–1.00Si–2C + 0.05Al (***b***) systems

Рис. 4. Дифрактограммы систем 3Ti–1,25Si–2C + 0,1Al (***a***) и 3Ti–1,00Si–2C + 0,05Al (***b***)

Conclusions

1. It was established that the combined addition of excess Si and Al in the 3Ti–1.25Si–2C + 0.1Al charge composition substantially increases the Ti_3SiC_2 content, reaching ~89 vol. % under SHS conditions in air using a sand layer without a reactor or protective atmosphere.

2. Additions of Cu and Cr in the 3Ti–1Si–2C + 0.1Cu and 3Ti–1Si–2C + 0.1Cr systems lead to an almost complete suppression of Ti_3SiC_2 formation in the SHS product.

3. Partial (10 and 50 %) and complete (100 %) substitution of the elemental Ti and Si powders with $TiSi_2$ significantly reduces the yield of the Ti_3SiC_2 MAX phase during SHS in air.

4. It is likely that further optimization of the 3Ti–1.25Si–2C + 0.1Al system with respect to the par-

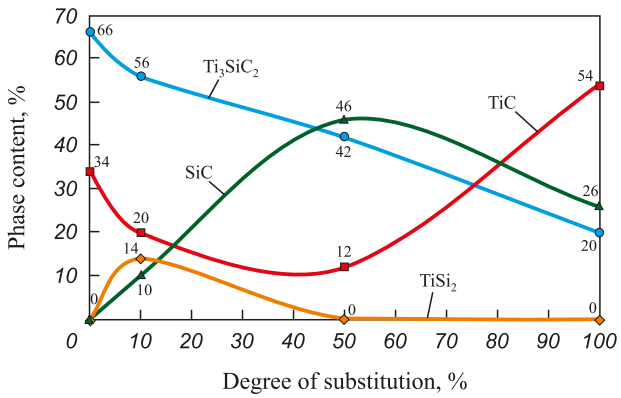

Fig. 5. Dependence of the phase composition of the SHS product on the degree of Si and Ti substitution by $TiSi_2$ in the 3Ti–1Si–2C green mixture

Рис. 5. Зависимость содержания фаз в продукте СВС от степени замещения Si и Ti на $TiSi_2$ в исходной шихтовой смеси 3Ti–1Si–2C

ticle-size distribution of the starting powder reagents, as well as scale-up factors, may allow the Ti_3SiC_2 content to exceed 90 % under reactorless SHS conditions.

References / Список литературы

1. Barsoum M.W. MAX phases: Properties of machinable ternary carbides and nitrides. Weinheim: Wiley-VCH, 2013. P.188–197. https://doi.org/10.1002/9783527654581
2. Gonzalez-Julian J. Processing of MAX phases: From synthesis to applications. *Journal of the American Ceramic Society*. 2020;104:659–690. https://doi.org/10.1111/jace.17544
3. Wu Q., Li C., Tang H. Surface characterization and growth mechanism of laminated Ti_3SiC_2 crystals fabricated by hot isostatic pressing. *Applied Surface Science*. 2010;256(23):6986–6990. https://doi.org/10.1016/j.apsusc.2010.05.012
4. Liu X., Zhang H., Jiang Y., He Y. Characterization and application of porous Ti_3SiC_2 ceramic prepared through reactive synthesis. *Materials and Design*. 2015;79:94–98. https://doi.org/10.1016/j.matdes.2015.03.061
5. El-Raghy T., Wiederhorn S., Luecke W., Radovic M., Barsoum M. Effect of temperature, strain rate and grain size on the mechanical response of Ti_3SiC_2 in tension. *Acta Materialia*. 2002;50(6):1297–1306. https://doi.org/10.1016/S1359-6454(01)00424-4
6. He X., Bai Y., Li Y., Zhu C., Kong X. In situ synthesis and mechanical properties of bulk Ti_3SiC_2/TiC composites by SHS/PHIP. *Materials Science and Engineering A*. 2010;527(18-19):4554–4559. https://doi.org/10.1016/j.msea.2010.04.006
7. Levashov E.A., Mukasyan A.S., Rogachev A.S., Shtansky D.V. Self-propagating high-temperature synthesis of advanced materials and coatings. *International Materials Reviews*. 2016;62(4):1–37. https://doi.org/10.1080/09506608.2016.1243291
8. Amosov A.P., Borovinskaya I.P., Merzhanov A.G. Powder technology of self-propagating high-temperature synthesis of materials: Textbook. Ed. by V.N. Antsiferov. Moscow: Mashinostroenie-1, 2007. 567 p. (In Russ.).

   Амосов А.П., Боровинская И.П., Мержанов А.Г. Порошковая технология самораспространяющегося высокотемпературного синтеза материалов: Учеб. пособие. Под ред. В.Н. Анциферова. М.: Машиностроение-1, 2007. 567 с.
9. Umerov E.R., Latukhin E.I., Amosov A.P., Kichaev P.E. Preparation of Ti_3SiC_2–Sn(Pb) cermet by SHS of Ti_3SiC_2 porous skeleton with subsequent spontaneous infiltration with Sn–Pb melt. *International Journal of Self-Propagating High-Temperature Synthesis*. 2023;32(1):30–35. https://doi.org/10.3103/S1061386223010089
10. Feng A., Orling T., Munir Z.A. Field-activated pressure-assisted combustion synthesis of polycrystalline Ti_3SiC_2. *Journal of Materials Research*. 1999;14(3):925–939. https://doi.org/10.1557/JMR.1999.0124
11. Du Y., Schuster J.C., Seifert H.J., Aldinger F. Experimental investigation and thermodynamic calculation of the titanium–silicon–carbon system. *Journal of the American Ceramic Society*. 2000;83(1):197–203. https://doi.org/10.1111/j.1151-2916.2000.tb01170.x
12. Amosov A.P., Latukhin E.I., Ryabov A.M. SHS process application in Ti_3SiC_2–Ni composite fabrication. *Powder Metallurgy and Functional Coatings*. 2018;(4):48–61. (In Russ.). https://doi.org/10.17073/1997-308X-2018-4-48-61

    Амосов А.П., Латухин Е.И., Рябов А.М. О применении процесса СВС для получения композита Ti_3SiC_2–Ni. *Известия вузов. Порошковая металлургия и функциональные покрытия*. 2018;(4):48–61. https://doi.org/10.17073/1997-308X-2018-4-48-61
13. Konovalikhin S.V., Kovalev D.Yu., Sytschev A.E., Vadchenko S.G., Shchukin A.S. Formation of nanolaminate structures in the Ti–Si–C system: A crystallochemical study. *International Journal of Self-Propagating High-Temperature Synthesis*. 2014;23(4):216–220. https://doi.org/10.3103/S1061386214040049
14. Kachenyuk M.N. Formation of the structure and properties of ceramic materials based on titanium, zirconium, and silicon compounds during consolidation by spark plasma sintering. Diss. of Dr. Sci. (Eng.). Perm; 2022. . 283 p. (In Russ.).

    Каченюк М.Н. Формирование структуры и свойств керамических материалов на основе соединений титана, циркония, кремния при консолидации искровым плазменным спеканием. Дисс. д.т.н. Пермь: 2022. 283 с.
15. Meng F., Liang B., Wang M. Investigation of formation mechanism of Ti_3SiC_2 by self-propagating high-temperature synthesis. *International Journal of Refractory Metals and Hard Materials*. 2013;41:152–161. https://doi.org/10.1016/j.ijrmhm.2013.03.005
16. Hwang S.S., Lee S.C., Han J., Lee D., Park S. Machinability of Ti_3SiC_2 with layered structure synthesized by hot pressing mixture of TiC_x and Si powder. *Journal of the European Ceramic Society*. 2012;32(12):3493–3500. https://doi.org/10.1016/j.jeurceramsoc.2012.04.021
17. Yeh C.-L., Lai K.-L. Effects of TiC, Si, and Al on combustion synthesis of Ti_3SiC_2/TiC/Ti_3Si_2 composites. *Materials*. 2023;16(18):6142. https://doi.org/10.3390/ma16186142
18. Li S.-B., Xie J.-X., Zhang L.-T., Cheng L.-F. In situ synthesis of Ti_3SiC_2/SiC composite by displacement reaction of Si and TiC. *Materials Science and Engineering A*. 2004;381(1-2):51–56. https://doi.org/10.1016/j.msea.2004.03.046
19. Zhang Z.F., Sun Z.M., Hashimoto H., Abe T. A new synthesis reaction of Ti_3SiC_2 through pulse discharge sintering Ti/SiC/TiC powder. *Scripta Materialia*. 2001; 45(12):1461–1467. https://doi.org/10.1016/S1359-6462(01)01184-8
20. Yeh C.L., Shen Y.G. Effects of SiC addition on formation of Ti_3SiC_2 by self-propagating high-temperature synthesis. *Journal of Alloys and Compounds*. 2008;461(1-2): 654–660. https://doi.org/10.1016/j.jallcom.2007.07.088
21. Yeh C.L., Shen Y.G. Effects of TiC addition on formation of Ti_3SiC_2 by self-propagating high-temperature synthesis. *Journal of Alloys and Compounds*. 2008;458(1-2): 286–291. https://doi.org/10.1016/j.jallcom.2007.04.225
22. Sun Z.M., Murugaiahc A., Zhen T., Zhou A., Barsoum M.W. Microstructure and mechanical properties of porous

Ti_3SiC_2. *Acta Materialia*. 2005;53(16):4359–4366. https://doi.org/10.1016/j.actamat.2005.05.034

23. Gubarevich A.V., Tamura R., Maletaskić J., Yoshida K., Yano T. Effect of aluminium addition on yield and microstructure of Ti_3SiC_2 prepared by combustion synthesis method. *Materials Today: Proceedings*. 2019;16:102–108. https://doi.org/10.1016/j.matpr.2019.05.244

24. Yeh C.L., Lai K.L. Effects of excess Si and Al on synthesis of Ti_3SiC_2 by self-sustaining combustion in the Ti–Si–C–Al system. *Journal of the Australian Ceramic Society*. 2024;60(3):959–969. https://doi.org/10.1007/s41779-023-00947-y

25. Davydov D.M., Umerov E.R., Amosov A.P., Latukhin E.I. Influence of starting reagents on the formation of Ti_3SiC_2 porous skeleton by SHS in air. *International Journal of Self-Propagating High-Temperature Synthesis*. 2024;33(1):26–32. https://doi.org/10.3103/S1061386224010023

26. Wakelkamp W.J.J., van Loo F.J.J., Metselaar R. Phase relations in the Ti–Si–C system. *Journal of the European Ceramic Society*. 1991;8(3):135–139. https://doi.org/10.1016/0955-2219(91)90067-A

27. Tabares E., Jiménez-Morales A., Tsipas S.A. Study of the synthesis of MAX phase Ti_3SiC_2 powders by pressureless sintering. *Boletin de la Sociedad Espanola de Ceramica y Vidrio*. 2021;60(1):41–52. https://doi.org/10.1016/j.bsecv.2020.01.004

28. Lepakova O.K., Itin V.I., Astafurova E.G., Erkaev P.A., Kitler V.D., Afanasyev N.I. Synthesis, phase composition, structure and strength properties of porous materials based on Ti_3SiC_2 compound. *Fizicheskaya mezomekhanika*. 2016;19(2):108–113. (In Russ.).

Лепакова О.К., Итин В.И., Астафурова Е.Г., Еркаев П.А., Китлер В.Д., Афанасьев Н.И. Синтез, фазовый состав, структура и прочностные свойства пористых материалов на основе соединения Ti_3SiC_2. *Физическая мезомеханика*. 2016;19(2):108–113.

29. Zhou C.L., Ngai T.W.L., Lu L., Li Y.Y. Fabrication and characterization of pure porous Ti_3SiC_2 with controlled porosity and pore features. *Materials Letters*. 2014;131:280–283. https://doi.org/10.1016/j.matlet.2014.05.198

30. El Saeed M.A., Deorsola F.A., Rashad R.M. Optimization of the Ti_3SiC_2 MAX phase synthesis. *International Journal of Refractory Metals and Hard Materials*. 2012;35:127–131. https://doi.org/10.1016/j.ijrmhm.2012.05.001

31. Eremenko V.N., Buyanov Y.I., Prima S.B. Phase diagram of the system titanium–copper. *Powder Metallurgy and Metal Ceramics*. 1966;5(6):494–502. https://doi.org/10.1007/BF00775543

32. Olesinski R.W., Abbaschian G.J. The Cu–Si (copper–silicon) system. *Bulletin of Alloy Phase Diagrams*. 1986;7(2):170–178. https://doi.org/10.1007/BF02881559

33. Zhou Y., Gu W. Chemical reaction and stability of Ti_3SiC_2 in Cu during high-temperature processing of Cu/Ti_3SiC_2 composites. *International Journal of Materials Research*. 2004;95(1):50–56. https://doi.org/10.3139/146.017911

34. Amosov A.P., Latukhin E.I., Ryabov A.M., Umerov E.R., Novikov V.A. Application of SHS process for fabrication of copper–titanium silicon carbide composite (Cu–Ti_3SiC_2). *Journal of Physics: Conference Series*. 2018;1115(4):042003. https://doi.org/10.1088/1742-6596/1115/4/042003

35. Murray J.L. The Cr–Ti (chromium–titanium) system. *Bulletin of Alloy Phase Diagrams*. 1981;2(2):174–181. https://doi.org/10.1007/BF02881474

36. Gokhale A.B., Abbaschian G.J. The Cr–Si (chromium–silicon) system. *Journal of Phase Equilibria and Diffusion*. 1987;8(5):474–484. https://doi.org/10.1007/BF02893156

37. Shcherbakov V.A., Gryadunov A.N., Karpov A.V., Sachkova N.V., Sychev A.E. Self-propagating high-temperature synthesis of TiC + *x*C composites. *Inorganic Materials*. 2020;56(6):567–571. https://doi.org/10.1134/S0020168520060102

Щербаков В.А., Грядунов А.Н., Карпов А.В., Сачкова Н.В., Сычев А.Е. Самораспространяющийся высокотемпературный синтез композитов TiC + *x*C. *Неорганические материалы*. 2020;56(6):598–602. https://doi.org/10.31857/s0002337x20060111

38. Umerov E.R., Amosov A.P., Latukhin E.I., Novikov V.A. SHS of TiC–graphite porous composites and carbon graphitization. *International Journal of Self-Propagating High-Temperature Synthesis*. 2025;34(1):42–49. https://doi.org/10.3103/S1061386224700407

Information about the Authors

Emil R. Umerov – Cand. Sci. (Eng.), Leading Researcher of the Department of metal science, powder metallurgy, nanomaterials (MPMN), Samara State Technical University (SamSTU)
ORCID: 0000-0002-2050-6899
E-mail: umeroff2017@yandex.ru

Shamil A. Kadyamov – Postgraduate Student of the Department of MPMN, SamSTU
ORCID: 0009-0005-6578-367X
E-mail: leader2310@mail.ru

Denis M. Davydov – Cand. Sci. (Eng.), Junior Researcher of the Department of MPMN, SamSTU
ORCID: 0000-0001-5469-8588
E-mail: davidov@npcsamara.ru

Сведения об авторах

Эмиль Ринатович Умеров – к.т.н., вед. науч. сотрудник кафедры «Металловедение, порошковая металлургия, наноматериалы» (МПМН), Самарский государственный технический университет (СамГТУ)
ORCID: 0000-0002-2050-6899
E-mail: umeroff2017@yandex.ru

Шамиль Акдасович Кадямов – аспирант кафедры МПМН, СамГТУ
ORCID: 0009-0005-6578-367X
E-mail: leader2310@mail.ru

Денис Михайлович Давыдов – к.т.н., мл. науч. сотрудник кафедры МПМН, СамГТУ
ORCID: 0000-0001-5469-8588
E-mail: davidov@npcsamara.ru

Evgeny I. Latukhin – Cand. Sci. (Eng.), Associate Professor of the Department of MPMN, SamSTU
ORCID: 0000-0002-2071-3521
E-mail: evgelat@yandex.ru

Aleksandr P. Amosov – Dr. Sci. (Phys.-Math.), Prof., Head of the Department of MPMN, SamSTU
ORCID: 0000-0003-1994-5672
E-mail: egundor@yandex.ru

Евгений Иванович Латухин – к.т.н., доцент кафедры МПМН, СамГТУ
ORCID: 0000-0002-2071-3521
E-mail: evgelat@yandex.ru

Александр Петрович Амосов – д.ф.-м.н.., проф., зав. кафедрой МПМН, СамГТУ
ORCID: 0000-0003-1994-5672
E-mail: egundor@yandex.ru

Contribution of the Authors

E. R. Umerov – formulation of the research problem, conducting experiments, writing the manuscript.
Sh. A. Kadyamov – preparation of charge mixtures and synthesis of samples, participation in the discussion of the results.
D. M. Davydov – microstructural examination and phase analysis of the samples, participation in the discussion of the results.
E. I. Latukhin – participation in the experiments and discussion of the results, writing the manuscript.
A. P. Amosov – definition of the aim of the study, participation in the discussion of the results, manuscript editing.

Вклад авторов

Э. Р. Умеров – определение задачи работы, проведение экспериментов, написание статьи.
Ш. А. Кадямов – подготовка шихтовых смесей и синтез образцов, участие в обсуждении результатов.
Д. М. Давыдов – исследование микроструктуры, фазовый анализ образцов, участие в обсуждении результатов.
Е. И. Латухин – участие в проведении экспериментов и обсуждении результатов, написание статьи.
А. П. Амосов – определение цели работы, участие в обсуждении результатов, редактирование статьи.

Received 21.04.2025
Revised 12.05.2025
Accepted 15.05.2025

Статья поступила 21.04.2025 г.
Доработана 12.05.2025 г.
Принята к публикации 15.05.2025 г.

Refractory, Ceramic, and Composite Materials
Тугоплавкие, керамические и композиционные материалы

UDC 666.3

https://doi.org/10.17073/1997-308X-2025-6-36-43

Research article
Научная статья

Synthesis of optically transparent YAG:Ru ceramics

V. E. Suprunchuk, A. A. Kravtsov, V. A. Lapin, F. F. Malyavin, D. P. Bedrakov

North-Caucasus Federal University
1a Pushkin Str., Stavropol 355000, Russia

vikasuprunchuk@gmail.com

Abstract. Yttrium–aluminum garnet (YAG) ceramics doped with ruthenium atoms were synthesized in this study. The precursor powder was obtained by the coprecipitation method. The dopant, in the form of ruthenium (III) chloride, was introduced at different technological stages: during precursor powder synthesis and during deagglomeration of the ceramic powder, resulting in two series of samples. The phase composition of the sintered ceramics was examined by *X*-ray diffraction (XRD). According to the obtained data, no secondary or impurity phases were detected. Differential thermal analysis (DTA) revealed a decrease in the cationic homogeneity of the precursor powder. Incorporation of ruthenium into the YAG structure led to a shift of the exothermic crystallization peak toward higher temperatures. The ceramic samples were sintered at 1815 °C for 20 h, followed by annealing in air at 1500 °C for 2 h. Optical characterization of the ceramics showed that the method of dopant introduction affected both the optical transmittance and the band gap energy. The transmittance at 1100 nm for undoped YAG ceramics was 77.04 %, while for the ruthenium-containing samples it decreased to 65.1 and 74.5 %, depending on the dopant incorporation route. The band gap energy was determined from differential absorption spectra: for pure YAG it was 4.92 eV, and for the Ru-doped ceramics it decreased to a minimum of 4.4 eV.

Keywords: YAG:Ru, ceramics, optical properties, band gap energy, coprecipitation method, ceramic powder

Acknowledgements: This study was supported by the Russian Science Foundation, Project No. 24-73-00023 (https://rscf.ru/project/24-73-00023).

For citation: Suprunchuk V.E., Kravtsov A.A., Lapin V.A., Malyavin F.F., Bedrakov D.P. Synthesis of optically transparent YAG:Ru ceramics. *Powder Metallurgy and Functional Coatings*. 2025;19(6):36–43. https://doi.org/10.17073/1997-308X-2025-6-36-43

Получение оптически прозрачного граната YAG:Ru

В. Е. Супрунчук, А. А. Кравцов, В. А. Лапин, Ф. Ф. Малявин, Д. П. Бедраков

Северо-Кавказский федеральный университет
Россия, 355000, г. Ставрополь, ул. Пушкина, 1а

vikasuprunchuk@gmail.com

Аннотация. В ходе работы осуществлен синтез керамики на основе иттрий-алюминиевого граната (YAG), легированного атомами рутения. Порошок-прекурсор получен методом соосаждения. Легирующий агент в виде хлорида рутения (III) вводили на разных технологических стадиях: в ходе синтеза порошков-прекурсоров и на этапе деагломерации керамического порошка, с формированием двух серий образцов. Методом рентгенофазного анализа изучали фазовый состав готовой керамики. Согласно полученным данным присутствие вторичных и примесных фаз не выявлено. С помощью дифференциально-термического анализа установлено снижение катионной однородности порошка-прекурсора. При введении рутения в структуру граната наблюдалось смещение экзотермического пика его кристаллизации в сторону больших температур. Спекание образцов керамик осуществляли при температуре 1815 °C в течение 20 ч с последующим отжигом на воздухе

при $t = 1500$ °C, $\tau = 2$ ч. При определении оптических характеристик керамических материалов было установлено, что способ введения лигатуры приводит к изменению показателя светопропускания, а также снижению энергии запрещенной зоны. Показатель светопропускания керамики на длине волны 1100 нм для нелегированного иттрий-алюминиевого граната составил 77,04 %, а для керамических образцов, содержащих рутений, этот показатель снизился до 65,1 и 74,5 % в зависимости от способа введения примесных ионов. Энергию запрещенной зоны образцов рассчитывали из дифференциальных спектров поглощения: ширина запрещенной зоны для чистого граната составила 4,92 эВ, а для легированного – она снизилась до минимального значения 4,4 эВ.

Ключевые слова: YAG:Ru, керамика, оптические свойства, энергия запрещенной зоны, метод соосаждения, керамический порошок

Благодарности: Исследование выполнено за счет средств гранта Российского научного фонда, проект № 24-73-00023 (https://rscf.ru/project/24-73-00023).

Для цитирования: Супрунчук В.Е., Кравцов А.А., Лапин В.А., Малявин Ф.Ф., Бедраков Д.П. Получение оптически прозрачного граната YAG:Ru. *Известия вузов. Порошковая металлургия и функциональные покрытия*. 2025;19(6):36–43. https://doi.org/10.17073/1997-308X-2025-6-36-43

Introduction

Yttrium–aluminum garnet (YAG) is a crystalline material with a cubic structure characterized by high thermal conductivity, chemical stability, and excellent physical and optical properties. These features make it suitable for a wide range of industrial applications. YAG is widely used in most laser systems [1], light-emitting diodes (LEDs), and various optical and electronic devices. It can be produced in both single-crystal and polycrystalline forms. Recently, polycrystalline materials doped with rare-earth elements have gained attention as alternatives to single crystals [2], the fabrication of which often poses challenges in achieving uniform dopant distribution [3].

In contrast to single crystals, ceramic processing allows not only for homogeneous atomic-level dopant distribution but also for the fabrication of components with controlled geometry and dimensions. Particular attention has been given to doping YAG with trivalent rare-earth ions [4]. The incorporation of impurity ions follows the general principles of ionic size and charge compatibility with the substituted garnet-forming ions [5]. It is well established that doping and variation of dopant concentration can alter the optical [6], mechanical, and thermal properties of the material [4; 7].

Ruthenium, a 4*d*-transition metal cation, is an attractive dopant owing to the diversity of its electronic states, which impart unique electronic, magnetic [8], photorefractive, and photochromic properties to the host matrix [9; 10]. Most studies on Ru applications focus on catalyst development [11; 12], conductive metallic coatings for electrochemical gas sensors [13], and chromatographic detectors [14]. In ceramic systems, ruthenium has been introduced into oxide matrices to enhance electronic conductivity [15; 16], dielectric permittivity [17], and electrical resistivity control [18], and to develop intermediate-temperature ion-transport ceramic membranes [19].

The behavior of Ru has been extensively studied in certain oxide systems, such as perovskite-type structures $AA'_3B_4O_{12}$ [12; 16; 20]. However, no literature reports were found on the fabrication of optically transparent YAG:Ru ceramics. It can be assumed that the introduction of Ru into the YAG structure may enable targeted modification of its optical characteristics.

The present work aimed to obtain optically transparent YAG:Ru ceramics and to determine the optimal synthesis route. Our previous results demonstrated the feasibility of incorporating Ru into the garnet structure during ceramic powder synthesis [21]. Further study of YAG:Ru materials may reveal their potential for applications in the production of polycrystalline optical isolators, absorbers, and LEDs. Therefore, in this work, YAG:Ru compositions were synthesized using different methods of Ru incorporation into the YAG lattice, and the effects of Ru addition on the microstructural features, phase transformations of powders, phase composition, and optical properties of the final ceramics were investigated.

Materials and methods

The ceramic materials were synthesized using the following reagents:

– ammonia (25 %, pure grade, SigmaTek, Russia);

– aluminum chloride hexahydrate (99 %, Nevatorg, Russia);

– ruthenium (III) chloride (99 %, Anhui Herrman Impex Co. Ltd., China);

– yttrium chloride hexahydrate (99.9 %, Nevatorg, Russia);

– ammonium sulfate (99 %, Stavreakhim, Russia);

– isopropyl alcohol (99.7 %, Khimprom LLC, Russia);

– calcium chloride (99 %, Vekton, Russia);

– magnesium chloride (99.9 %, Interkhim, Russia).

Deionized water was used to prepare all solutions.

To determine the optimal stage for introducing the dopant, three types of samples were prepared: S_0 – pure YAG; S_Ru – YAG:Ru, where the dopant was added during precursor synthesis; S_0_Ru – YAG:Ru, where Ru was introduced during the deagglomeration of the ceramic powder in a ball mill.

The precursor powders S_0 and S_Ru were synthesized by the coprecipitation method. For this purpose, solutions of yttrium and aluminum salts (and additionally ruthenium salts for S_Ru) were added dropwise into a 2.7 % ammonia precipitant solution using a peristaltic pump. The salt solution also contained $NH_4(SO_4)_2$ at a concentration of 0.08 M. The resulting precipitate was washed with 0.045 M ammonium sulfate solution, followed by isopropyl alcohol, and dried at 60 °C for 15 h. The dried precipitate was sieved through a 200-mesh screen, ground, and mixed with sintering additives. Grinding was carried out in a planetary ball mill (Pulverisette 5, Fritsch, Germany) using alumina balls (2 mm) for 30 min at 150 rpm in 0.2 M ammonium sulfate solution. The mass ratio of milling medium:grinding media:powder was 4.5:4.5:1.0. Magnesium oxide (MgO) and calcium oxide (CaO) were added as sintering aids at 0.1 at. % each. The powders were calcined in air at 1150 °C for 2 h in a high-temperature furnace (Nabertherm 40/17, Germany).

The S_0 powder was divided into two portions, and ruthenium (III) chloride was introduced into one of them. All powder samples were then ground in a planetary ball mill with alumina balls (1 mm) at a medium-to-ball-to-powder ratio of 3.5:5.5:1.0 for 20 min at 150 rpm. The resulting suspensions were dried and sieved through a 200-mesh screen. The powders were uniaxially pressed at 50 MPa and sintered under vacuum at 1815 °C for 20 h. The sintered samples were ground to a thickness of 2 ± 0.1 mm, polished using a QPol-250 setup, and annealed in air at 1500 °C for 2 h (Nabertherm 40/17).

The particle-size distribution was analyzed by laser diffraction (LDA) using a SALD-7500 nano analyzer (Shimadzu, Japan). The morphology of the powders and ceramics was studied by scanning electron microscopy (SEM) using a MIRA3-LMH microscope (Tescan, Czech Republic) equipped with an AZtecEnergy Standard/X-max 20 EDS system. The specific surface area was determined by the Brunauer–Emmett–Teller (BET) method on a 3Flex analyzer (Micromeritics, USA) by nitrogen adsorption at T = 77 K.

Thermal behavior of the precursor powders was studied by differential thermal analysis (DTA) and thermogravimetry (TG) using an STA 449 F5 Jupiter analyzer (NETZSCH-Gerätebau GmbH, Germany) in the temperature range 20–1300 °C under air flow (25 °C/min). Phase composition of the ceramics was examined by X-ray diffraction (XRD) on a TD-3700 diffractometer (Tongda, China) equipped with a CuK_α radiation source (λ = 1.5406 Å).

Optical transmittance in the wavelength range λ = 200–1100 nm was measured using an SF-56 spectrophotometer (OKB-Spektr, Russia).

Results and discussion

At the first stage, YAG and YAG:Ru precursor powders were synthesized and characterized in terms of particle-size distribution. Fig. 1 shows the cumulative particle-size curves of both powders. In both cases, a monomodal distribution with similar values was observed. The median particle diameters (d_{50}) for S_0 and S_Ru were 2.3 and 2.6 μm, respectively, indicating a negligible effect of cationic composition on powder dispersion.

The morphology of YAG and YAG:Ru powders was examined by SEM. As shown in Fig. 2, the particles form loose, coarse agglomerates. They have an elongated shape and may consist of several crystallites connected by necks. No morphological differences were observed between S_0 and S_Ru powders.

The specific surface areas were also comparable – 11.06 m^2/g for YAG and 10.28 m^2/g for YAG:Ru – indicating a branched surface structure. Thus, the introduction of Ru did not significantly affect the morphology of the ceramic powders.

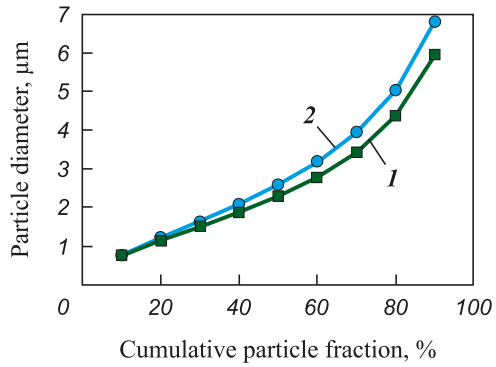

Fig. 1. Cumulative particle-size distribution curves of precursor powders S_0 (***1***) and S_Ru (***2***)

Рис. 1. Кумулятивные кривые распределения частиц порошков-прекурсоров образцов S_0 (***1***) и S_Ru (***2***)

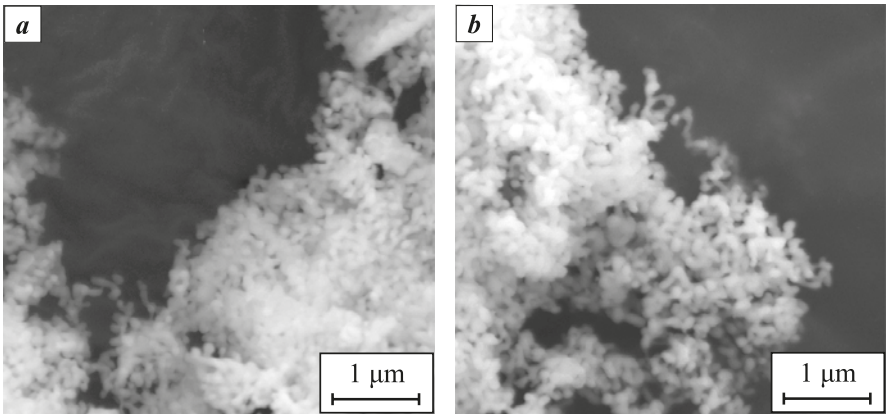

Fig. 2. SEM images of ceramic powders S_0 (***a***) and S_Ru (***b***)

Рис. 2. СЭМ-изображения керамических порошков S_0 (***a***) и S_Ru (***b***)

Thermal analysis curves of precursor powders S_0 and S_Ru are shown in Fig. 3. Both samples exhibited pronounced weight loss. The first critical weight-loss region (≈30 %) occurred between 100 and 450 °C and was attributed to the removal of adsorbed and chemically bound water, ammonia, and nitro groups [22; 23], as indicated by the endothermic peak at 200 °C. The second weight-loss region (900–1100 °C) included two endothermic and one exothermic peak. The endothermic peaks correspond to the decomposition of sulfates and oxysulfates and desorption of sulfate groups [24], while the exothermic peak near 940 °C is associated with YAG crystallization [25]. In the Ru-doped sample, this crystallization peak shifted toward higher temperatures, likely due to reduced cationic homogeneity of the precursor powder. Broadening of this peak suggests the formation of intermediate phases prior to YAG crystallization.

The phase composition of the ceramics after vacuum sintering at 1815 °C for 20 h was determined for S_0, S_Ru, and S_0 _Ru samples. XRD patterns (Fig. 4) confirmed that all samples were single-phase solid solutions with a garnet structure and contained no secondary or Ru-bearing impurity phases such as RuO_2. This indicates structural uniformity of the synthesized YAG ceramics regardless of the Ru introduction method.

Optical characterization of the ceramics was then carried out. Prior to measurement, all samples were

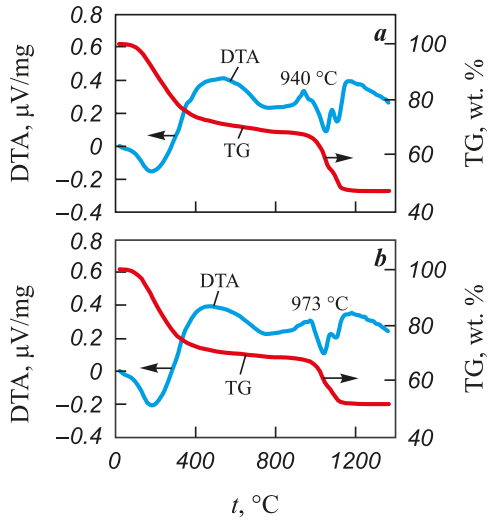

Fig. 3. Thermogravimetric (TGA) and differential thermal analysis (DTA) curves of precursor powders S_0 and S_Ru

Рис. 3. Кривые термогравиметрического (ТГА) и дифференциального термического (ДТА) анализов порошков-прекурсоров S_0 и S_Ru

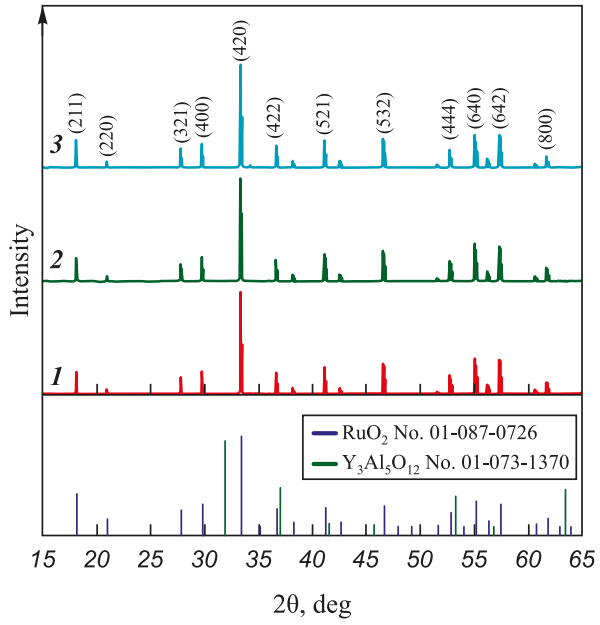

Fig. 4. XRD patterns of YAG ceramics S_0 (***1***), S_Ru (***2***), and S_0 _Ru (***3***)

Рис. 4. Рентгеновские дифрактограммы керамики S_0 (***1***), S_Ru (***2***) и S_0 _Ru (***3***)

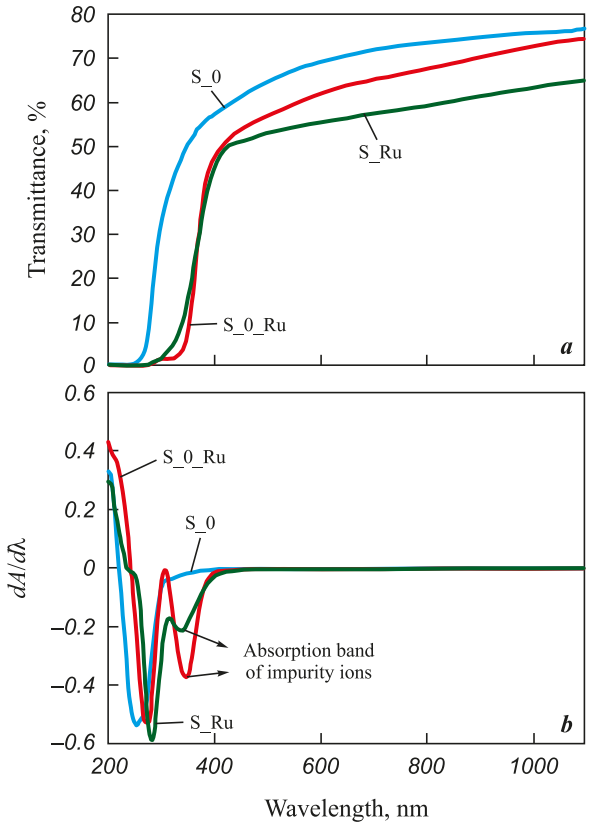

Fig. 5. Optical transmittance spectra (***a***) and differential absorption spectrum (***b***) of YAG ceramics

Рис. 5. Спектры светопропускания (***a***) и дифференциальный спектр поглощения (***b***)

annealed in air at 1500 °C for 2 h. The transmittance spectra (Fig. 5, *a*) revealed that the linear optical transmittance at 1100 nm was 77.04 % for YAG, 65.1 % for S_Ru, and 74.5 % for S_0_Ru. These results indicate that Ru doping decreases the optical transparency of YAG, particularly when Ru is introduced during hydroxide precipitation.

Reduced transmittance was observed across the entire wavelength range (200–1100 nm), which may be attributed to color changes induced by Ru incorporation into the garnet lattice (Fig. 6). The gray coloration likely results from the formation of oxygen vacancies that act as color centers due to electron association and remain partially stable after air annealing [26]. Therefore, the observed coloration is directly related to the dopant ions introduced.

Fig. 6. Photographs of ceramic samples S_0, S_Ru, and S_0_Ru Captured with Pixel 8 Pro, ISO 41, f/1.95, exposure 1/336 s, D65 daylight; reference sample: S_0

Рис. 6. Фотографии образцов керамики S_0, S_Ru и S_0_Ru Режим съемки: камера Pixel 8 Pro ISO 41, f/1.95; выдержка 1/336 с; дневное освещение (D65); контроль: образец S_0

Additionally, a shift in the absorption edge was observed, which can be associated with lattice disorder caused by Ru doping and a decrease in the band gap energy. The latter was calculated from the absorption spectra derived from transmittance data [27] and differentiated (Fig. 5, *b*). The differential absorption spectrum (rate of absorbance change $d_A/d\lambda$) of pure YAG exhibits a single absorption edge corresponding to a band gap of 4.92 eV. For the S_Ru and S_0_Ru samples, two absorption edges were observed, likely due to intrinsic absorption of ruthenium ions through $Ru^{3+} \rightarrow Ru^{4+}$ transitions. The calculated band gap energies for S_Ru and S_0_Ru were 4.4 and 4.54 eV, respectively.

Thus, the sample doped during the deagglomeration stage exhibited higher optical transmittance and a smaller absorption-edge shift, indicating that this method provides the most favorable route for obtaining optically transparent YAG:Ru ceramics.

Conclusions

YAG:Ru ceramic powders were synthesized by the coprecipitation method, and the optimal stage for introducing ruthenium (III) chloride into the system was identified. According to DTA, incorporation of Ru into the garnet lattice shifts the exothermic YAG formation peak to higher temperatures, which is consistent with reduced cation homogeneity in the YAG precursor. Ru in the garnet structure also decreases optical transmittance across the entire measured wavelength range (200–1100 nm): from 77.04 % for undoped YAG to a minimum of 65.1 % for YAG:Ru.

Ceramics obtained when the dopant was introduced during deagglomeration of the ceramic powder exhibited a higher linear transmittance (74.5 %) and a smaller absorption-edge shift – with the band gap decreasing from 4.92 eV (pure YAG) to 4.54 eV (YAG:Ru) – which makes this route the preferred method for producing optically transparent YAG:Ru ceramics.

Although Ru doping lowers transmittance, it modulates the optical response relative to pure YAG. The combined effects – band-gap narrowing and enhanced absorption – are promising for the development of broadband absorbers, neutral-density optical filters, and passive optical limiting devices.

References / Список литературы

1. Ikesue A., Aung Y.L., Taira T., Kamimura T., Yoshida K., Messing G.L., Progress in ceramic lasers. *Annual Review of Materials Research*. 2006;36:397–429. https://doi.org/10.1146/annurev.matsci.36.011205.152926
2. Ali H., Masschelein P., Bruyere S., Pigeat P., Dauscher A., Rinnert H., Horwat D., Khedr M.A., Giba A.E. White light emission from Sm-doped YAG ceramic controlled by the excitation wavelengths. *Optics & Laser Technology*. 2021;142:107223. https://doi.org/10.1016/j.optlastec.2021.107223
3. Lu J., Prabhu M., Song J., Li C., Xu J., Ueda K., Kaminskii A.A., Yagi H., Yanagitani T. Optical properties and highly efficient laser oscillation of Nd:YAG ceramics. *Applied Physics B: Lasers and Optics*. 2000;71(4):469–473. https://doi.org/10.1007/s003400000394
4. Timoshenko A.D., Matvienko O.O., Doroshenko A.G., Parkhomenko S.V., Vorona I.O., Kryzhanovska O.S., Safronova N.A., Vovk O.O., Tolmachev A.V., Baumer V.N., Matolínová I., Hau S., Gheorghe C., Yavetskiy R.P. Highly-doped YAG:Sm3+ transparent ceramics: Effect of Sm^{3+} ions concentration. *Ceramics International*. 2023;49(5):7524–7533. https://doi.org/10.1016/j.ceramint.2022.10.257
5. Boulesteix R., Maître A., Baumard J.-F., Sallé C., Rabinovitch Y. Mechanism of the liquid-phase sintering for Nd:YAG ceramics. *Optical Materials*. 2009;31(5): 711–715. https://doi.org/10.1016/j.optmat.2008.04.005
6. Wu X., Wang S., Wong-Ng W., Gu Q., Jiang Y., Wang C., Ma S., Liu W. Novel optical properties and induced magnetic moments in Ru-doped hybrid improper ferroelectric $Ca_3Ti_2O_7$. *Journal of Advanced Ceramics*. 2021;28;10(1):120–128. https://doi.org/10.1007/s40145-020-0425-2
7. Yagi H., Yanagitani T., Numazawa T., Ueda K. The physical properties of transparent $Y_3Al_5O_{12}$. *Ceramics International*. 2007;33(5):711–714. https://doi.org/10.1016/j.ceramint.2005.12.007
8. Banerjee A. Fluoride electrolyte based galvanic cell: Stability of the hollandite $BaRu_6O_{12}$(s). *Journal of Fluorine Chemistry*. 2021;245:109779. https://doi.org/10.1016/j.jfluchem.2021.109779
9. Wu S.-Y., Fu Q., Lin J.-Z., Zhang H.-M. Theoretical studies of the local structures and the EPR parameters for Ru^{3+} in the garnets. *Optical Materials*. 2007;29(8): 1014–1018. https://doi.org/10.1016/j.optmat.2006.03.036
10. Chiang C.H., Chen J., Hu C. Photorefractive and photochromic properties of Ru-doped lithium niobate crystal. In: *Proc. of Conference on Lasers and Electro-Optics Europe-Technical Digest*. Munich, Germany, 2007. CC_15. https://doi.org/10.1109/CLEOE-IQEC.2007.4386031
11. Masuda Y., Hosokawa S., Inoue M. Combustion activities of the Ru catalysts supported on hexagonal $YbFeO_3$. *Journal of the Ceramic Society of Japan*. 2011; 119(1395):850–854. https://doi.org/10.2109/jcersj2.119.850
12. Sun N., Li W., Qin Y., Zheng Z., Zhang B., Dong X., Wei P., Zhang Y., He X., Xie X., Huang K., Wu L., Lei M., Gou H., Yu R. Screening A-site ordered quadruple perovskites for alkaline hydrogen evolution reaction via unifying electronic configuration descriptor. *Chinese Physics B*. 2024;33(12):128101. https://doi.org/10.1088/1674-1056/ad8074
13. Fesik E.V., Grebnev V.V., Zarazhevskii V.I., Mal'chikov G.D. Ruthenium coatings on zirconium dioxide ceramic: Physicochemical and functional properties. *Russian Journal of Applied Chemistry*. 2014;87(5):591–595. https://doi.org/10.1134/S1070427214050097

    Фесик Е.В., Гребнев В.В., Заражевский В.И., Мальчиков Г.Д. Рутениевые покрытия на керамике из диоксида циркония: физико-химические и функциональные свойства. *Журнал прикладной химии*. 2014;87(5):601–606.
14. Salimi A., Pourbeyram S., Amini M.K. Renewable-surface sol–gel derived carbon ceramic electrode fabricated by [Ru(bpy)(tpy)Cl]PF 6 and its application as an amperometric sensor for sulfide and sulfur oxoanions. *The Analyst*. 2002;127(12):1649–1656. https://doi.org/10.1039/B209194A
15. Hu D., Wang R., Du P., Li G., Wang Y., Fan D., Pan X. Electrospinning Ru doped Co_3O_4 porous nanofibers as promising bifunctional catalysts for oxygen evolution and oxygen reduction reactions. *Ceramics International*. 2022;48(5):6549–6555. https://doi.org/10.1016/j.ceramint.2021.11.202
16. Veselinović L., Mitrić M., Mančić L., Jardim P.M., Škapin S.D., Cvjetićanin N., Milović M.D., Marković S. Crystal Structure and Electrical Properties of Ruthenium-Substituted Calcium Copper Titanate. *Materials*. 2022;29;15(23):8500. https://doi.org/10.3390/ma15238500
17. Li W., Zhang T., Liu S., Lu Z., Xiong R. Decrease in the dielectric loss of $CaCu_3Ti_4O_{12}$ at high frequency by Ru doping. *Ceramics International*. 2017;43(5):4366–4371. https://doi.org/10.1016/j.ceramint.2016.12.082
18. Annamalai S., Vidensky I., Pegg I.L., Dutta B. Effect of cation stoichiometry on the transport properties of calcium ruthenium oxide ceramics. *Journal of Materials Science*. 2008;43(14):4996–5004. https://doi.org/10.1007/s10853-008-2739-2
19. Dergacheva P.E., Kulbakin I.V., Fedorov S.V., Lysenkov A.S., Artemov V.V. Ceramic composite membranes based on $Bi_3Ru_3O_{11}$–$Bi_{1.6}Er_{0.4}O_3$ for obtaining of oxygen. *Inorganic Materials: Applied Research*. 2021;12(5):1326–1331. https://doi.org/10.1134/S2075113321050087
20. Mizumaki M., Mizokawa T., Agui A., Tanaka S., Takatsu H., Yonezawa S., Maeno Y. Oxygen hole state in A-site ordered perovskite $ACu_3Ru_4O_{12}$ (A = Na, Ca, and La) probed by resonant *X*-ray emission spectroscopy. *Journal of the Physical Society of Japan*. 2013;82(2):024709. https://doi.org/10.7566/JPSJ.82.024709
21. Suprunchuk V.E., Kravtsov A.A., Tarala L.V., Medyanik E.V., Malyavin F.F., Lapin V.A., Bedrakov D.P. Synthesis of yttrium aluminum garnet ceramic powder doped with ruthenium. *Fiziko-khimicheskie aspekty izucheniya klasterov, nanostruktur i nanomaterialov*.

2024;(16):1016–1024. (In Russ.).
https://doi.org/10.26456/pcascnn/2024.16.1016

Супрунчук В.Е., Кравцов А.А., Тарала Л.В., Медяник Е.В., Малявин Ф.Ф., Лапин В.А., Бедраков Д.П. Синтез керамического порошка иттрий-алюминиевого граната, легированного рутением. *Физико-химические аспекты изучения кластеров, наноструктур и наноматериалов*. 2024;16:1016–1024.
https://doi.org/10.26456/pcascnn/2024.16.1016

22. Kravtsov A.A., Nikova M.S., Vakalov D.S., Tarala V.A., Chikulina I.S., Malyavin F.F., Chapura O.M., Krandievsky S.O., Kuleshov D.S., Lapin V.A. Combined effect of MgO sintering additive and stoichiometry deviation on YAG crystal lattice defects. *Ceramics International*. 2019;45(16):20178–20188.
https://doi.org/10.1016/j.ceramint.2019.06.287

23. Jing W. , Li F., Yu S., Ji X., Xu T., Zhang J., Pan Z., Yuan Z., Kang B., Deng J., Yin W., Huang H. High efficiency synthesis of Nd:YAG powder by a spray co-precipitation method for transparent ceramics. *Journal of the European Ceramic Society*. 2018;38(5):2454–2461.
https://doi.org/10.1016/j.jeurceramsoc.2017.12.059

24. Kravtsov A.A., Chapura O.M., Tarala V.A., Medyanik E.V., Tarala L.V., Suprunchuk V.E., Malyavin F.F., Kuznetsov S.V., Tsvetkov V.S., Dobretsova E.A., Kalachev Y.L., Lapin V.A. Fabrication and characterization of LuAG: Er ceramics with high optical transmission. *Journal of the European Ceramic Society*. 2025;45(3):117033.
https://doi.org/10.1016/j.jeurceramsoc.2024.117033

25. Ru Y., Jie Q., Min L., Guoqiang L. Synthesis of yttrium aluminum garnet (YAG) powder by homogeneous precipitation combined with supercritical carbon dioxide or ethanol fluid drying. *Journal of the European Ceramic Society*. 2008;28(15):2903–2914.
https://doi.org/10.1016/j.jeurceramsoc.2008.05.005

26. Zhang W., Lu T., Wei N., Ma B., Li F., Lu Z., Qi J. Effect of annealing on the optical properties of Nd:YAG transparent ceramics. *Optical Materials*. 2012;34(4):685–690.
https://doi.org/10.1016/j.optmat.2011.10.001

27. Huang C.H., Zhang G., Chen Z.Q., Huang X.J., Shen H.Y. Calculation of the absorption coefficients of optical materials by measuring the transmissivities and refractive indices. *Optics & Laser Technology*. 2002;34(3):209–211.
https://doi.org/10.1016/S0030-3992(01)00112-8

Information about the Authors

Viktoria E. Suprunchuk – Cand. Sci. (Chem.), Associate Professor, Senior Researcher, Sector of Nanopowder for Synthesis, Research Laboratory Advanced Materials and Laser Media (RL AMLM), North-Caucasus Federal University (NCFU)
ORCID: 0000-0002-5587-8262
E-mail: vikasuprunchuk@gmail.com

Alexander A. Kravtsov – Cand. Sci. (Eng.), Head, Sector of Nanopowder Synthesis, RL AMLM, NCFU
ORCID: 0000-0002-0645-1166
E-mail: sanya-kravtsov@yandex.ru

Vyacheslav A. Lapin – Cand. Sci. (Eng.), Senior Researcher, Sector of Physicochemical Methods of Analysis, RL AMLM, NCFU
ORCID: 0000-0002-1938-4134
E-mail: viacheslavlapin@yandex.ru

Fedor F. Malyavin – Head, Ceramics Sintering Sector, RL AMLM, NCFU
ORCID: 0000-0002- 5255-9346
E-mail: fedormalyavin@mail.ru

Dmitry P. Bedrakov – Engineer, Operations and Maintenance Sector, RL AMLM, NCFU
ORCID: 0009-0001-8207-7436
E-mail: dima.bedracov@mail.ru

Сведения об авторах

Виктория Евгеньевна Супрунчук – к.х.н., доцент, ст. науч. сотрудник Сектора синтеза нанопорошков Научно-исследовательской лаборатории перспективных материалов и лазерных сред (НИЛ ПМиЛС) Северо-Кавказского федерального университета (СКФУ)
ORCID: 0000-0002-5587-8262
E-mail: vikasuprunchuk@gmail.com

Александр Александрович Кравцов – к.т.н., зав. Сектором синтеза нанопорошков НИЛ ПМиЛС, СКФУ
ORCID: 0000-0002-0645-1166
E-mail: sanya-kravtsov@yandex.ru

Вячеслав Анатольевич Лапин – к.т.н., ст. науч. сотрудник Сектора физико-химических методов исследования и анализа НИЛ ПМиЛС, СКФУ
ORCID: 0000-0002-1938-4134
E-mail: viacheslavlapin@yandex.ru

Федор Федорович Малявин – зав. Сектором спекания керамики НИЛ ПМиЛС, СКФУ
ORCID: 0000-0002- 5255-9346
E-mail: fedormalyavin@mail.ru

Дмитрий Павлович Бедраков – инженер Сектора эксплуатации и обслуживания НИЛ ПМиЛС, СКФУ
ORCID: 0009-0001-8207-7436
E-mail: dima.bedracov@mail.ru

Contribution of the Authors

V. E. Suprunchuk – conceptualization; experimental work on sample preparation and synthesis; data analysis; writing and manuscript preparation.
A. A. Kravtsov – methodology; preliminary data analysis.

V. A. Lapin – physicochemical characterization of samples; participation in data interpretation.

Вклад авторов

В. Е. Супрунчук – концептуализация, проведение экспериментальной работы по подготовке и синтезу образцов, анализ результатов, написание и оформление статьи.
А. А. Кравцов – определение методики работы, проведение первичного анализа результатов.
В. А. Лапин – проведение физико-химического исследования образцов, участие в обсуждении результатов.

F. F. Malyavin – uniaxial pressing and vacuum sintering of ceramic powders; participation in discussion of results.

D. P. Bedrakov – polishing of ceramic specimens; participation in discussion of results.

Ф. Ф. Малявин – проведение прессования и спекания подготовленных керамических порошков под вакуумом, участие в обсуждении результатов.

Д. П. Бедраков – проведение полировки керамики, участие в обсуждении результатов.

Received 07.04.2025
Revised 24.07.2025
Accepted 06.08.2025

Статья поступила 07.04.2025 г.
Доработана 24.07.2025 г.
Принята к публикации 06.08.2025 г.

Refractory, Ceramic, and Composite Materials
Тугоплавкие, керамические и композиционные материалы

UDC 669.715; 69.2.8
https://doi.org/10.17073/1997-308X-2025-6-44-51

Research article
Научная статья

Aluminum matrix composites Al–SiO_2 produced using amorphous microsilica

M. P. Kuz'min ✉, **M. Yu. Kuz'mina, A. S. Kuz'mina**

Irkutsk National Research Technical University
83 Lermontov Str., Irkutsk 664074, Russia

✉ mike12008@yandex.ru

Abstract. Studies were carried out to develop aluminum matrix composites reinforced with amorphous microsilica particles. The feasibility of producing Al–5 wt. % SiO_2 materials using both stirring-assisted casting and semisolid metal processing was established. The latter method, when combined with subsequent squeeze casting, demonstrated the highest efficiency. Magnesium was shown to function as a surface-active additive that removes oxygen from the surfaces of the dispersed particles and enhances the mechanical properties of the composite during heat treatment. The resulting material exhibits a uniform distribution of microsilica particles throughout the aluminum matrix and demonstrates hardness, corrosion resistance, and reduced specific weight superior to those of the base AlSi7 alloy. Therefore, the composites produced using the developed technology are promising for applications in transport engineering as well as in the aerospace and space industries.

Keywords: aluminum, composite materials, aluminum matrix composites, silicon dioxide, amorphous microsilica, stirred casting, semisolid metal processing, squeeze casting

For citation: Kuz'min M.P., Kuz'mina M.Yu., Kuz'mina A.S. Aluminum matrix composites Al–SiO_2 produced using amorphous microsilica. *Powder Metallurgy and Functional Coatings*. 2025;19(6):44–51. https://doi.org/10.17073/1997-308X-2025-6-44-51

Получение алюмоматричных композитов Al–SiO_2 с использованием аморфного микрокремнезема

М. П. Кузьмин ✉, **М. Ю. Кузьмина, А. С. Кузьмина**

Иркутский национальный исследовательский технический университет
Россия, 664074, г. Иркутск, ул. Лермонтова, 83

✉ mike12008@yandex.ru

Аннотация. Проведены исследования, направленные на получение алюмоматричных композитов, армированных частицами аморфного микрокремнезема. Установлена возможность получения материалов системы Al–5SiO_2 (мас. %) с использованием методов литья с интенсивным перемешиванием и полутвердого металлического литья. Наибольшую эффективность продемонстрировал второй способ с последующей жидкой штамповкой. Показана возможность использования магния в качестве поверхностно-активной добавки, способствующей удалению кислорода с поверхности дисперсных частиц и улучшению механических свойств композиционного материала в процессе термообработки. Полученный композит имеет равномерное распределение дисперсных частиц микрокремнезема в объеме металла, обладает твердостью, коррозионной стойкостью и удельным весом, превосходящими аналогичные характеристики исходного алюминиевого сплава. Таким образом, полученные с использованием разработанной технологии материалы могут быть востребованы во всех сферах транспортного машиностроения, а также в отраслях авиационной и космической промышленности.

Ключевые слова: алюминий, композиционные материалы, алюматричные композиты, диоксид кремния, аморфный микрокремнезем, литье с перемешиванием, полутвердое металлическое литье, жидкая штамповка

Для цитирования: Кузьмин М.П., Кузьмина М.Ю., Кузьмина А.С. Получение алюматричных композитов Al–SiO_2 с использованием аморфного микрокремнезема. *Известия вузов. Порошковая металлургия и функциональные покрытия*. 2025; 19(6):44–51. https://doi.org/10.17073/1997-308X-2025-6-44-51

Introduction

The advancement of modern engineering is inseparable from the use of materials – both alloys and composites – possessing specific physical, chemical, mechanical, and operational properties, as well as from the continuous improvement of technologies for their production.

The development of composite materials consisting of a metallic matrix reinforced by dispersed particles is among the highest-priority directions in contemporary metallurgy and materials science. In many cases, only composites can meet the stringent requirements of advanced engineering applications, which increasingly demand higher loads, operational speeds, temperatures, environmental aggressiveness, and reduced structural weight. Among metal-matrix composites, aluminum-based systems are the most widely used owing to their high specific strength, low density, and advantageous combinations of mechanical and operational properties [1–10].

A broad range of technologies is available for the fabrication of aluminum matrix composites (AMCs), including powder metallurgy, mechanical dispersion, liquid metal infiltration, and various casting techniques [1; 4; 11]. Casting assisted by intensive stirring is the most accessible and widely employed method. This process involves introducing reinforcing particles into molten aluminum followed by mechanical or electromagnetic stirring [12–14]. A known limitation of this method is the agglomeration of the added particles due to their inherently low wettability in an aluminum melt [15].

Several studies have demonstrated that semisolid metal processing (SSM) represents one of the most cost-effective approaches to producing aluminum matrix composites. In this method, the melt is processed within the temperature interval between liquidus and solidus, where the alloy exhibits a slurry-like rheology, enhancing particle incorporation [16; 17]. Three closely related SSM routes are distinguished: thixocasting, rheocasting, and thixomolding [18–20]. To reduce porosity and refine the microstructure of finished products, high-pressure die casting is commonly applied as an auxiliary step [21]. Most research on AMCs focuses on reinforcing particles such as Al_2O_3, ZrO_2, MgO, SiC, as well as carbon nanotubes [10–30]. The use of dispersed reinforcing materials is limited by the technological complexity of composite fabrication and by their cost, which is strongly influenced by market conditions and varies significantly among different types of ceramic powders depending on their chemical composition, particle size, and degree of purity.

In recent years, significant effort has been directed to ward reducing the cost of AMC production by employing inexpensive and widely available raw materials. In this study, microsilica – an ultrafine material composed of spherical SiO_2 particles – is used as a modifying agent [4; 5]. Depending on the manufacturer, its market price ranges from 550 to 870 USD/t. A promising route to cost reduction is the use of dust collected from gas-cleaning systems of silicon-production furnaces as a low-cost source of microsilica (~1500 RUB/t) [11].

The aim of the present study was to develop a method for producing Al–SiO_2 composites containing up to 5 wt. % of reinforcing particles using intensive stirring casting and semisolid metal processing, and to evaluate the influence of SiO_2 particles on their microstructure and properties.

Materials and methods

For the laboratory studies aimed at producing composites using amorphous silica, a hypoeutectic AlSi7 silumin alloy was used as the matrix metal; its chemical composition was as follows (wt. %):

Si	7.00
Fe	0.19
Mg	0.25
Mn	0.10
Cu	0.05
Zn	0.07
Ga	0.001

Amorphous microsilica was collected from the gas-cleaning system of JSC Kremniy (Shelekhov, Russia) and enriched by flotation [17]. To improve the wettability of the microsilica particles and suppress agglomeration during their introduction into the melt,

the powder was subjected to ultrasonic treatment in acetone, rinsing with distilled water, drying, and subsequent heat treatment at 200–300 °C. In parallel with thermal conditioning of the microsilica, the melt was alloyed with magnesium, added as MG-90 master alloy in an amount of 1 wt. % to enhance interfacial wetting.

Two processing routes were employed to produce the aluminum matrix composites:

– intensive mechanical stirring followed by gravity casting;

– semisolid metal processing followed by squeeze casting.

To enable an objective comparison of the microstructure and physicomechanical properties, the base aluminum alloy was remelted using the continuous casting method.

During stirred casting, microsilica particles were introduced at 730 °C, whereas in semisolid processing they were introduced at 585–615 °C, i.e., between the solidus and liquidus temperatures of the AlSi7 alloy. All subsequent casting operations were performed at temperatures above the liquidus (730 °C). The SiO_2 particles, preheated to 200–300 °C, were fed into the melt at 5 g/min while the melt was stirred with a rotor at 200 rpm. The final forming step consisted of squeeze casting on a 25-ton hydraulic press. After that, the ingots were subjected to heat treatment at 500 °C for 14 h, followed by quenching in warm water (70 °C) and precipitation, or age hardening, at 165 °C for 8 h. The T6 heat-treatment mode was applied to both the unreinforced alloy and the composite and consisted of solution treatment at 525 °C for 12 h, followed by quenching in warm water at 80 °C and aging at 165 °C for 8 h.

Phase analysis was performed using a Shimadzu XRD-7000 diffractometer within a 2θ range of 10–70°. Microstructural analysis in secondary-electron and backscattered-electron modes was carried out using a JEOL JIB-4500 scanning electron microscope equipped with an Oxford Instruments X-Max EDS detector. Metallographic observations were conducted using an Olympus GX-51 optical microscope. Hardness was measured using a Zwick Brinell hardness tester with a 2.5-mm indenter and a 62.5-kg load. Corrosion behavior was examined by potentiodynamic polarization using a three-electrode cell with a saturated calomel reference electrode and platinum counter electrode. Density was measured by hydrostatic weighing according to GOST 8.568-97. Cubic samples (10 mm edge length) were degreased and dried at 105 °C for 1 h to remove adsorbed moisture.

Results and discussion

SEM images of the spherical microsilica particles (Fig. 1) reveal a wide particle-size distribution and the adhesion of smaller particles to the surfaces of larger spheres due to their high surface energy (Fig. 1, *b*).

The microsilica used in this study had the following chemical composition (wt. %):

SiO_2	95.0
Al_2O_3	0.55
Fe_2O_3	0.61
CaO	0.96
MgO	1.21
Na_2O	0.31
K_2O	0.84
C	0.25
S	0.27

Fig. 2, *a* shows the microstructure of the initial hypoeutectic AlSi7 silumin, consisting of dendrites of the aluminum solid solution (α-Al) and the α-Al + Si eutectic located in the interdendritic regions.

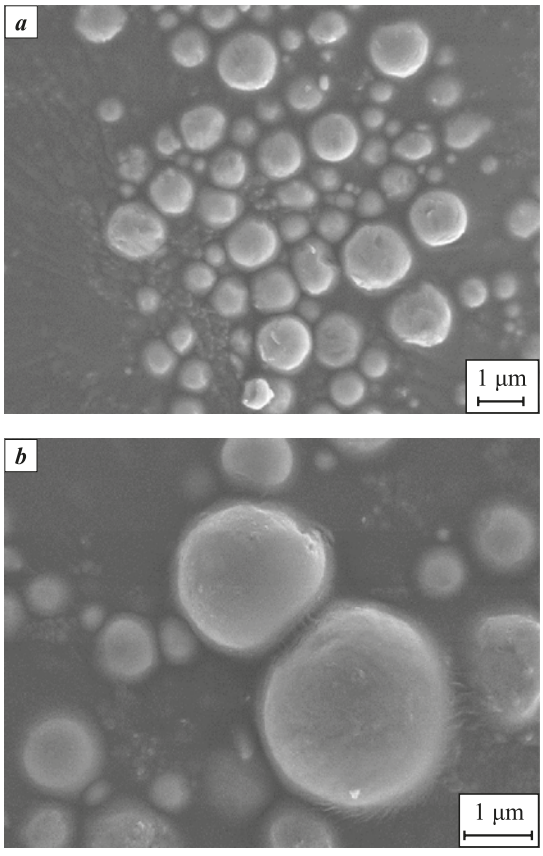

Fig. 1. SEM images of microsilica particles

Рис. 1. СЭМ-изображения частиц микрокремнезема

The AlSi7 alloy produced by high-pressure die casting exhibits a refined microstructure with an average grain size of 15 μm and no shrinkage or gas porosity. The microstructure of the Al–SiO_2 composite produced by casting with intensive mechanical stirring and subsequent pouring at 720 °C (Fig. 2, *b*) is characterized by agglomeration of the microsilica particles and the formation of regions of shrinkage porosity. This indicates a high degree of SiO_2 particle agglomeration, which increases in direct proportion to the casting temperature.

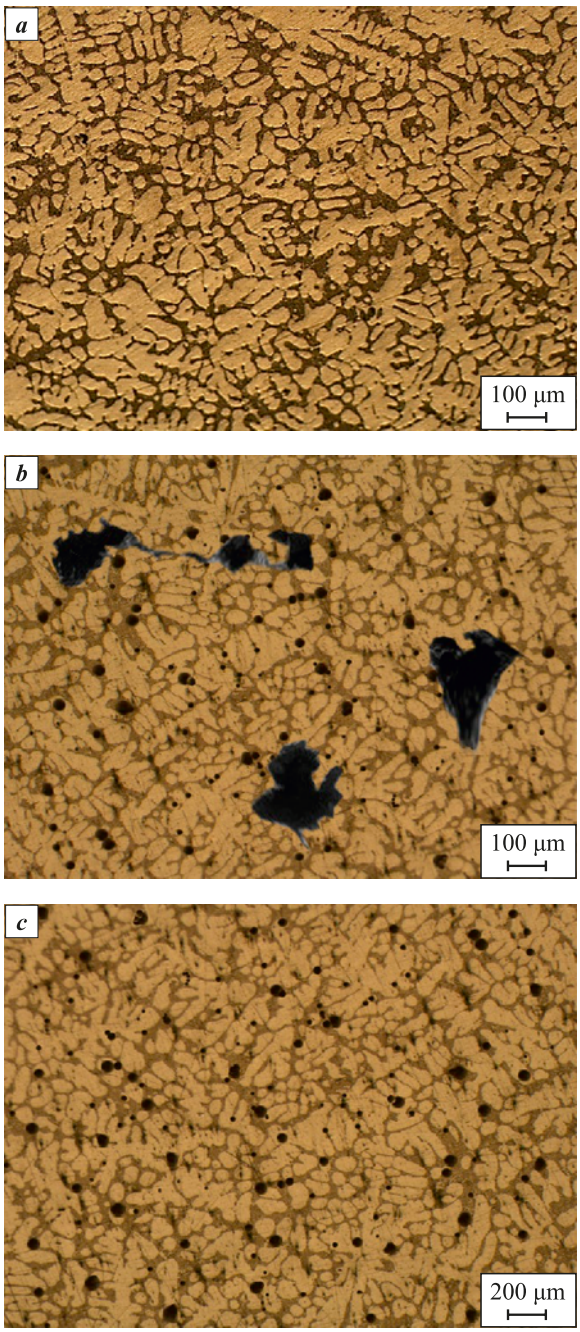

Fig. 2. Microstructures of the base AlSi7 alloy (***a***), the composite produced by casting with intensive mechanical stirring (***b***), and the composite produced by semisolid metal processing (***c***)

Рис. 2. Микроструктуры исходного алюминиевого сплава AlSi7 (***a***), композита, полученного литьем с интенсивным механическим перемешиванием (***b***), и композита, полученного методом полутвердого металлического литья (***c***)

Fig. 2, *c* presents the microstructure of the Al–SiO_2 composite fabricated via semisolid metal processing at 600 °C with intensive mechanical stirring followed by squeeze casting. Under these conditions, the composite exhibits a uniform distribution of the microsilica particles throughout the material, to gether with grain refinement and the elimination of shrinkage porosity. Because the squeeze-casting process allows the metal to be processed in the form of a semisolid slurry, the dispersed reinforcing particles become highly uniformly distributed and their agglomeration is effectively prevented.

Semisolid processing was conducted within the temperature interval between the liquidus and solidus, during which the alloy containing primary α-Al dendrites was stirred at 590 °C. Processing the alloy in this semisolid state enabled a uniform distribution of the SiO_2 particles throughout the matrix – an outcome that could not be achieved by intensive stirring of the fully molten metal. The diffraction pattern of this sample shows reflections corresponding to Al, Si, and SiO_2 (Fig. 3). The most intense peaks arise from metallic aluminum (2θ = 28.7°, 32.4°, 43.5°), crystalline silicon (2θ = 35.1°, 47.4°, 57.5°, 68.4°), silicon dioxide (2θ = 25.5°, 38.1°, 45.3°, 52.7°, 57.3°, 66.5°), and aluminum oxide (2θ = 37.6°, 41.9°, 44.8°). *X*-ray diffraction also revealed the presence of $MgAl_2O_4$ and $Mg_{17}Al_{12}$, formed as a result of the additional

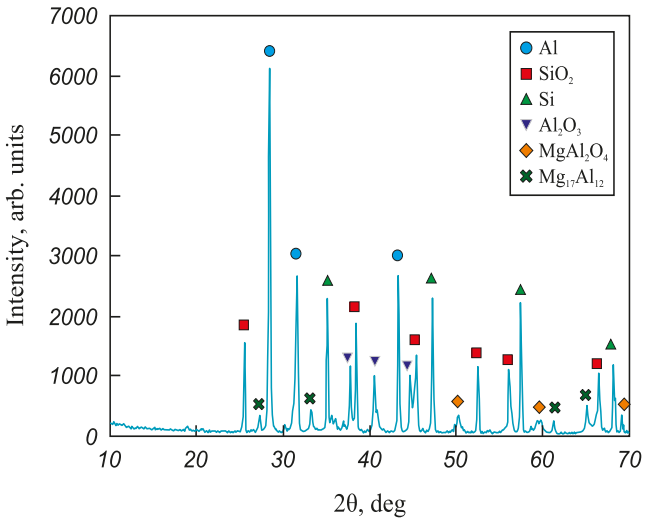

Fig. 3. Diffraction pattern of the Al–SiO_2 composite in the 2θ range of 10÷70°

Рис. 3. Дифрактограмма композита Al–SiO_2 в диапазоне 2θ = 10÷70°

magnesium introduced into the base silumin alloy. Magnesium improves the wettability of the microsilica particles by the aluminum matrix through the formation of $MgAl_2O_4$ spinel, which removes surface oxides [10; 17]. The $Mg_{17}Al_{12}$ phase formed during heat treatment further contributes to strengthening of the composite.

The results show that the SiO_2 content in the composite material matches the target value of 5 wt. %. This demonstrates that the amount of dispersed particles introduced into the aluminum matrix can be accurately controlled. However, to avoid the formation of the Al_3Mg_2 intermetallic phase, which degrades the strength of the composite, the magnesium addition to the aluminum matrix should be limited to 2 wt. %.

Brinell hardness data for the cast AlSi7 silumin and the composites produced from it by the different processing routes are presented in Fig. 4. These results indicate that the incorporation of amorphous microsilica particles into the cast silumin, provided they are uniformly distributed, leads to an increase in hardness. The SiO_2 particles in the aluminum matrix act as nucleation centers and promote grain refinement, while the mismatch in the coefficients of thermal expansion between the microsilica and the matrix alloy generates interfacial strain, which serves as a barrier to dislocation motion.

The hardness of the composite materials is governed primarily by the processing route and by the degree of dispersion of the reinforcing particles. The composite obtained by casting with intensive mechanical stirring shows, even after heat treatment, a marked reduction in hardness relative to the base AlSi7 alloy. This deterioration is associated with the pronounced agglomeration of microsilica particles and the resulting formation of shrinkage porosity. By contrast, the composite produced by semisolid metal processing followed by squeeze casting exhibits the highest hardness. This improvement is due to the more uniform dispersion of microsilica throughout the matrix and to grain refinement caused by crystallization under pressure in the presence of numerous nucleation sites.

The tensile strength of the composite produced by semisolid metal processing was 257 MPa, which is essentially equal to that of the base AlSi7 alloy (σ_b = 269 MPa). In addition to its high strength, this composite showed enhanced corrosion resistance (Fig. 5). This enhancement is attributed to the formation of interfacial reaction products arising from the interaction of aluminum, magnesium, and microsilica, which are less susceptible to corrosive attack. Phases such as $MgAl_2O_4$, Al_2O_3, and SiO_2 form a protective oxide layer on the material surface.

The density of the composite obtained by casting with intensive mechanical stirring is slightly lower (2.58 g/cm^3) than that of the base alloy (2.64 g/cm^3). This reduction is explained by the presence of shrinkage porosity and agglomerates of SiO_2 particles, as revealed by microstructural analysis (Fig. 2, *b*).

The lowest density (2.47 g/cm^3) was measured for the composite produced by semisolid casting followed by squeeze casting. Despite its lower density, this material exhibited the best mechanical properties and

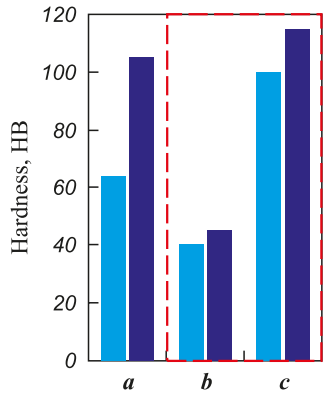

Fig. 4. Brinell hardness of the base AlSi7 alloy (***a***) and of the composites produced by casting with intensive mechanical stirring (***b***), and by semisolid metal processing (***c***)

– Al; – Al + SiO_2

Рис. 4. Твердость исходного алюминиевого сплава AlSi7 (***a***) и композитов, полученных литьем с интенсивным механическим перемешиванием (***b***) и методом полутвердого металлического литья (***c***)

– Al; – Al + SiO_2

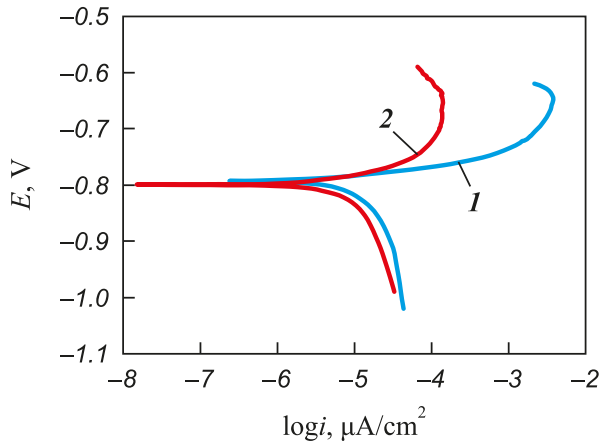

Fig. 5. Potentiodynamic polarization curves of the base AlSi7 alloy (***1***) and the composite produced by semisolid metal processing (***2***)

Рис. 5. Кривые потенциодинамической поляризации исходного алюминиевого сплава AlSi7 (***1***) и композита, полученного методом полутвердого металлического литья (***2***)

no macroporosity. The main reasons for the reduced density in this case are.

1. The presence of a low-density reinforcing phase. Amorphous SiO_2 particles have a density of about 2.2 g/cm^3, which is lower than that of the aluminum matrix (~2.7 g/cm^3). The addition of 5 wt. % SiO_2 therefore naturally reduces the overall density of the composite.

2. Densification under pressure. Squeeze casting produces a material with a more homogeneous microstructure and minimal porosity, as confirmed by the micrographs (Fig. 2, *c*).

Thus, in this case the decrease in density is not associated with defects but rather with the uniform distribution of the lightweight ceramic phase within the metallic matrix.

Conclusions

This study confirms the feasibility of producing Al–SiO_2 composites using intensive stirring casting and semisolid metal processing with subsequent squeeze casting. The latter method proved most effective, enabling the fabrication of composites containing 5 wt. % uniformly distributed microsilica particles. The results showed that magnesium enhances the wettability of the dispersed microsilica particles by removing oxygen from their surfaces and by suppressing further oxide formation through the generation of the $MgAl_2O_4$ intermetallic phase. An improvement in the mechanical properties of the composite during heat treatment was also observed, which is attributed to the formation of the $Mg_{17}Al_{12}$ phase. The resulting composite exhibited higher hardness and superior corrosion resistance compared to the base AlSi7 alloy.

The proposed processing routes – casting with intensive mechanical stirring and semisolid metal processing – enable the production of Al–SiO_2 composites with high strength, excellent corrosion resistance, and low porosity, making them promising for transport engineering as well as the aviation and aerospace industries. The findings expand current understanding of the use of micro- and nanoscale powders as alloying and modifying agents in next-generation composite materials.

Список литературы / References

1. Pattnayak A., Madhu N., Sagar Panda A., Kumar Sahoo M., Mohanta K. A Comparative study on mechanical properties of Al–SiO_2 composites fabricated using rice husk silica in crystalline and amorphous form as reinforcement. *Materials Today: Proceedings*. 2018;5(2): 8184–8192. https://doi.org/10.1016/j.matpr.2017.11.507
2. Malek A., Abderraouf Gh. Synthesis and characterization of Al–SiO_2 composites. *Journal of Ceramic Processing Research*. 2019;20(3):259–263. https://doi.org/10.36410/jcpr.2019.20.3.259
3. Nalivaiko A. Yu., Arnautov A.N., Zmanovsky S.V., Ozherelkov D.Yu., Shurkin P.K., Gromov A.A. Al–Al_2O_3 powder composites obtained by hydrothermal oxidation method: Powders and sintered samples characterization. *Journal of Alloys and Compounds*. 2020;825:154024. https://doi.org/10.1016/j.jallcom.2020.154024
4. Kuz'min M.P., Ivanov N.A., Kondrat'ev V.V., Kuz'mina M.Yu., Begunov A.I., Kuz'mina A.S., Ivanchik N.N. Preparation of aluminum–carbon nanotubes composite material by hot pressing. *Metallurgist*. 2018;61(3):815–821. https://doi.org/10.1007/s11015-018-0569-2

   Кузьмин М.П., Иванов Н.А., Кондратьев В.В., Григорьев В.Г., Кузьмина М.Ю., Бегунов А.И., Кузьмина А.С., Иванчик Н.Н. Получение композиционного материала «алюминий–углеродные нанотрубки» методом горячего прессования. *Металлург*. 2017;61(9):97–102.
5. Kuz'min M.P., Kondrat'ev V.V., Larionov L.M., Kuz'mina M.Y., Ivanchik N.N. Possibility of preparing alloys of the Al–Si system using amorphous microsilica. *Metallurgist*. 2017;60(5):86–91. https://doi.org/10.1007/s11015-017-0458-0

   Кузьмин М.П., Иванов Н.А., Кондратьев В.В., Григорьев В.Г., Кузьмина М.Ю., Бегунов А.И., Кузьмина А.С., Иванчик Н.Н. Получение композиционного материала «алюминий–углеродные нанотрубки» методом горячего прессования. *Металлург*. 2017;61(1):101–105.
6. Sathish T., Chandramohan D. Teaching methods and methodologies used in laboratories. *International Journal of Recent Technology and Engineering*. 2019;7(6):291–293.
7. Lepezin G.G., Kargopolov S.A., Zhirakovskii V.Yu. Sillimanite group minerals: A new promising raw material for the Russian aluminum industry. *Russian Geology and Geophysics*. 2010:51(12):1247–1256. https://doi.org/10.1016/j.rgg.2010.11.004

   Лепезин Г.Г., Каргополов С.А., Жираковский В.Ю. Минералы группы силлиманита как новое перспективное сырье для алюминиевой промышленности России. *Геология и геофизика*. 2010;51(12):1605–1617.
8. Bakker H. Enthalpies in alloys. Miedema's semi-empirical model. Switzerland: Trans Tech Publications. Ltd., 1998. 195 p.
9. Saravanan K.S., Pradhan Raghuram A., Ramya S., Senthilnathan K. Characterization of Al–SiO_2 composite material. *International Journal of Engineering and Advanced Technology*. 2019;9(2):2972–2975. https://doi.org/10.35940/ijeat.B3898.129219
10. Pai B.C., Ramani G., Pillai R.M., Satyanarayana K.G. Role of magnesium in cast aluminium alloy matrix composites. *Journal of Materials Science*. 1995;30(8):1903–1911. https://doi.org/10.1007/BF00353012
11. Kuz'min M.P., Larionov L.M., Chu P.K., Qasim A.M., Kuz'mina M.Yu., Kondratiev V.V., Kuz'mina A.S., Jia Q. Ran new methods of obtaining Al–Si alloys using amorphous microsilica. *International Journal of Metalcasting*. 2020;14(1):207–217. https://doi.org/10.1007/s40962-019-00353-w

12. Gowri Shankar M.C., Jayashree P.K., Kini A.U., Sharma S.S. Effect of silicon oxide (SiO_2) reinforced particles on ageing behavior of Al–2024 Alloy. *International Journal of Mechanical Engineering and Technology*. 2014: 5(9):15–21.

13. Kok M. Production and mechanical properties of Al_2O_3 particle-reinforced 2024 aluminum alloy composites. *Journal of Materials Processing Technology*. 2005;161(3): 381–387. https://doi.org/10.1016/j.jmatprotec.2004.07.068

14. Taha M.A., El-Mahallawy N.A. Metal–matrix composites fabricated by pressure assisted infiltration of loose ceramic powder. *Journal of Materials Processing Technology*. 1998;73(1-3):139–146. https://doi.org/10.1016/S0924-0136(97)00223-9

15. Sajjadi S.A., Ezatpour H.R., Parizi M.T. Comparison of microstructure and mechanical properties of A356 aluminum alloy /Al_2O_3 composites fabricated by stir and compo–casting processes. *Materials and Design*. 2012;34: 106–111. https://doi.org/10.1016/j.matdes.2011.07.037

16. Abbasipour B., Niroumand B., Monir vaghefi S.M. Compocasting of A356–CNT composite. *Transactions of Nonferrous Metals Society of China*. 2010;20(9):1561–1566. https://doi.org/1010.1016/S1003-6326(09)60339-3

17. Kuz'min M.P., Paul K. Chu, Abdul M. Qasim, Larionov L.M., Kuz'mina M.Yu., Kuz'min P.B. Obtaining of Al–Si foundry alloys using amorphous microsilica – Crystalline silicon production waste. *Journal of Alloys and Compounds*. 2019;806(4-6):806–813. https://doi.org/10.1016/j.jallcom.2019.07.312

18. Robie A.R., Hemingway B.S. Thermodynamic properties of minerals and related substances at 298,15 K and 1 bar (10^5 pascals) pressure and at higher temperatures. Washington: United States Government Printing Office; 1995. 461 p.

19. Sajjadi S.A., Torabi Parizi M., Ezatpoura H.R., Sedghic A. Fabrication of A356 composite reinforced with micro and nano Al_2O_3 particles by a developed compocasting method and study of its properties. *Journal of Alloys and Compounds*. 2012;511(1):226–231. https://doi.org/10.1016/j.jallcom.2011.08.105

20. Cocen L., Onel K. The production of Al–Si alloy–SiC_p composites via compocasting: some microstructural aspects. *Materials Science and Engineering: A*. 1996; 221(1-2):187–191. https://doi.org/10.1016/s0921-5093(96)10436-6

21. Escalera-Lozano R., Gutierrez C.A., Pech-Canul M.A. Pech-Canul M.I. Corrosion characteristics of hybrid Al/SiC_p/$MgA1_2O_4$ composites fabricated with fly ash and recycled aluminum. *Materials Characterization*. 2007;58(10):953–960. https://doi.org/10.1016/j.matchar.2006.09.012

22. Munasir M., Triwikantoro T., Zainuri M., Bäßler R., Darminto D. Mechanical strength and corrosion rate of aluminium composites (Al/SiO_2): Nanoparticle silica (NPS) as reinforcement. *Journal of Physical Science*. 2019;30(1):81–97. https://doi.org/10.21315/jps2019.30.1.7

23. Kuz'min M.P., Larionov L.M., Kondratiev V.V., Kuz'mina M.Yu., Grigoriev V.G., Knizhnik A.V., Kuz'mina A.S. Fabrication of silumins using silicon production waste. *Russian Journal of Non–Ferrous Metals*. 2019;60(5): 483–491. https://doi.org/10.3103/S1067821219050122

Кузьмин М.П., Ларионов Л.М., Кондратьев В.В., Кузьмина М.Ю., Григорьев В.Г., Книжник А.В., Кузьмина А.С. Получение силуминов с использованием отходов кремниевого производства. *Известия вузов. Цветная металлургия*. 2019;60(4):4–15. https://doi.org/10.17073/0021-3438-2019-4-4-15

24. Li G., Hao S., Gao W., Lu Z. The Effect of applied load and rotation speed on wear characteristics of Al–Cu–Li alloy. *Journal of Materials Engineering and Performance*. 2022:31 (1): 5875–5885. https://doi.org/10.1007/s11665-022-06613-x

25. Zheng Zh.-k., Ji Y.-j., Mao W.-m., Yue R., Liu Zh.-y. Influence of rheo-diecasting processing parameters on microstructure and mechanical properties of hypereutectic Al–30 % Si alloy. *Transactions of Nonferrous Metals Society of China*. 2017;27(6):1264–1272. https://doi.org/10.1016/S1003-6326(17)60147-X

26. Jeon J.H., Shin J.H., Bae D.H. Si phase modification on the elevated temperature mechanical properties of Al–Si hypereutectic alloys. *Materials Science and Engineering: A*. 2019;748(6):367–370. https://doi.org/10.1016/j.msea.2019.01.119

27. Apakashev R., Davydov S., Valiev N. High-temperature synthesis of composite material from Al–SiO_2. *System Components*. 2014;1064:58–61. https://doi.org/10.4028/www.scientific.net/AMR.1064.58

28. Feng H.K., Yu S.R., Li Y.L., Gong L.Y. Effect of ultrasonic treatment on microstructures of hypereutectic Al–Si alloy. *Journal of Materials Processing Technology*. 2008;208(1-3):330–350. https://doi.org/10.1016/J.JMATPROTEC.2007.12.121

29. Jiang B., Ji Z., Hu M., Xu H., Xu S. A novel modifier on eutectic Si and mechanical properties of Al–Si alloy. *Materials Letters*. 2019:239:13–16. https://doi.org/10.1016/j.matlet.2018.12.045

30. Lin Ch., Wu Sh.-s., Lü Sh.-l., Zeng J.-b., An P. Dry sliding wear behavior of rheocast hypereutectic Al–Si alloys with different Fe contents. *Transactions of Nonferrous Metals Society of China*. 2016;26(3):665–675. https://doi.org/10.1016/S1003-6326(16)64156-0

Information about the Authors

Сведения об авторах

Mikhail P. Kuz'min – Cand. Sci. (Eng.), Associate Professor, Department of Metallurgy of Non-Ferrous Metals, Irkutsk National Research Technical University (INRTU)
ORCID: 0000-0002-8714-5004
E-mail: mike12008@yandex.ru

Михаил Петрович Кузьмин – к.т.н., доцент кафедры металлургии цветных металлов Иркутского национального исследовательского технического университета (ИРНИТУ)
ORCID: 0000-0002-8714-5004
E-mail: mike12008@yandex.ru

Marina Yu. Kuz'mina – Cand. Sci. (Chem.), Associate Professor, Department of Metallurgy of Non-Ferrous Metals, INRTU
ORCID: 0000-0001-7215-5501
E-mail: kuzmina.my@yandex.ru

Alina S. Kuz'mina – Cand. Sci. (Phys.-Math.), Associate Professor, Department of Radioelectronics and Telecommunication Systems, INRTU
ORCID: 0000-0001-9553-5179
E-mail: kuzmina.istu@gmail.com

Марина Юрьевна Кузьмина – к.х.н., доцент кафедры металлургии цветных металлов, ИРНИТУ
ORCID: 0000-0001-7215-5501
E-mail: kuzmina.my@yandex.ru

Алина Сергеевна Кузьмина – к.ф.-м. н., доцент кафедры радиоэлектроники и телекоммуникационных систем, ИРНИТУ
ORCID: 0000-0001-9553-5179
E-mail: kuzmina.istu@gmail.com

Contribution of the Authors

M. P. Kuz'min – defined the research objective; developed the study methodology; participated in the discussion of the results; drafted the manuscript; reviewed and edited the final text.
M. Yu. Kuz'mina – defined the research objective; conducted the experimental investigations; drafted the manuscript; participated in the discussion of the results.
A. S. Kuz'mina – conducted the experimental investigations; drafted the manuscript; participated in the discussion of the results.

Вклад авторов

М. П. Кузьмин – определение цели работы, разработка методологии исследования, участие в обсуждении результатов, написание текста статьи, рецензирование и редактирование.
М. Ю. Кузьмина – определение цели работы, проведение экспериментальных исследований, написание текста статьи, участие в обсуждении результатов.
А. С. Кузьмина – экспериментальных исследований, написание текста статьи, участие в обсуждении результатов.

Received 27.03.2025
Revised 14.04.2025
Accepted 21.04.2025

Статья поступила 27.03.2025 г.
Доработана 14.04.2025 г.
Принята к публикации 21.04.2025 г.

Refractory, Ceramic, and Composite Materials
Тугоплавкие, керамические и композиционные материалы

UDC 666.7-121

https://doi.org/10.17073/1997-308X-2025-6-52-64

Research article
Научная статья

Effect of Cu additions and SHS charge compaction pressure on thermite-copper infiltration and the macrostructure of synthesized TiC–Cu cermets

E. A. Karakich ✉, E. R. Umerov, V. A. Novikov, P. E. Kichaev, A. P. Amosov

Samara State Technical University
244 Molodogvardeyskaya Str., Samara 443100, Russia

✉ maximcaracki4@gmail.com

Abstract. TiC–Cu ceramic–metal composites (cermets) have been extensively discussed in recent literature in terms of their properties and structure. However, in most cases the formation conditions considered involve the introduction of TiC particles into an overheated Cu melt. In the present work, samples were synthesized in air without crucible reactors by combining a thermite reaction to produce a copper melt for subsequent infiltration of a porous Ti + C powder charge and initiation of its combustion by self-propagating high-temperature synthesis (SHS) of titanium carbide. As a result, TiC–Cu cermets were formed. The effect of Cu addition to the Ti + C SHS charge and of compaction pressure on the completeness of infiltration by the copper melt generated during combustion of the copper thermite mixture is analyzed. The influence of these factors on the structure of the synthesized cermets is also examined. TiC–Cu cermets were synthesized with 5, 10, and 15 wt. % Cu added to SHS charges compacted at 22, 34, 45, 56, and 69 MPa. The completeness of infiltration was evaluated from the appearance of polished sections, microstructure, and phase composition. Optimal conditions were identified that provide composites with maximum density, minimal structural defects, the desired phase composition, and enhanced mechanical properties. The microstructure, composition, and physico-mechanical properties (density, Brinell hardness, compressive strength) of the new composites were investigated. It was established that the highest infiltration completeness and density of TiC–Cu samples are achieved at 10 wt. % Cu addition to the SHS charge and a compaction pressure of 45 MPa, while increasing Cu content in the charge leads to higher mechanical properties (hardness and compressive strength).

Keywords: self-propagating high-temperature synthesis, SHS-aluminothermy, copper, titanium carbide, infiltration

Acknowledgements: This study was supported by the Russian Science Foundation, project no. 24-79-10187, https://rscf.ru/project/24-79-10187/.

For citation: Karakich E.A., Umerov E.R., Novikov V.A., Kichaev P.E., Amosov A.P. Effect of Cu additions and SHS charge compaction pressure on thermite-copper infiltration and the macrostructure of synthesized TiC–Cu cermets. *Powder Metallurgy and Functional Coatings*. 2025;19(6):52–64. https://doi.org/10.17073/1997-308X-2025-6-52-64

Влияние добавки Cu и давления прессования СВС-шихты на инфильтрацию термитной меди и макроструктуру синтезированных керметов TiC–Cu

Е. А. Каракич, Э. Р. Умеров, В. А. Новиков, П. Е. Кичаев, А. П. Амосов

Самарский государственный технический университет
Россия, 443100, г. Самара, ул. Молодогвардейская, 244

maximcaracki4@gmail.com

Аннотация. В литературных источниках последних лет достаточно широко рассмотрены свойства и структура керамико-металлических композитов (керметов) системы TiC–Cu. Однако условия их образования в большинстве своем затрагивают случаи введения частиц TiC в перегретый расплав Cu. В данной работе образцы синтезировались на открытом воздухе без применения тиглей-реакторов путем сочетания термитной реакции для получения расплава меди, последующей инфильтрации пористой порошковой шихты Ti + C расплавом и инициации ее горения самораспространяющимся высокотемпературным синтезом (СВС) карбида титана. В результате образовывался кермет состава TiC–Cu. Представлен анализ влияния добавки меди в СВС-шихту Ti + C и давления ее прессования на полноту пропитки медным расплавом, полученным в результате горения медной термитной смеси. Также рассмотрено влияние вышеизложенных факторов на структуру синтезируемого кермета. Проведены исследования по синтезу керметов TiC–Cu при введении 5, 10, 15 мас. % Cu в СВС-шихты, спрессованные под давлением 22, 34, 45, 56, 69 МПа. Полнота инфильтрации определялась по внешнему виду шлифа сечения кермета, микроструктуре и составу. Определены оптимальные условия, при которых получаются композиты с наибольшей плотностью, наименьшим количеством дефектов структуры, заданным фазовым составом и высокими механическими характеристиками. Исследованы микроструктура, состав и физико-механические свойства (плотность, твердость по Бринеллю, прочность при сжатии) новых композитов. Установлено, что наибольшие полнота пропитки и плотность полученных образцов TiC–Cu достигаются при добавке меди в СВС-шихту в количестве 10 мас. % и давлении прессования СВС-шихты 45 МПа. Показано, что с увеличением доли меди в шихте возрастают значения механических свойств (твердость, предел прочности на сжатие).

Ключевые слова: самораспространяющийся высокотемпературный синтез, СВС-металлотермия, медь, карбид титана, инфильтрация

Благодарности: Исследование выполнено за счет гранта Российского научного фонда № 24-79-10187, https://rscf.ru/project/24-79-10187/

Для цитирования: Каракич Е.А., Умеров Э.Р., Новиков В.А., Кичаев П.Е., Амосов А.П. Влияние добавки Cu и давления прессования СВС-шихты на инфильтрацию термитной меди и макроструктуру синтезированных керметов TiC–Cu. *Известия вузов. Порошковая металлургия и функциональные покрытия*. 2025;19(6):52–64. https://doi.org/10.17073/1997-308X-2025-6-52-64

Introduction

Copper and copper-based alloys are widely used as structural materials in mechanical engineering due to their high electrical and thermal conductivity and chemical stability. However, these materials exhibit relatively low strength and wear resistance. Improving their mechanical and tribological properties remains an important task aimed at expanding the application range of copper and its alloys, increasing efficiency of use, and enhancing service life and operational reliability. Metal-matrix composites are actively being developed, in which a copper matrix is typically reinforced with hard and stiff particles of ceramics, intermetallics, carbon nanotubes, and similar phases [1–3]. To impart self-lubricating properties, the most common hardening phases include SiC [4], TiC [5], AlN [6], Al_2O_3 [7], TiB_2 [8], WC [9], as well as graphite [10], carbon nanotubes [11], and MoS_2 [12]. Titanium carbide is an attractive reinforcement for metallic matrices because it possesses a high elastic modulus, high hardness, a high melting point, and moderate electrical conductivity [13]. In addition, TiC exhibits virtually no interaction with copper; therefore, its incorporation into a copper matrix does not adversely affect the physical or electrical properties of TiC–Cu composites [14].

For producing TiC–Cu composites, powder metallurgy offers several established routes, including conventional sintering, microwave sintering, spark plasma sintering (SPS), and hot pressing. Minimizing residual porosity in such composites requires applying high pressure and temperature to achieve sufficient densification of the initial powder materials. The physical and mechanical properties of TiC–Cu composites are also

governed by the adhesion at the metal–ceramic interface, which is controlled by the wetting of TiC particles by molten copper. The wetting angle in the TiC–Cu system depends on both temperature and contact time: for example, at 1200 °C it decreases from 130 to 90° within 25 min [15]. Lower temperatures increase the wetting angle. Furthermore, oxidation of TiC surfaces decreases their wettability by molten copper because it inhibits the partial dissolution reactions of titanium carbide in copper that facilitate wetting [16].

The high temperatures and pressures required to fabricate TiC–Cu composites significantly complicate manufacturing and increase energy consumption, which affects their cost. In this regard, the method of self-propagating high-temperature synthesis (SHS) represents a promising basis for future energy-efficient fabrication technologies for TiC–Cu composites. SHS enables the synthesis of various ceramic compounds through a highly exothermic reaction that does not require external heating, proceeds in a self-sustaining regime, and can raise product temperatures to 2500–3000 °C [17]. For example, STIM-type alloys (synthetic hard tool materials) are produced by adding up to 40–50 vol. % of a metallic binder (copper, nickel, etc.) to an initial Ti + C powder mixture. After initiating the SHS reaction Ti + C → TiC, the binder metal melts, and pressure up to 180 MPa is applied. The resulting TiC–Cu composites can achieve a relative density of 99 % [18]. Further development of this method has led to the fabrication of TiC–Ti_xCu_y–Cu composites containing 48–68 %[1] TiC, 32–48 % Ti_xCu_y intermetallics, and up to 2.5 % free copper, exhibiting high abrasive resistance at hardness levels of 50–52 HRC [19].

A recently developed approach eliminates the need for external pressing equipment: SHS is used to produce porous TiC (or TiC mixed with the MAX-phase Ti_3SiC_2–TiC), followed by spontaneous infiltration with molten metal (Al, Sn, Cu) without applying external pressure [20–22]. However, when using copper melt generated solely by the heat of the SHS TiC reaction from the initial Cu powder, it was found that the available amount of molten copper was insufficient to fill the entire pore volume of the TiC preform. At the same time, preparing copper melt in a furnace at 1100 °C – i.e., using an external heat source – does not provide adequate wetting of TiC at this temperature, preventing spontaneous infiltration of molten copper into the TiC framework. The present work addresses this issue by employing a higher-temperature copper melt generated via the aluminothermic reaction $3CuO + 2Al \rightarrow Al_2O_3 + 3Cu$, which can heat the copper above its boiling point [23].

SHS can also proceed concurrently with a metallothermic reaction within a single highly exothermic reactive system used to synthesize ceramic–metal composite materials [24; 25]. In [26], TiC–Fe powders were produced via coupled reactions in $Fe_2O_3 + 2Al$ and Ti + C mixtures in an energy-saving and technologically simple mode. However, the product of the combined SHS and aluminothermic reaction was a highly porous Fe(Al)–Fe_3Al–Al_2O_3–TiC or TiC–Fe cermet that could be easily crushed into powder. To explore the possibility of producing a dense (or low-porosity) cermet, it is promising to separate the aluminothermic and SHS reactions into two independent reactive systems that generate a metal melt and a porous ceramic body (preform) separately. These can then be combined into a monolithic cermet through capillary wetting at the elevated temperature achieved during the aluminothermic and SHS processes.

Earlier [27], we developed a special graphite refractory reactor consisting of two cylindrical crucible-reactors positioned vertically. The working volume of the upper reactor serves for the aluminothermic reaction that produces the copper melt. The lower crucible holds the SHS Ti + C charge that forms the porous TiC ceramic preform. The two reaction chambers are separated by a graphite plate with an opening through which the thermite melt can flow into the lower crucible. To ensure phase separation between the molten copper and alumina produced during aluminothermy, the opening is covered by a copper or steel washer that delays the outflow of the thermite melt for several seconds.

In [28], it was demonstrated that SHS and aluminothermy can be combined without a special two-crucible setup by conducting the synthesis on an open sand substrate, where a compacted SHS briquette is simply surrounded by a copper-thermite mixture. TiC–Cu cermets were obtained in this manner, and it was shown that the compaction pressure of the SHS charge and the addition of 5 % copper significantly influence the phase composition of the materials, which – besides the main phases – may contain Ti_xCu_y intermetallics and free graphite. Proper optimization of the SHS charge composition and compaction pressure can ensure uniform TiC–Cu composites with minimized residual porosity and, consequently, enhanced physical and mechanical properties.

The objective of this study was to examine the effect of SHS charge compaction and Cu additions in the SHS mixture on the structure and mechanical properties of TiC–Cu composites produced by combining aluminothermy and SHS in air without refractory crucible reactors.

[1] Unless otherwise specified, all compositions are given in wt. %.

Materials and methods

Titanium carbide porous preforms were synthesized using titanium powder grade TPP-7 ($d \leq 300$ μm, purity 99 %) and carbon in the form of P701 carbon black ($d = 13$–70 nm, purity 99 %) to prepare a 15 g SHS Ti + C charge. Copper powder PMS-A ($d = 100$ μm, 99.5 %) was added in amounts of 0, 0.75, 1.5, and 2.25 g to reduce the combustion rate and obtain a more homogeneous TiC preform. A copper thermite mixture (TU 1793-002-12719185-2009), 40 g in total, served both as the SHS ignition source and as the primary source of molten copper. The mixed SHS charge with copper addition was uniaxially compacted using a manual press in a steel die of 23 mm diameter. The minimum compaction pressure was 22 MPa, which provided sufficient strength for handling and preserving the shape of the compact during combustion.

The samples were synthesized by combining aluminothermy and SHS in air without using refractory crucible reactors. Under these conditions, both the aluminothermic reaction $3CuO + 2Al \rightarrow Al_2O_3 + 3Cu$, with phase separation of the oxide and copper melts followed by release of the latter after melting a thin steel washer [27; 28], and the SHS process producing the porous TiC preform, occurred simultaneously. The overall experimental layout is shown in Fig. 1.

The compacted cylindrical SHS briquette was placed into a cavity formed in a sand substrate and uniformly covered with the copper thermite mixture. An electrical heating coil initiated the thermite reaction, whose thermal impulse triggered the SHS reaction. During combustion of the copper thermite mixture and formation of the copper melt, a sufficiently high temperature was reached to initiate SHS of the porous TiC preform, which was instantaneously infiltrated by the incoming molten copper through capillary action. As a result of synthesis and spontaneous infiltration, dense TiC–Cu cermet bodies were obtained.

The completeness of preform infiltration was preliminarily assessed by visual examination of polished sample surfaces (macrosections) and by density measurements using the Archimedes method. Microstructural analysis of the synthesized samples was performed using a JSM-7001F scanning electron microscope (Jeol, Japan). The phase composition of the synthesis products was determined by *X*-ray diffraction (XRD). Diffraction patterns were recorded on an automated ARL X'trA diffractometer (Thermo Scientific, Switzerland) using CuK_α radiation in continuous scan mode over $2\theta = 20$–$80°$ at 2°/min. The diffraction data were processed using the WinXRD software package. Hardness was measured according to the Brinell method using a 5 mm ball indenter

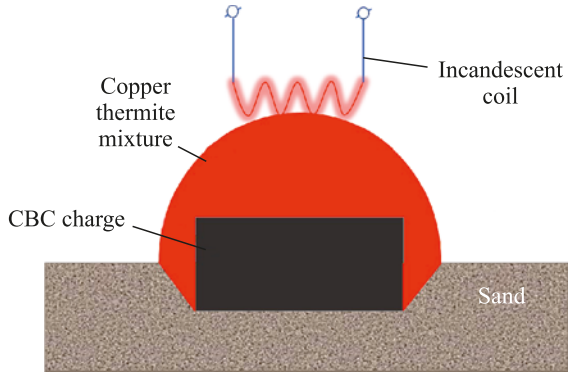

Fig. 1. Schematic representation of the combined aluminothermic reaction and SHS process used to produce ceramic–metal composite materials

Рис. 1. Схема сочетания реакции металлотермии и СВС для получения керамико-металлических композитов

at a load of 98 N in accordance with GOST 9012-59. Compression tests were carried out following GOST 25.503-97 on cylindrical samples with a diameter of 20.1 ± 0.1 mm and a height of 19.4 ± 0.8 mm using a Bluehill 3 testing machine (Instron, USA) at a cross-head speed of 1 mm/min.

Results and discussion

Fig. 2 shows macro-images of polished sections of the synthesized TiC–Cu cermet samples produced from the Ti + C SHS charge without Cu addition at different compaction pressures (P). Regardless of the applied pressure, the resulting samples contain numerous unfilled pores, pronounced delamination, and even cracking. At $P = 69$ MPa, the composite underwent complete destruction during synthesis.

Figs. 3–5 macro-images of polished sections of TiC–Cu cermet samples synthesized from SHS charges containing Cu at different compaction pressures.

Analysis of Fig. 3 shows that even a relatively small amount of copper (0.75 g) in the charge markedly affects the macrostructure of the resulting composites. The 5 % Cu addition significantly improves the infiltration completeness of the thermite copper melt into the synthesized TiC preform. As the compaction pressure increases, the defect morphology changes: at $P = 22$ MPa, the composite contains a considerable fraction of open pores, whereas higher pressures lead to progressively more complete infiltration across the sample cross-section. However, the nature of defects shifts from pore-dominated to crack-dominated.

When the Cu addition is increased to 10 %, all samples become infiltrated and exhibit only residual porosity (Fig. 4). At lower compaction pressures, infiltration remains incomplete (Fig. 4, *a*, *b*). Numerous small

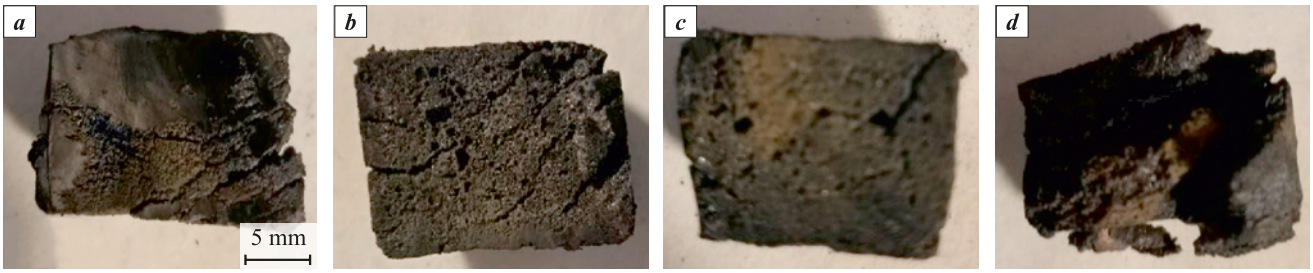

Fig. 2. Macro-images of polished sections of synthesized TiC–Cu cermet samples produced from the Ti + C SHS charge without Cu addition at different compaction pressures

P, MPa: 22 (***a***), 34 (***b***), 45 (***c***), 56 (***d***)

Рис. 2. Фотографии шлифов синтезированных образцов керметов TiC–Cu из СВС-шихты без добавки меди Ti + C при различных давлениях ее прессования

P, МПа: 22 (***a***), 34 (***b***), 45 (***c***), 56 (***d***)

pores and cracks are observed along the periphery of the samples. It is worth noting that at $P = 45$ MPa the samples show the lowest defect density among all conditions studied in this work, and infiltration occurs throughout the entire TiC preform volume. Further increases in compaction pressure lead to composite delamination and crack formation.

The samples with 15 % Cu exhibit an increased defect density in their macro-structure, accompanied by a change in defect morphology. In the micrographs shown in Fig. 5, individual isolated pores are almost completely absent; instead, the defects appear predominantly as clusters of fine pores arranged in crack-like formations.

The masses of the synthesized cermet samples obtained under different synthesis conditions – Cu addition to the SHS charge and compaction pressure – are listed in Table 1 and presented graphically in

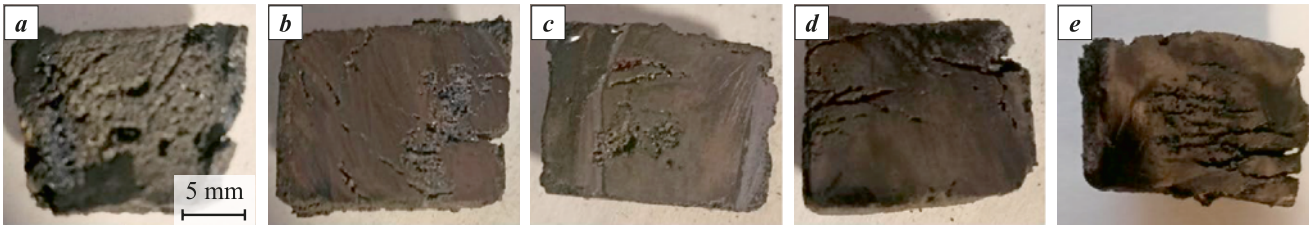

Fig. 3. Macro-images of polished sections of synthesized TiC–Cu cermet samples produced from the SHS charge with 5 % Cu addition at different compaction pressures

P, MPa: 22 (***a***), 34 (***b***), 45 (***c***), 56 (***d***), 69 (***e***)

Рис. 3. Фотографии шлифов синтезированных образцов керметов TiC–Cu из СВС-шихты с 5 %-ной добавкой меди при различных давлениях ее прессования

P, МПа: 22 (***a***), 34 (***b***), 45 (***c***), 56 (***d***), 69 (***e***)

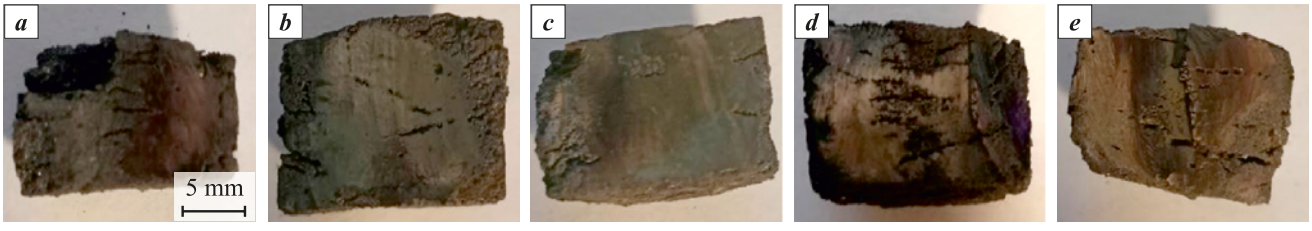

Fig. 4. Macro-images of polished sections of synthesized TiC–Cu cermet samples produced from the SHS charge with 10 % Cu addition at different compaction pressures

P, MPa: 22 (***a***), 34 (***b***), 45 (***c***), 56 (***d***), 69 (***e***)

Рис. 4. Фотографии шлифов синтезированных образцов керметов TiC–Cu из СВС-шихты с 10 %-ной добавкой меди при различных давлениях ее прессования

P, МПа: 22 (***a***), 34 (***b***), 45 (***c***), 56 (***d***), 69 (***e***)

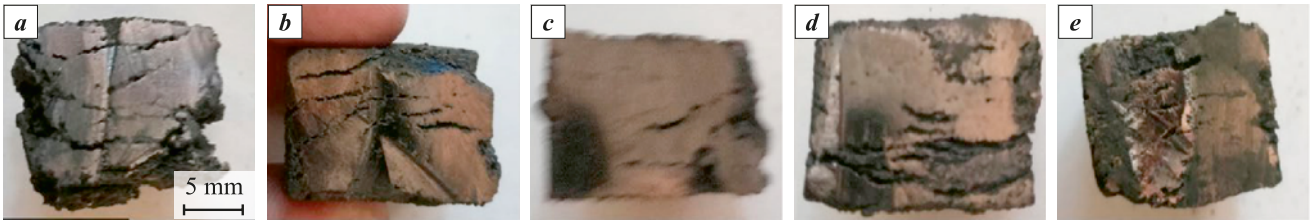

Fig. 5. Macro-images of polished sections of synthesized TiC–Cu cermet samples produced from the SHS charge with 15 % Cu addition at different compaction pressures
P, MPa: 22 (***a***), 34 (***b***), 45 (***c***), 56 (***d***), 69 (***e***)

Рис. 5. Фотографии шлифов синтезированных образцов керметов TiC–Cu из СВС-шихты с 15 %-ной добавкой меди при различных давлениях ее прессования
P, МПа: 22 (***a***), 34 (***b***), 45 (***c***), 56 (***d***), 69 (***e***)

Fig. 6. These data show that at $P = 45$ MPa all samples demonstrate a distinct mass maximum, indicating the most complete infiltration, particularly for SHS charges containing 5 and 10 % Cu.

To evaluate the completeness of infiltration, the density of the synthesized cermets was calculated as

$$\rho = m/V,$$

where m is the mass and V is the volume of the body. The obtained results are presented in Table 2 and in graphical form in Fig. 7. The data show that the den-

Table 1. **Dependence of cermet sample mass (g) on synthesis conditions**

Таблица 1. **Зависимость массы (г) образцов кермета от условий синтеза**

Cu addition, wt. %	Compaction pressure, MPa				
	22	34	45	56	69
0	15.6	18.2	26.4	21.6	22.7
5	27.4	30.65	31.7	30.9	27.4
10	22.0	29.2	31.6	27.6	27.9
15	26.8	31.0	28.5	31.3	28.4

Table 2. **Density (ρ, g/cm^3) of the synthesized cermet samples as a function of Cu addition to the SHS charge and compaction pressure**

Таблица 2. **Плотность полученных образцов керметов (ρ, г/см^3) в зависимости от условий синтеза – добавки меди в СВС-шихту и давления прессования**

Cu addition, wt. %	Compaction pressure, MPa				
	22	34	45	56	69
0	3.13	2.51	3.24	2.65	0
5	3.78	3.38	3.89	3.79	3.78
10	3.47	3.90	5.07	3.59	3.62
15	3.48	3.61	3.70	4.61	5.01

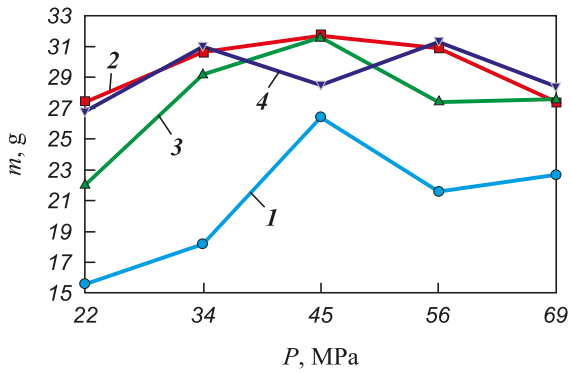

Fig. 6. Dependence of the mass of synthesized TiC–Cu cermet samples on the compaction pressure of the SHS charge with different Cu additions
1 – 0, ***2*** – 5 %, ***3*** – 10 %, ***4*** – 15 %

Рис. 6. Зависимость массы синтезированных образцов керметов от давления прессования СВС-шихты с различным количеством добавки меди
1 – 0, ***2*** – 5 %, ***3*** – 10 %, ***4*** – 15 %

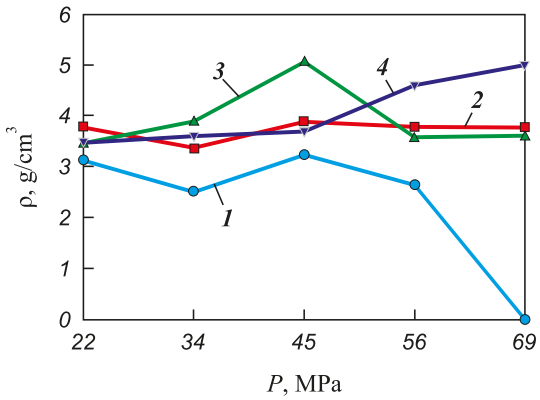

Fig. 7. Dependence of the density of synthesized TiC–Cu cermet samples on the compaction pressure of the SHS charge with different Cu additions
1 – 0, ***2*** – 5 %, ***3*** – 10 %, ***4*** – 15 %

Рис. 7. Зависимость плотности синтезированных образцов керметов TiC–Cu от давления прессования СВС-шихты с различным количеством добавки меди
1 – 0, ***2*** – 5 %, ***3*** – 10 %, ***4*** – 15 %

sity increases with increasing Cu content in the SHS charge. In addition, a distinct peak of maximum denity is observed at 45 MPa for the 10 % Cu addition.

To analyze the phase composition of the obtained TiC–Cu composites, *X*-ray diffraction (XRD) was performed. The corresponding diffraction patterns are shown in Figs. 8–10. All TiC–Cu samples produced from SHS charges without Cu addition contain a significant fraction of Ti–Cu intermetallic compounds, and all diffraction patterns exhibit shifts of Cu peaks, which may indicate stable incorporation of a small amount of Ti in the copper matrix (Fig. 8).

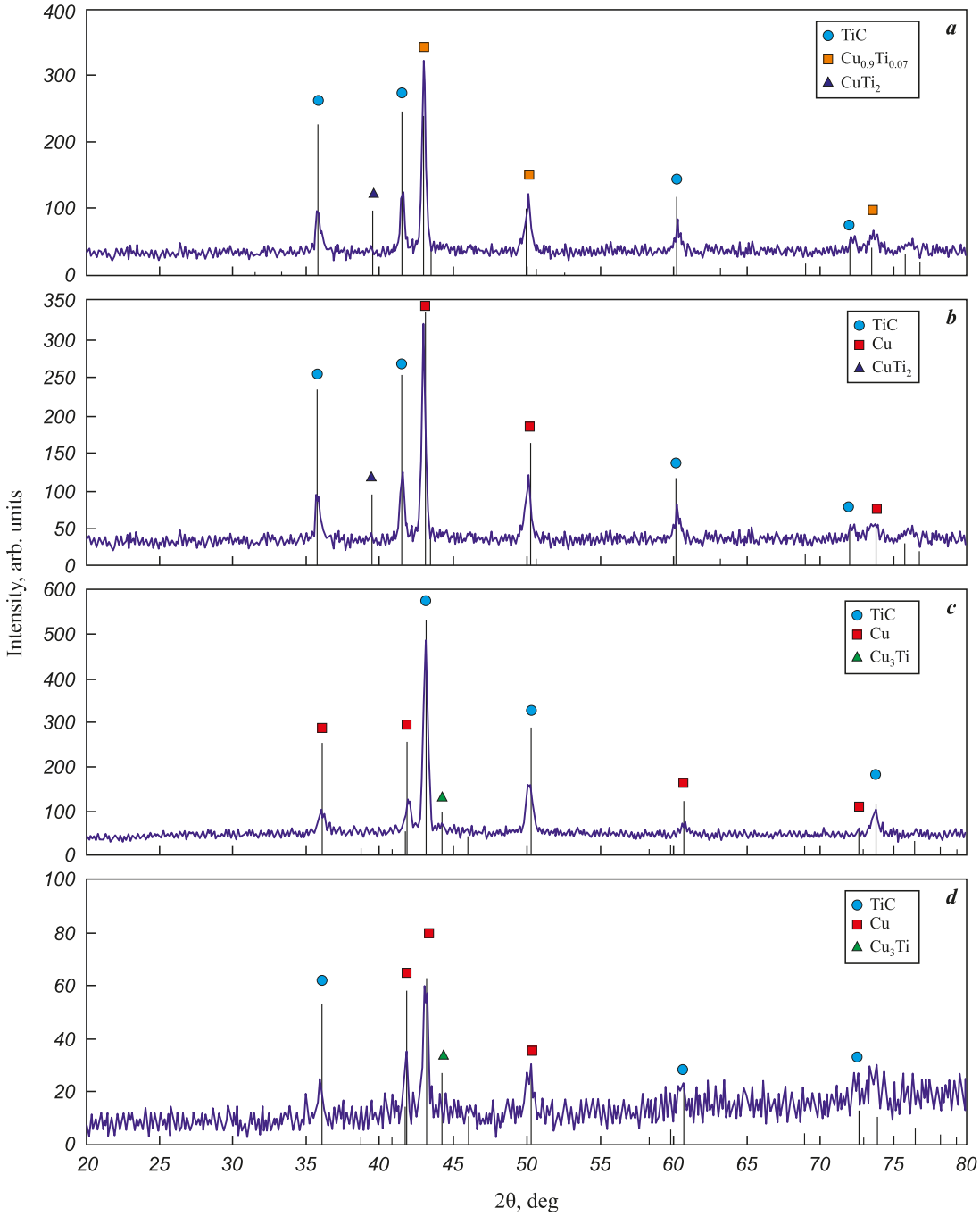

Fig. 8. Diffraction patterns of synthesized TiC–Cu cermet samples obtained from the SHS charge without Cu addition at different compaction pressures

P, MPa: 22 (***a***), 34 (***b***), 45 (***c***), 56 (***d***)

Рис. 8. Дифрактограммы синтезированных образцов керметов TiC–Cu из СВС-шихты без добавки меди при различных давлениях ее прессования

P, МПа: 22 (***a***), 34 (***b***), 45 (***c***), 56 (***d***)

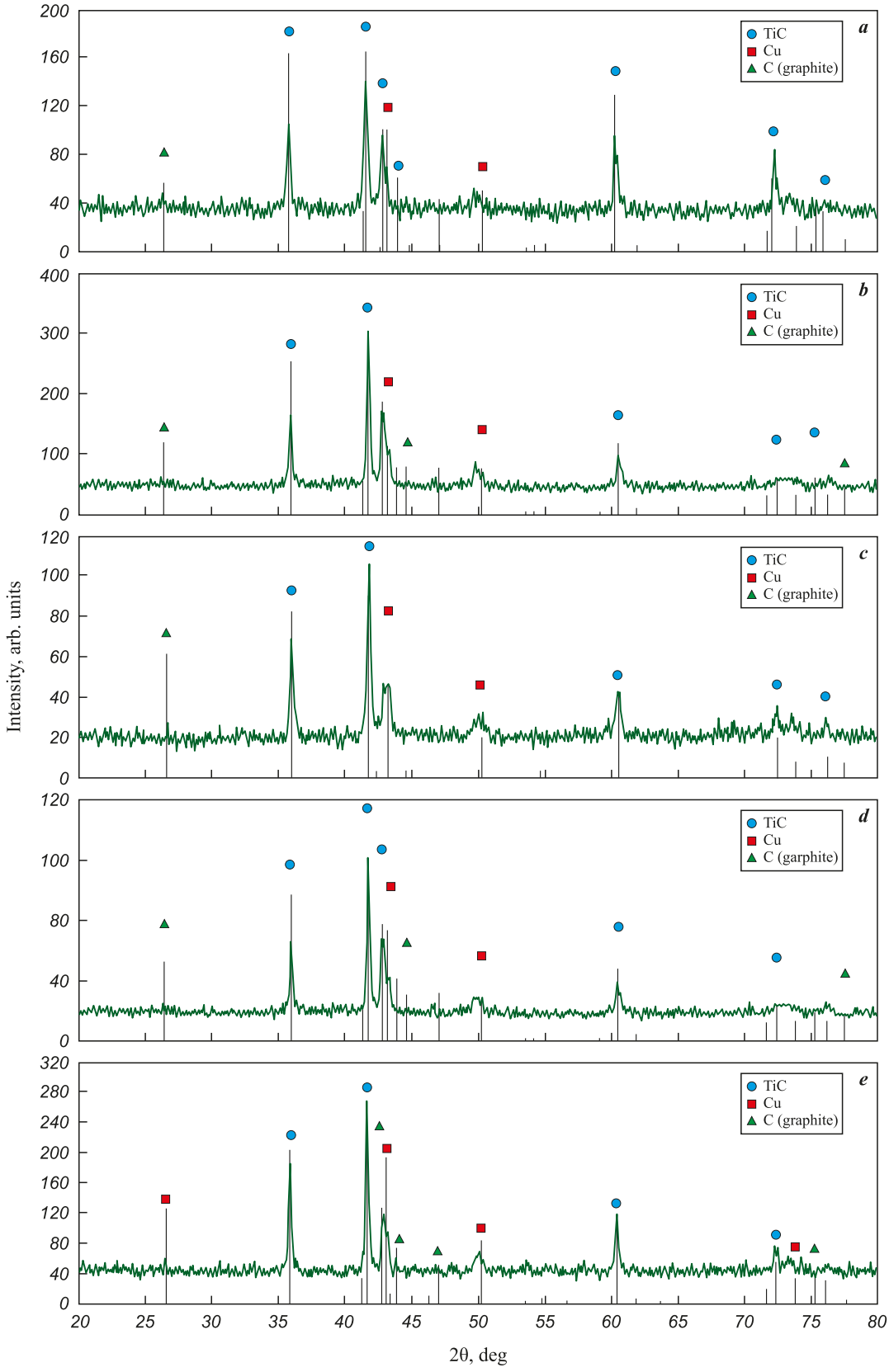

Fig. 9. Diffraction patterns of synthesized cermet samples obtained from the SHS charge with 5 % Cu addition at different compaction pressures

P, MPa: 22 (***a***), 34 (***b***), 45 (***c***), 56 (***d***), 69 (***e***)

Рис. 9. Дифрактограммы синтезированных образцов керметов с 5 %-ной добавкой меди

P, МПа: 22 (***a***), 34 (***b***), 45 (***c***), 56 (***d***), 69 (***e***)

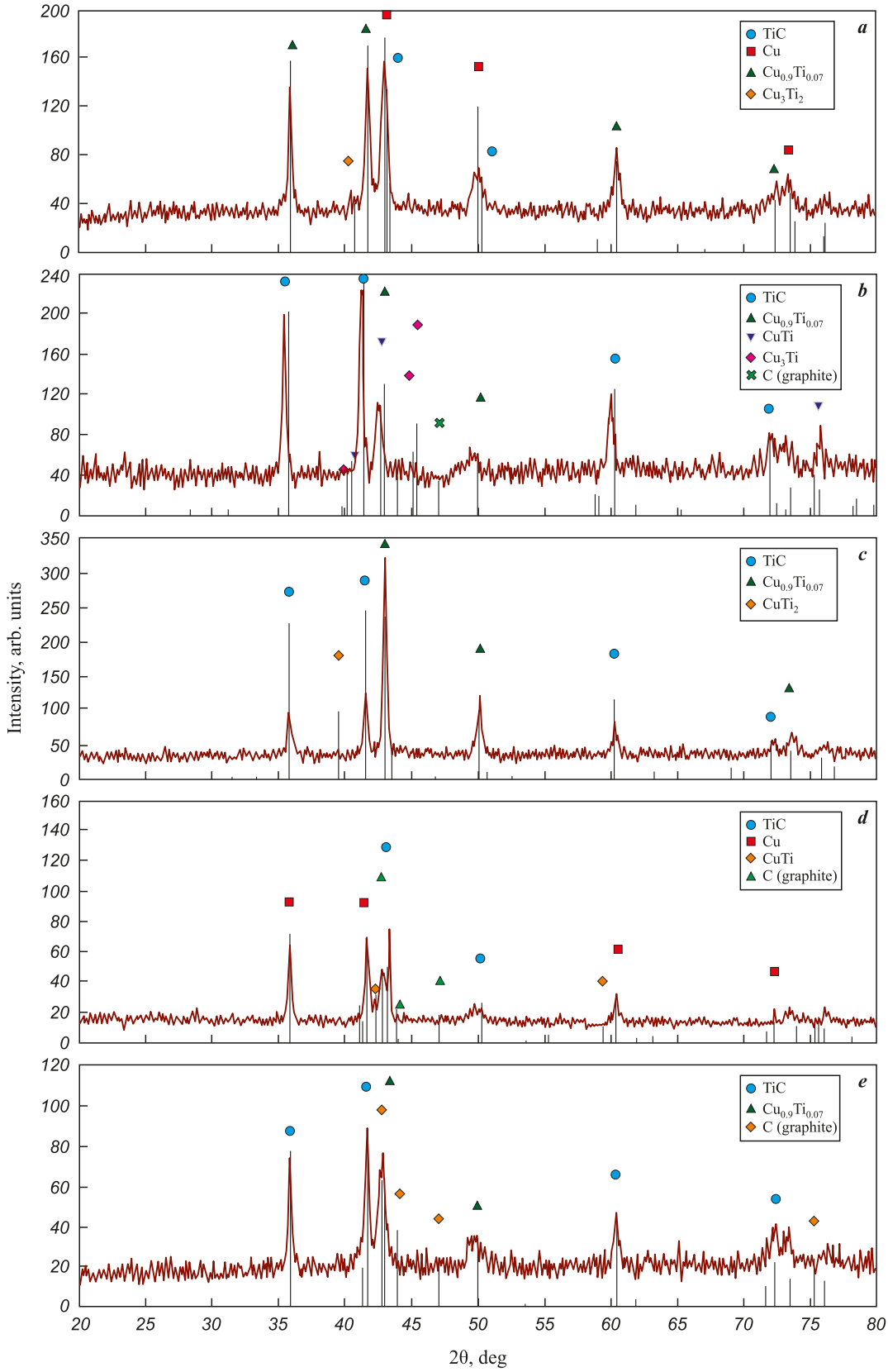

Fig. 10. Diffraction patterns of synthesized cermet samples obtained from the SHS charge with 10 % Cu addition at different compaction pressures

P, MPa: 22 (***a***), 34 (***b***), 45 (***c***), 56 (***d***), 69 (***e***)

Рис. 10. Дифрактограммы синтезированных образцов керметов с 10 %-ной добавкой меди

P, МПа: 22 (***a***), 34 (***b***), 45 (***c***), 56 (***d***), 69 (***e***)

Table 3. **Brinell hardness (HB) of the synthesized TiC–Cu cermet samples**

Таблица 3. **Твердость по Бринеллю (HB) полученных образцов керметов**

Cu addition, wt. %	Compaction pressure, MPa				
	22	34	45	56	69
0	90.00 ± 12.5	78.75 ± 4.3	22.00 ± 8.6	53.00 ± 9.0	0
5	68.50 ± 16.4	**95.75 ± 13.9**	75.25 ± 20.9	81.50 ± 15.4	45.25 ± 22.5
10	81.25 ± 12.1	**95.00 ± 7.4**	31.75 ± 11.0	50.00 ± 19.0	33.00 ± 7.2
15	71.75 ± 6.5	52.00 ± 4.3	88.50 ± 5.1	65.00 ± 25.5	56.25 ± 25.2

As follows from Fig. 9, the introduction of 5 % Cu into the charge eliminates the Ti–Cu intermetallic peaks on the diffraction patterns. However, peaks of free graphite (Gr) appear. Considering that the carbon phase (carbon black) in the initial SHS charge corresponded to the stoichiometry of TiC, the observed free carbon in the form of graphite should lead to non-stoichiometric titanium carbide TiC_x. The shift of the TiC peaks supports this interpretation. The graphite peak may also indicate graphitization of the amorphous carbon black introduced into the reaction mixture. Partial graphitization of carbon black during SHS of titanium carbide was previously reported in SHS–pressing experiments [29], where amorphous carbon transformed into graphitic nanofilms.

It is also important to note that under the conditions of intensive thermite combustion in air without the use of a special crucible for the metallothermic reaction (Fig. 1), where gravitational phase separation of liquid copper and alumina might not proceed to completion, the presence of Al_2O_3 in the TiC–Cu cermets was expected. However, XRD data show that none of the synthesized cermet samples contain alumina contamination. This result can be explained by the fact that at high combustion temperatures the relatively low-viscosity thermite copper melt wets the ceramic TiC preform and infiltrates it, whereas the more viscous Al_2O_3 melt does not wet the preform sufficiently and therefore does not infiltrate [30]. Thus, in this case the phase separation of Cu and Al_2O_3 produced in the thermite reaction is governed by their strong differences in viscosity and wettability of the TiC preform.

As seen from Fig. 10, with increasing Cu content in the charge, the SHS process is still initiated despite the expected reduction in exothermicity, leading to TiC formation. At the same time, Ti–Cu intermetallic compounds are generated, accompanied by partial graphitization of the carbon black.

XRD results for samples with 15 % Cu addition are not shown because they are identical to those presented in Fig. 10.

Based on these observations, it can be concluded that in all examined cases the molten copper completely infiltrates the porous SHS-produced TiC preform. In every experiment, stable combustion of the SHS charge and the formation of the TiC preform were observed. The purest samples – those free of intermetallic inclusions – were obtained with 5 % Cu addition to the Ti + C SHS charge at a compaction pressure of 45 MPa.

To investigate hardness (HB), a TH600 hardness tester (Time Group Inc., China) was used. The results, based on four measurements for each sample, are presented in Table 3. The highest hardness values (95 HB) were achieved at 5 and 10 % Cu additions with a compaction pressure of 34 MPa, whereas at the optimal pressure of 45 MPa and 15 % Cu addition a comparable value of 88.5 HB was reached.

For compression strength (σ_c), samples synthesized under optimal conditions (P = 45 MPa) were selected. Samples produced without Cu addition were excluded because of high residual porosity and structural heterogeneity, which significantly reduce strength compared to samples derived from Cu-containing charges. The obtained results are summarized in Table 4.

The data clearly show a substantial increase in compressive strength with increasing Cu content in the composite. This is associated with the fact that adding 5–15 % Cu to the Ti + C SHS charge promotes the formation of a more homogeneous SHS-produced TiC preform and ensures more complete infiltration by the thermite copper melt. As a result, structurally more uniform TiC–Cu composites with minimal residual porosity and significantly higher hardness and compressive strength are obtained.

Table 4. **Compressive strength (σ_c, MPa) of TiC–Cu cermet samples synthesized from SHS charges with and without Cu addition**

Таблица 4. **Значения прочности при испытании на сжатие ($\sigma_в$, МПа) образцов керметов из СВС-шихты с добавкой меди**

Cu, wt. %	0 %	5 %	10 %	15 %
σ_c, MPa	161.5 ± 9	240 ± 38	264.5 ± 23	390 ± 24

Conclusions

1. The feasibility of synthesizing TiC–Cu composites by combining aluminothermy to produce a copper melt with subsequent SHS initiation to form a porous TiC preform in air without the use of crucible reactors has been demonstrated.

2. It has been established that the copper melt generated by the aluminothermic reaction spontaneously infiltrates the still-hot porous SHS-produced TiC preform, in contrast to alumina, which is also formed during aluminothermy but does not infiltrate and remains outside the TiC preform.

3. Microstructural examination of the TiC–Cu composites showed that the compaction pressure of the Ti + C SHS charge and the addition of copper powder significantly affect the completeness of infiltration by the thermite copper melt. The highest infiltration completeness and density of the TiC–Cu samples (3.89 g/cm^3), combined with minimal structural defects, are achieved at 10 wt. % Cu addition to the SHS charge and a compaction pressure of 45 MPa.

4. The hardness of TiC–Cu composites obtained from SHS charges compacted at 45 MPa reaches 88.5 HB for a 15 wt. % Cu addition, which is close to the maximum value of 95 HB observed at P = 34 MPa with 5–10 wt. % Cu.

5. The compressive strength increases markedly with increasing copper content in the initial SHS charge and reaches a maximum value of 414 MPa at 15 wt. % Cu and P = 45 MPa.

References / Список литературы

1. Kumar V., Singh A., Ankit, Gaurav G. A comprehensive review of processing techniques, reinforcement effects, and performance characteristics in copper-based metal matrix composites. *Interactions*. 2024;245(1):357. https://doi.org/10.1007/s10751-024-02200-9
2. Serpova V.M., Nyafkin A.N., Kurbatkina E.I. Hybrid metal composite materials based on copper (review). *Trudy VIAM*. 2022;1(107):76–87. (In Russ.). https://doi.org/10.18577/2307-6046-2022-0-1-76-87

   Серпова В.М., Няфкин А.Н., Курбаткина Е.И. Гибридные металлические композиционные материалы на основе меди (обзор). *Труды ВИАМ*. 2022;1(107):76–87. https://doi.org/10.18577/2307-6046-2022-0-1-76-87
3. Suman P., Bannaravuri P.K., Baburao G., Kandavalli S.R., Alam S., Shanthi Raju M., Pulisheru K.S. Integrity on properties of Cu-based composites with the addition of reinforcement: A review. *Materials Today: Proceedings*. 2021;47(19):6609–6613. https://doi.org/10.1016/j.matpr.2021.05.096
4. Kumar S., Yadav A., Patel V., Nahak B., Kumar A. Mechanical behaviour of SiC particulate reinforced Cu alloy based metal matrix composite. *Materials Today: Proceedings*. 2021;41(2):186–190. https://doi.org/10.1016/j.matpr.2020.08.580
5. Chandrakanth R.G., Rajkumar K., Aravindan S. Fabrication of copper–TiC–graphite hybrid metal matrix composites through microwave processing. *International Journal of Advanced Manufacturing Technology*. 2010;48(5):645–653. https://doi.org/10.1007/s00170-009-2474-0
6. Tian J., Shobu K. Hot-pressed AlN-Cu metal matrix composites and their thermal properties. *Journal of Materials Science*. 2004;39(4):1309–1313. https://doi.org/10.1023/B:JMSC.0000013890.01343.0c
7. Shehata F., Fathy A., Abdelhameed M., Moustafa S.F. Preparation and properties of Al_2O_3 nanoparticle reinforced copper matrix composites by *in situ* processing. *Materials & Design*, 2009;30(7):2756–2762. https://doi.org/10.1016/j.matdes.2008.10.005
8. Dong S.J., Zhou Y., Shi Y.W., Chang B.H. Formation of a TiB_2-reinforced copper-based composite by mechanical alloying and hot pressing. *Metallurgical and Materials Transactions A*. 2002;33(4):1275–1280. https://doi.org/10.1007/s11661-002-0228-9
9. Samal P., Tarai H., Meher A., Surekha B., Vundavilli P.R. Effect of SiC and WC reinforcements on microstructural and mechanical characteristics of copper alloy-based metal matrix composites using stir casting route. *Applied Sciences*. 2023;13(3):1754. https://doi.org/10.3390/app13031754
10. Zhan Y., Zhang G. Friction and wear behavior of copper matrix composites reinforced with SiC and graphite particles. Tribology Letters. 2004;17(1):91–98. https://doi.org/10.1023/B:TRIL.0000017423.70725.1c
11. Zhang X., Shi C., Liu E. In-situ space-confined synthesis of well-dispersed three-dimensional graphene/carbon nanotube hybrid reinforced copper nanocomposites with balanced strength and ductility. *Composites. Part A: Applied Science and Manufacturing*. 2017;103:178–187. https://doi.org/10.1016/j.compositesa.2017.09.010
12. Kato H., Takama M., Iwai Y., Washida K., Sasaki Y. Wear and mechanical properties of sintered copper–tin composites containing graphite or molybdenum disulfide. *Wear*. 2003;255(1):573–578. https://doi.org/10.1016/S0043-1648(03)00072-3
13. Li L., Wong Y.S., Fuh J.Y., Lu L. Effect of TiC in copper–tungsten electrodes on EDM performance. *Journal of Materials Processing Technology*. 2001;113(1):563–567. https://doi.org/10.1016/S0924-0136(01)00622-7
14. Zarrinfar N., Kennedy A.R., Shipway P.H. Reaction synthesis of Cu–TiC_x master-alloys for the production of copper-based composites. *Scripta Materialia*. 2004;50(7):949–952. https://doi.org/10.1016/j.scriptamat.2004.01.007
15. Frage N., Froumin N., Dariel M.P. Wetting of TiC by non-reactive liquid metals. *Acta Materialia*. 2002;50(2):237–245. https://doi.org/10.1016/S1359-6454(01)00349-4
16. Froumin N., Frage N., Polak M., Dariel M.P. Wetting phenomena in the TiC/(Cu–Al) system. *Acta Materialia*. 2000;48(7):1435–1441. https://doi.org/10.1016/S1359-6454(99)00452-8

17. Amosov A.P., Borovinskaya I.P., Merzhanov A.G. Powder technology of self-propagating high-temperature synthesis of materials. Moscow: Mashinostroenie-1, 2007. 567 p. (In Russ.).

Амосов А.П., Боровинская И.П., Мержанов А.Г. Порошковая технология самораспространяющегося высокотемпературного синтеза материалов. М.: Машиностроение-1, 2007. 567 с.

18. Alabushev V.A., Rozhkov A.S. Method of obtaining products from composite materials based on titanium carbide: Patent 1338209 (RF). 1995.

Алабушев В.А., Рожков А.С. Способ получения изделий из композиционных материалов на основе карбида титана: Пат. 1338209 (РФ). 1995.

19. Tsikarev V.G., Filippenkov A.A., Filippov M.A., Alabushev A.V., Sharapova V.A. The experience of obtaining composite materials of the Ti–Cu–C system by the SHS process. *Powder Metallurgy and Functional Coatings*. 2021;(4):4–11. (In Russ.).
https://doi.org/10.17073/1997-308X-2021-4-11

Цикарев В.Г., Филиппенков А.А., Филиппов М.А., Алабушев А.В., Шарапова В.А. Опыт получения композиционных материалов системы Ti–Cu–C СВС-процессом. *Известия вузов. Порошковая металлургия и функциональные покрытия*. 2021;15(4):4–11.
https://doi.org/10.17073/1997-308X-2021-4-11

20. Amosov A., Amosov E., Latukhin E., Kichaev P., Umerov E. Producing TiC–Al cermet by combustion synthesis of TiC porous skeleton with spontaneous infiltration by aluminum melt. In: *Proc. of 2020 7th International Congress on Energy Fluxes and Radiation Effects*. IEEE, 2020. P. 1057–1062.
https://doi.org/10.1109/EFRE47760.2020.9241903

21. Amosov A.P., Latukhin E.I., Umerov E.R. Applying infiltration processes and self-propagating high-temperature synthesis for manufacturing cermets: A review. *Russian Journal of Non-Ferrous Metals*. 2022; 63(1):81–100.
https://doi.org/10.3103/S1067821222010047

Амосов А.П., Латухин Е.И., Умеров Э.Р. Применение процессов инфильтрации и самораспространяющегося высокотемпературного синтеза для получения керметов. Обзор. *Известия вузов. Цветная металлургия*. 2021;27(6):52–75.
https://doi.org/10.17073/0021-3438-2021-6-52-75

22. Umerov E., Amosov A., Latukhin E., Kiran K.U., Choi H., Saha S., Roy S. fabrication of MAX-phase composites by novel combustion synthesis and spontaneous metal melt infiltration: Structure and tribological behaviors. *Advanced Engineering Materials*. 2024;26(8):2301792.
https://doi.org/10.1002/adem.202301792

23. Karakich E.A., Samboruk A.R., Maidan D.A. Thermite welding. *Sovremennye materialy, tekhnika i tekhnologii*. 2021;1(34):63–67. (In Russ.).

Каракич Е.А., Самборук А.Р., Майдан Д.А. Термитная сварка. *Современные материалы, техника и технологии*. 2021;1(34):63–67.

24. Merzhanov A.G. Thermally coupled processes of self-propagating high-temperature synthesis. *Doklady Physical Chemistry*. 2010;434(2):159–162.
https://doi.org/10.1134/S0012501610100015

Мержанов А.Г. Развитие научных основ структурной макрокинетики процессов горения. *Доклады Академии Наук*. 2010;434(4):489–492.

25. Kharatyan S.L., Merzhanov A.G. Coupled SHS reactions as a useful tool for synthesis of materials: An overview. *International Journal of Self-Propagating High-Temperature Synthesis*. 2012;21(1):59–73.
https://doi.org/10.3103/S1061386212010074

26. Amosov A.P., Samboruk A.R., Yatsenko I.V., Yatsenko V.V. TiC–Fe powders by coupled SHS reactions: An overview. *International Journal of Self-Propagating High-Temperature Synthesis*. 2019;28(1):10–17.
https://doi.org/10.3103/S1061386219010023

27. Karakich E.A., Amosov A.P. Designing equipment for SHS thermite synthesis. *Sovremennye materialy, tekhnika i tekhnologii*. 2024;1(52):9–15. (In Russ.).

Каракич Е.А., Амосов А.П. Конструирование оснастки для СВС-термитного синтеза. *Современные материалы, техника и технологии*. 2024;1(52):9–15.

28. Karakich E.A., Latukhin E.I., Umerov E.R., Amosov A.P. Comparison of *X*-ray diffraction data of samples of TiC–Cu cermets synthesized under various charge pressing conditions. In: *Modern perspective development of science, equipment and technologies. Collection of scientific articles of the 2nd International Scientific and Technical Conference*. Kursk: CJSC "University Book", 2024. P. 175–179.

Каракич Е.А., Латухин Е.И., Умеров Э.Р., Амосов А.П. Сравнение данных РФА образцов керметов системы TiC–Cu, синтезированных при различных условиях прессования шихт. В сб.: *Современное перспективное развитие науки, техники и технологий. Материалы 2-й Междунар. науч.-техн. конференции*. Курск: ЗАО «Университетская книга», 2024. С. 175–179.

29. Shcherbakov V.A., Grydunov A.N., Karpov A.V., Sachkova N.V., Sychev A.E. Self-expanding high-temperature synthesis of TiC + *x*C composites. *Neorganicheskie materialy*. 2020;56(6):598–602. (In Russ.).
https://doi.org/10.31857/s0002337x20060111

Щербаков В.А., Грядунов А.Н., Карпов А.В., Сачкова Н.В., Сычев А.Е. Самораспространяющийся высокотемпературный синтез композитов TiC + *x*C. *Неорганические материалы*. 2020;56(6):598–602.
https://doi.org/10.31857/s0002337x20060111

30. Sanin V.N., Yukhvid V.I. Centrifugation-driven melt infiltration in high-temperature layered systems. *Inorganic Materials*. 2005;41(3):247–254.
https://doi.org/10.1007/s10789-005-0118-9

Санин В.Н., Юхвид В.И. Инфильтрация расплава под действием центробежной силы в высокотемпературных слоевых смесях. *Неорганические материалы*. 2005;41(3):305–313.

Information about the Authors

Egor A. Karakich – Post-graduate student, Junior Researcher of the Department of Metal Science, Powder Metallurgy, and Nanomaterials (MSPMN), Samara State Technical University (SamSTU)
ORCID: 0009-0006-8876-4321
E-mail: maximcaracki4@gmail.com

Emil R. Umerov – Cand. Sci. (Eng.), Leading Researcher of the Department of MSPMN, SamSTU
ORCID: 0000-0002-2050-6899
E-mail: umeroff2017@yandex.ru

Vladislav A. Novikov – Cand. Sci. (Eng.), Associate Professor of the Department of MSPMN, SamSTU
ORCID: 0000-0002-8052-305X
E-mail: vladislav_novyi@mail.ru

Evgeniy P. Kichaev – Cand. Sci. (Phys.-Math.), Associate Professor of the Department of Mechanics, SamSTU
ORCID: 0000-0003-0577-2889
E-mail: mech_kaf@samgtu.ru

Alexander P. Amosov – Dr. Sci. (Phys.-Math.), Head of the Department of MSPMN, SamSTU
ORCID: 0000-0002-1510-6567
E-mail: egundor@yandex.ru

Сведения об авторах

Егор Андреевич Каракич – аспирант, мл. науч. сотрудник кафедры «Металловедение, порошковая металлургия, наноматериалы» (МПМН), Самарский государственный технический университет (СамГТУ)
ORCID: 0009-0006-8876-4321
E-mail: maximcaracki4@gmail.com

Эмиль Ринатович Умеров – к.т.н, вед. науч. сотрудник кафедры МПМН, СамГТУ
ORCID: 0000-0002-2050-6899
E-mail: umeroff2017@yandex.ru

Владислав Александрович Новиков – к.т.н, доцент кафедры МПМН, СамГТУ
ORCID: 0000-0002-8052-305X
E-mail: vladislav_novyi@mail.ru

Евгений Петрович Кичаев – к.ф.-м.н, доцент кафедры «Механика», СамГТУ
ORCID: 0000-0003-0577-2889
E-mail: mech_kaf@samgtu.ru

Александр Петрович Амосов – д.ф.-м.н, профессор кафедры МПМН, СамГТУ
ORCID: 0000-0002-1510-6567
E-mail: egundor@yandex.ru

Contribution of the Authors

E. A. Karakich – carried out the combustion-mode synthesis experiments of TiC–Cu cermets, measured their density and hardness, prepared and processed the experimental results, and wrote the manuscript.
E. R. Umerov – formulated the research tasks, planned the experiments, analyzed and discussed the results, and contributed to manuscript preparation.
V. A. Novikov – performed SEM and XRD studies of the synthesized TiC–Cu cermets and participated in the analysis and discussion of the results.
P. E. Kichaev – conducted compressive strength tests of the synthesized TiC–Cu cermets and participated in the analysis and discussion of the results.
A. P. Amosov – defined the aim of the study, summarized the obtained results, and revised the manuscript.

Вклад авторов

Е. А. Каракич – проведение экспериментов по синтезу керметов TiC–Cu в режиме горения, определение их плотности и твердости, подготовка и оформление результатов экспериментов, написание статьи.
Э. Р. Умеров – постановка задач исследований, планирование экспериментов, анализ и обсуждение результатов, участие в написании статьи.
В. А. Новиков – проведение СЭМ и РФА синтезированных керметов TiC–Cu, участие в анализе и обсуждении результатов.

П. Е. Кичаев – проведение экспериментов по определению прочности при сжатии синтезированных керметов TiC–Cu, участие в анализе и обсуждении результатов.
А. П. Амосов – определение цели работы, обобщение полученных результатов, редактирование текста статьи.

Received 21.04.2025
Revised 12.05.2025
Accepted 19.05.2025

Статья поступила 21.04.2025 г.
Доработана 12.05.2025 г.
Принята к публикации 19.05.2025 г.

Nanostructured Materials and Functional Coatings
Наноструктурированные материалы и функциональные покрытия

UDC 620.193.2
https://doi.org/10.17073/1997-308X-2025-6-65-82

Research article
Научная статья

Mechanisms of failure in anti-corrosion polymer coatings on metallic surfaces of oilfield pipelines: Review

P. E. Yudin[1, 2], A. S. Lozhkomoev[3]

[1] **Samara State Technical University**
133 Molodogvardeyskaya Str., Samara 443001, Russia
[2] **Samara Research and Production Center LLC**
3B Garazhny Pr., Samara 443022, Russia
[3] **Institute of Strength Physics and Material Science, Siberian Branch of the Russian Academy of Sciences**
2/4 Akademicheskiy Prosp., Tomsk 634055, Russia

yudin@npcsamara.ru

Abstract. Corrosion is one of the primary causes of failure in oil and gas equipment, affecting not only its service life but also operational safety. In the Russian Federation, crude-oil production is increasingly complicated by the high water content of produced fluids, which significantly accelerates corrosion processes. The use of internal polymer coatings in pipelines partly mitigates this problem; however, the proportion of corrosion-related failures remains high. Effective protection of oil pipelines using polymer coatings requires a clear understanding of their degradation mechanisms, including under conditions that closely approximate field operation. Such understanding enables the development of effective solutions that help maintain the operating stock of oil wells in serviceable condition. This work summarizes the principal mechanisms of degradation of polymer coatings on metallic surfaces, including under exposure to aggressive environments. The key factors governing coating failure in oil pipelines are identified: diffusion and absorption of water molecules within the polymer matrix; disruption of molecular interactions in the polymer network; delamination due to loss of adhesion between the coating and the metal; interfacial corrosion; cathodic delamination; blister formation; and erosion-driven damage. The study presents results of the examination of various epoxy–novolac-based anticorrosion coatings removed from pipelines after field service and provides representative images of coatings at different degradation stages. The aim of the work was to consolidate current knowledge on the degradation mechanisms of polymer coatings on metals under diverse conditions and to refine the staged description of coating degradation in oil pipelines.

Keywords: internal anticorrosion coatings (IACCs), oil pipelines, production tubing, diffusion, degradation, delamination

Acknowledgements: This work was partially carried out within the framework of the State Assignment of the Institute of Strength Physics and Materials Science SB RAS, project FWRW-2022-0002.

For citation: Yudin P.E., Lozhkomoev A.S. Mechanisms of failure in anti-corrosion polymer coatings on metallic surfaces of oilfield pipelines: Review. *Powder Metallurgy and Functional Coatings*. 2025;19(6):65–82.
https://doi.org/10.17073/1997-308X-2025-6-65-82

Механизмы разрушения антикоррозионных полимерных покрытий на металлических поверхностях нефтепромысловых трубопроводов: обзор

П. Е. Юдин[1, 2], А. С. Ложкомоев[3]

[1] **Самарский государственный технический университет**
Россия, 443100, г. Самара, ул. Молодогвардейская, 244
[2] **ООО «НПЦ «Самара»**
Россия, 443022, г. Самара, Гаражный пр-д, 3б
[3] **Институт физики прочности и материаловедения СО РАН**
Россия, 634055, г. Томск, пр-т Академический, 2/4

yudin@npcsamara.ru

Аннотация. Коррозия является одной из главных причин выхода из строя нефтегазового оборудования. Помимо уменьшения его срока службы, она оказывает влияние на безопасность при его эксплуатации. В настоящее время добыча нефти в РФ осложнена обводненностью скважинной продукции, что в значительной степени интенсифицирует процессы коррозии. Применение внутренних полимерных покрытий трубопроводов частично решает данную проблему, однако доля отказов, связанных с коррозией, до сих пор остается на высоком уровне. Для эффективной протекторной защиты нефтепроводов с использованием полимерных покрытий необходимо понимание механизмов их разрушения, в том числе в приближенных к реальным условиях эксплуатации. Это позволит находить эффективные решения, способствующие поддержанию эксплуатационного фонда нефтяных скважин в работоспособном состоянии. В настоящей работе описаны основные механизмы разрушения полимерных покрытий на металлических поверхностях, в том числе при их эксплуатации в агрессивных средах. Выделены основные факторы, обуславливающие разрушение покрытий нефтепроводов: диффузия и абсорбция молекул воды внутри полимерной матрицы; нарушение связей внутри полимерной сети покрытия; отслоение покрытий из-за потери адгезии между ним и металлом; межфазная коррозия; катодное отслоение; образование пузырей; эрозионные процессы. Приведены результаты исследования различных антикоррозионных покрытий нефтепроводов на эпоксиноволачной основе после эксплуатации на месторождениях. Продемонстрированы изображения покрытий на различных этапах разрушения. Цель работы заключалась в обобщении механизмов разрушения полимерных покрытий на металлах в различных условиях и уточнении стадийности разрушения покрытий нефтепроводов.

Ключевые слова: коррозия, эрозия, полимерные покрытия, внутренние антикоррозионные покрытия (ВАКП), нефтепроводы, насосно-компрессорные трубы (НКТ), диффузия, деградация, расслоение

Благодарности: Работа частично выполнена в рамках государственного задания ИФПМ СО РАН, тема FWRW-2022-0002.

Для цитирования: Юдин П.Е., Ложкомоев А.С. Механизмы разрушения антикоррозионных полимерных покрытий на металлических поверхностях нефтепромысловых трубопроводов: обзор. *Известия вузов. Порошковая металлургия и функциональные покрытия*. 2025;19(6):65–82. https://doi.org/10.17073/1997-308X-2025-6-65-82

Introduction

All polymers are, in principle, permeable to well fluids encountered during oil production, and this permeability ultimately results in corrosion and delamination of internal polymer coatings (IPCs) used in oilfield pipelines [1]. The permeability of water, oxygen, and electrolyte ions through the coating is a fundamental characteristic governing the progression of coating degradation and the subsequent corrosion of pipeline steel [2]. The failure mechanism of IPCs includes:

• ingress of water and ions into the coating, where water diffuses through the polymer matrix and initiates changes in its properties;

• chemical degradation of the polymer molecular structure, in which water cleaves reactive sites within the epoxy network, causing hydrolysis-induced chain scission;

• accumulation of water within micropores of the coating, forming pathways for ion transport and ultimately leading to coating delamination from the metal surface [2].

Water absorption (hydration) within epoxy coatings is one of the primary causes of failure in pipeline coating systems [3].The uptake of water softens and plasticizes the polymer network, promotes blister formation, cracking, and localized delamination of the epoxy layer. During prolonged exposure to water and aggressive chemical species, water molecules displace polar interfacial bonds between the coating and steel, weakening adhesion. Underfilm corrosion represents the final stage of degradation, where the combined

effects of adhesion loss and osmotic pressure cause cracking and delamination, resulting in coating failure and a substantial reduction in pipeline service life [3].

The corrosion process is governed by anodic and cathodic reactions at the metal–polymer interface [4; 5]. Cathodic reactions at the metal surface generate hydroxide ions, producing a highly alkaline environment [6; 7] that can raise the local pH to values above 14 beneath the coating near the delamination front [7]. Cathodic delamination may therefore arise from:

– electrochemical reduction of the oxide layer [8];

– alkaline hydrolysis [9] or electrochemical degradation [10] of the interfacial polymer region responsible for adhesion;

– alkaline breakdown of interfacial bonds [8].

The interfacial polymer layer is also degraded by free radicals generated through Fenton-type reactions involving Fe^{2+} and H_2O_2 or organic peroxides [11; 12]. These peroxide intermediates form during oxygen reduction and react with iron cations in the electrolyte near the metal–polymer interface. Radical-driven degradation weakens interfacial adhesion and accelerates delamination [11; 12]. Cathodic polarization additionally promotes molecular hydrogen evolution at the metal surface [13; 14]. The evolution of molecular hydrogen gas at the metal–polymer interface can generate high interfacial pressures and additional mechanical stresses within the delamination zone. This effect is supported by the established correlation between the electrolytic hydrogen uptake current in the metal and the rate of cathodic delamination [13].

This review summarizes the general mechanisms of polymer-coating degradation on metallic surfaces in atmospheric environments or ionized water – where oxygen acts as the primary corrosive agent. It further examines the behavior of internal anti-corrosion coatings used in gathering pipelines, water lines, and tubing strings, and presents an updated staging model for IPC degradation in oil pipelines.

Cathodic delamination of coatings

A schematic representation of cathodic delamination is presented in [15] (Fig. 1), based on an experimental study of the degradation of a polybutadiene coating on steel exposed to a 0.5 M NaCl solution under a cathodic potential of –1.5 V for 1000 h [8]. At the edge of the delaminated region, a pronounced decrease in oxide-film thickness was observed compared with the central area [8]. The increase in pH at the delamination front promotes dissolution of the oxide layer; however, as the interfacial gap (the distance between the metal surface and the lifted coating) increases, the pH gradually decreases and the oxide layer thickensagain.

X-ray photoelectron spectroscopy (XPS) analysis [8] within the delaminated region revealed a metallic surface beneath the coating that was essentially free of oxide. According to the authors, this indicates that the surface oxide layer undergoes either reduction or dissolution. This process results in intraphase degradation of interfacial bonds and leads to interfacial separation along the metal/oxide boundary, with the oxide

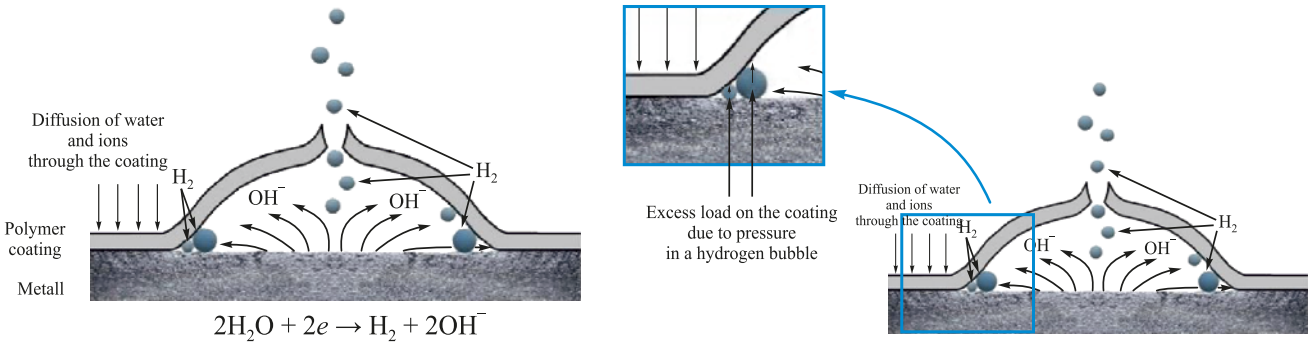

Fig. 1. Schematic representation of the processes occurring in a defective polymer coating and leading to cathodic delamination of the coating [15]

a – processes within the defect and beneath the delaminated coating; ***b*** – processes within the defect and beneath the delaminated coating, with detailed representation of the metal–polymer interface and the delamination zone

Рис. 1. Схема процессов, протекающих в дефектном полимерном покрытии и приводящих к катодному отслоению покрытия [15]

a – процессы в дефекте и под отслоившимся покрытием; ***b*** – процессы в дефекте и под отслоившимся покрытием с детализацией границы раздела металл–полимер и зоны отслоения покрытия

layer being removed together with the delaminated coating. Outside the interfacial separation zone, the coating detaches cleanly from the metal substrate without cohesive damage [8].

Anodic corrosion

Filiform corrosion, a form of anodic underfilm corrosion, has been observed on metals with polymer coatings exposed to a humid atmosphere, the aggressiveness of which is enhanced by artificial or natural contaminants such as sulfur dioxide or chlorides [16; 17]. This type of corrosion (Fig. 2) typically initiates at discontinuities in regions containing porosity and voids, mechanical defects, or areas of reduced coating thickness. Filiform corrosion is characterized by linear propagation paths, where local accumulation of water at the metal/coating interface triggers electrochemical processes [18; 19]. Localized anodic reactions on the steel are coupled with oxygen reduction, which in turn promotes cathodic degradation of adhesion at the interface.

Diffusion of reactants through polymer coatings

Fig. 3 illustrates the stages of coating delamination under high hydrostatic pressure as proposed in [20]. In an epoxy-varnish coating, the applied pressure significantly accelerates the diffusion of water toward the coating–substrate interface and leads to the formation of numerous small, water-filled blisters.

One of the most important degradation mechanisms is coating aging, which results in a loss of barrier performance and deterioration of mechanical properties. Aging occurs under the combined influence of elevated temperature, chemically aggressive species, pressure, and mechanical loading [21]. Another critical failure mechanism is blister formation during decompression. As described in [21], gases penetrate the pores of the material at high pressure; when the pressure is rapidly reduced, the dissolved gases expand, generating blisters within the coating and causing its failure (Fig. 4, *a*). Corrosion also develops at sites where the coating is mechanically damaged (Fig. 4, *b*). In such cases, the base metal of the pipe is directly exposed to the aggressive environment, leading to active corrosion. When defects are present, the rate of corrosion progresses with similar intensity regardless of the coating type [21].

The authors of [22] nvestigated the effect of prolonged exposure (85 weeks) to hot water at 65 °C on epoxy powder barrier coatings used to protect metallic surfaces, including components of oil and gas equipment. It was shown that degradation of the coating begins after only 8 weeks, while oxidation of the substrate becomes noticeable after 182 days. Adhesion-strength measurements demonstrated that the bonding strength of the coatings decreases rapidly due to water-induced plasticization, but subsequently exhibits a slight recovery attributed to secondary crosslinking of the epoxy network [22].

A study presented in [23] examined the degradation mechanisms of coatings based on amine-cured epoxy novolac (EN) and bisphenol-F (BPF) resins under

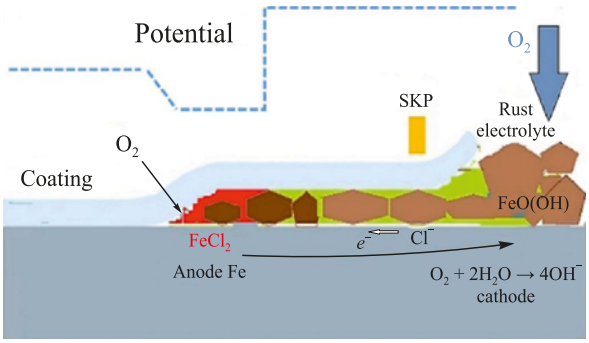

Fig. 2. Schematic representation of anodic delamination driven by corrosion, and the potential distribution along the metal–coating interface [16]

Рис. 2. Схема анодного отслоения покрытия под воздействием коррозии и распределение потенциала вдоль границы основы и покрытия [16]

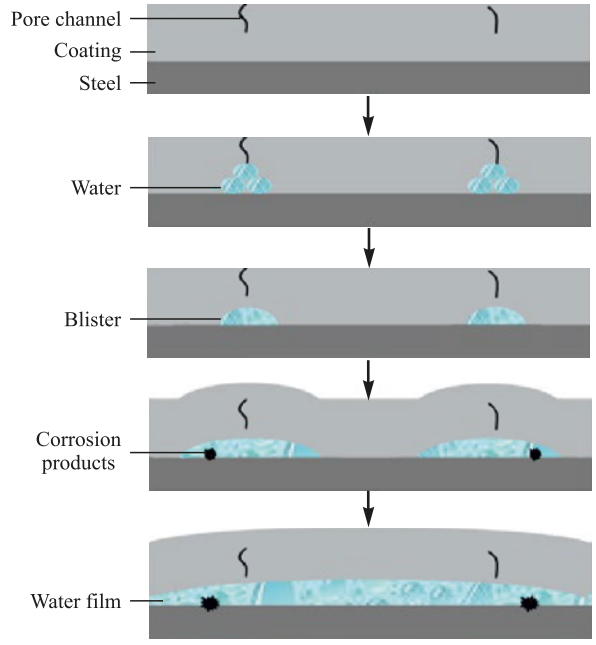

Fig. 3. Schematic representation of the coating-failure process under high hydrostatic pressure [20]

Рис. 3. Схематическое изображение процесса разрушения покрытий под высоким гидростатическим давлением [20]

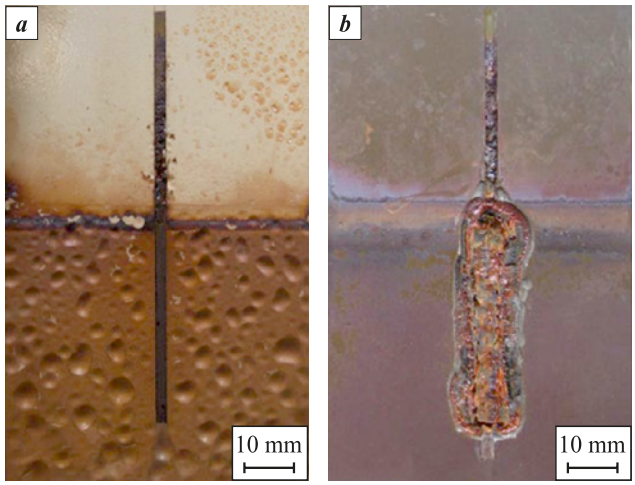

Fig. 4. Coating failure after corrosion autoclave testing [21]
a – blister formation caused by insufficient film thickness;
b – corrosion developing in a damaged coating

Рис. 4. Разрушение покрытия после коррозионных автоклавных испытаний [21]
a – образование пузырей из-за малой толщины пленки;
b – коррозия в поврежденном покрытии

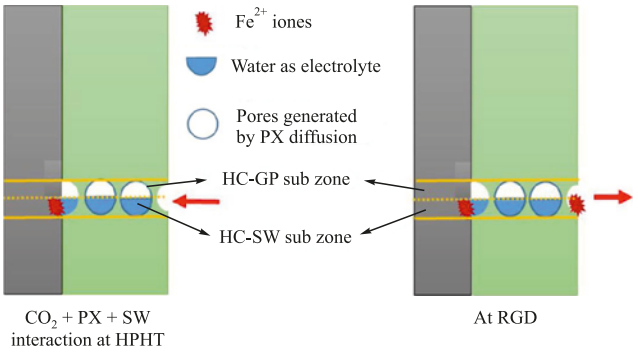

Fig. 5. Water ingress through the coating toward the metal and the migration route of iron ions toward the coating surface during decompression-driven pressure release [23]

Рис. 5. Проникновение воды через покрытие к металлу и путь ионов железа к поверхности покрытия при декомпрессионном сбросе давления [23]

high-pressure, high-temperature (HPHT) conditions. The coatings were subjected to autoclave testing. It was established that the degradation mechanisms of EN and BPF protective coatings under HPHT conditions are governed by the combined action of gas, hydrocarbon, and aqueous phases and their joint effects on the polymer structure and the substrate. In the gas phase, consisting of nitrogen and carbon dioxide, the coatings remain unchanged because no significant interaction or physical damage occurs. However, contact of the coating surface with hydrocarbons (*p*-xylene) results in solvent diffusion into the polymer matrix, which increases the free volume within the coating layer. Fig. 5 illustrates the mechanisms of coating degradation under HPHT exposure to *p*-xylene during autoclave conditioning, as well as during pressure release under decompression [23].

The study reported in [24], which involved simultaneous exposure to three phases (a gas phase, a hydrocarbon liquid phase, and mineralized water), investigated the influence of carbon dioxide (CO_2) present in the gas phase under HPHT conditions on the degradation of amine-cured epoxy novolac (EN) coatings. It was established that the combined action of the gas, hydrocarbon, and aqueous phases deteriorates the coating performance and leads to underfilm corrosion. When each phase was applied separately under low-pressure conditions, the EN network remained intact and essentially impermeable. However, in regions exposed to hydrocarbons, the joint action of *p*-xylene and CO_2 at elevated pressure and temperature causes a reduction in the glass-transition temperature, followed by softening of the EN network. This softening allows dissolved CO_2 to diffuse into the EN structure, forming microscopic voids at the coating surface (Fig. 6).

Comparative autoclave tests under high-pressure, high-temperature (HPHT) conditions were carried out in [25] or epoxy–siloxane hybrid coatings. These coatings were shown to outperform EN-based systems, which soften upon exposure to hydrocarbons (such as *p*-xylene), resulting in a reduction in glass-transition temperature and an accelerated diffusion of gases and ions.

The long polymer chains in siloxane-based coatings (EN-EPDMS) promote the uptake of water molecules, especially under high pressure. Such coatings tend to form unruptured blisters during rapid pressure release. In contrast, the coating modified with the short-chain 3-glycidyloxypropyltrimethoxysilane (EN-GPTMS) exhibited high resistance to decompression (Fig. 7).

Under the assumption that the coating remains intact and free of defects or inclusions, it can therefore be concluded that the primary initiating factor for coating degradation and the onset of corrosion is the diffusion of reactive species through the polymer layer (Fig. 8).

However, as noted by the authors of the review [26], many open questions remain regarding the swelling behavior of polymers and the complexity of describing diffusion processes that deviate from ideal Fickian diffusion (Fick's second law), among other issues (Fig. 9).

Overall, the degradation of a polymer coating is governed by the following processes and/or their combination.

• Diffusion and absorption of water molecules within the polymer matrix. These processes are influ-

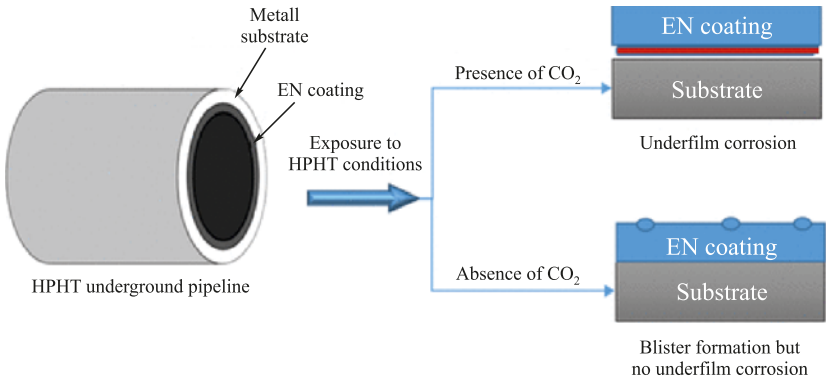

Fig. 6. Mechanisms by which the hydrocarbon and aqueous phases affect an epoxy–novolac coating under high-pressure, high-temperature conditions, in the presence and absence of carbon dioxide in the system [24]

Рис. 6. Механизмы воздействия углеводородной и водной фаз на эпоксидно-новолачное покрытие в условиях высоких давлений и температур при наличии углекислого газа в системе и без него [24]

enced by surface topography, polymer structure, and environmental conditions. Free volume and microcracks within the coating structure provide pathways for the diffusion of water molecules, which may follow Fickian, non-Fickian, and/or capillary diffusion regimes. As they move from the external coating surface toward the coating/metal interface, water molecules may either migrate freely or interact with polar segments of the polymer network. Water absorption by the polymer leads to structural instability of the polymer network (plasticization), promoting volumetric expansion, interfacial separation, and erosion of the coating [27–30].

• Disruption of van der Waals and hydrogen bonds within the polymer network as a result of interactions between water molecules and polar segments of the polymer chain, which causes anisotropic expansion of the network. These volumetric changes and the associated stresses can irreversibly alter the coating microstructure, leading to the initiation and/or growth of microcracks within the coating and at the coating/metal interface [31–34].

• Fragmentation of polymer chains due to hydrolytic degradation of coatings containing hydrolysable bonds. In addition to hydrolysis of the polymer matrix, dissolution of coating components (such as pigments and additives) may occur, resulting in mass loss and structural changes. The hydrolysis process can further accelerate polymer degradation by altering the local pH in regions surrounding the reactive sites [35–37].

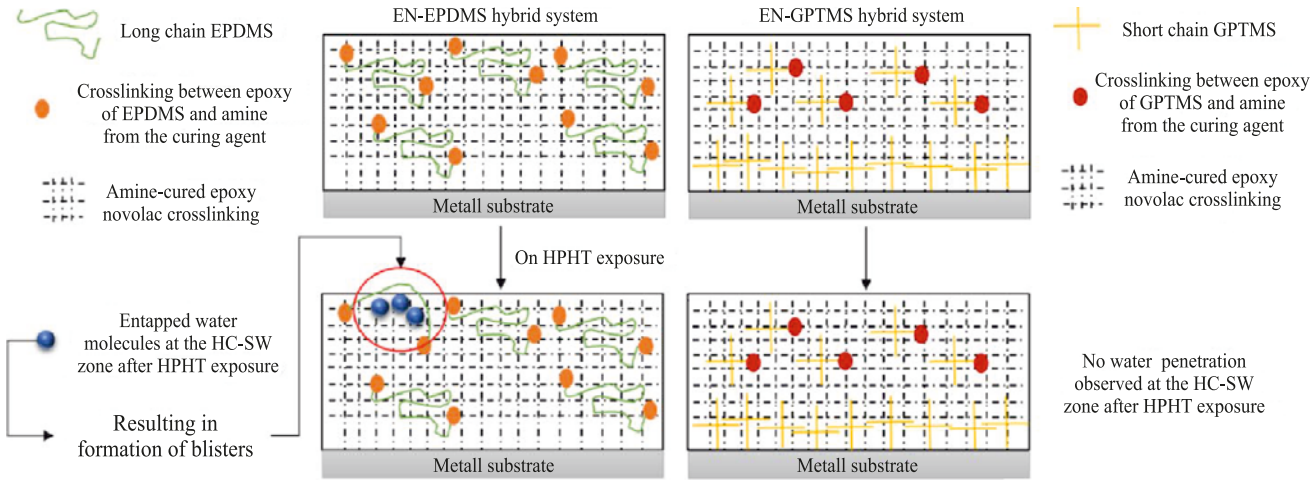

Fig. 7. Schematic illustration of crosslinking in EN-EPDMS and EN-GPTMS coatings before and after HPHT exposure [25]

The long and flexible EN-EPDMS chains exhibit trapped water molecules in the HC–SW region, which leads to the formation of unruptured blisters. By contrast, the short-chain, EN-GPTMS–crosslinked network shows no detectable changes under high-pressure, high-temperature exposure

Рис. 7. Схематическая иллюстрация сшивания EN-EPDMS и EN-GPTMS до и после воздействия HPHT [25]

Длинная и гибкая цепь EN-EPDMS демонстрирует захваченные молекулы воды в зоне HC–SW, что приводит к образованию нелопнувших пузырей. Напротив, короткая цепь в EN-GPTMS сшитой структуре не показывает никаких изменений при воздействии высоких давлений и температур

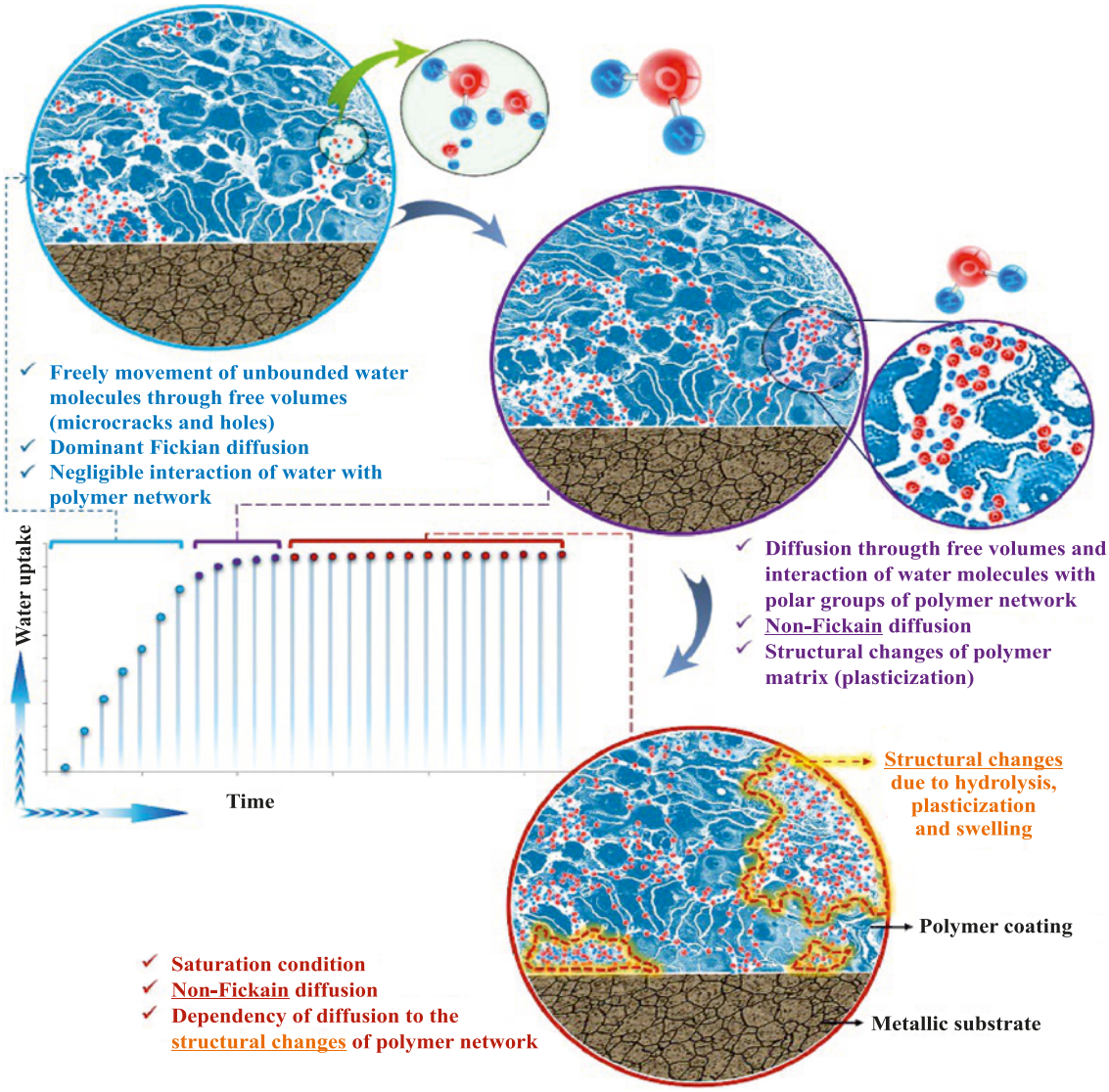

Fig. 8. Schematic illustration of changes in water uptake in polymer coatings as a function of exposure time [18]

Рис. 8. Схематическая иллюстрация изменения водопоглощения в полимерных покрытиях с течением времени [18]

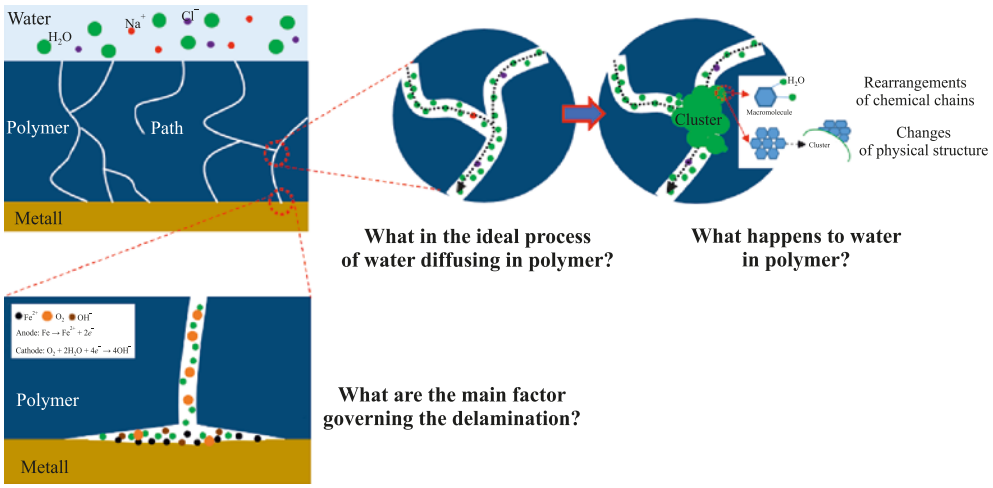

Fig. 9. Schematic representation of water diffusion through a polymer layer toward the metallic surface and the associated unresolved questions [26]

Рис. 9. Схема диффузии воды через слой полимера к металлической поверхности и связанные с этим вопросы [26]

• Delamination associated with loss of adhesion, driven by damage to molecular bonds between the coating and the metal, disruption of thermodynamic equilibrium at the metal–polymer interface, and the breakdown of mechanical interlocking and/or the development of osmotic pressure. Delamination is initiated by the permeation of water molecules through the coating to the metallic substrate, thereby compromising coating integrity and accelerating adhesion loss. Typically, delamination is preceded by plasticization and swelling of the coating, as well as changes in interfacial chemistry [38–41].

• Interfacial delamination caused by corrosion at the metal–coating interface. Variations in pH within the interfacial region disturb the thermodynamic equilibrium established by Lewis acid–base interactions, thereby reducing adhesion strength [18]. Corrosion at the metal/coating interface disrupts mechanical interlocking between the coating and the metallic substrate, further weakening adhesion. The accumulation of corrosion products in the interfacial gap generates mechanical stresses due to expansive forces (for example, the formation and growth of rust) [42]. Moreover, the hygroscopic nature of rust enhances moisture uptake, leading to dimensional changes and additional mechanical stresses within the coating. These stresses promote interfacial separation and cracking. Lateral expansion of the separated coating region, caused by growth of corrosion products, can also lead to blister formation [43].

• Cathodic delamination of polymer coatings, which is driven by the alkaline environment generated by cathodic reactions at the metal–polymer interface. As a result, the thermodynamic equilibrium at the interface is disrupted: alkaline species dissolve the thin oxide layer on the metal and induce chemical degradation of the polymer via alkaline hydrolysis and reactive intermediates. This process also promotes substrate corrosion by disturbing the local charge balance and facilitating the transport of charged species. Ultimately, these mechanisms undermine the adhesion forces between the coating and the substrate [39; 44–46].

• Blister-induced delamination of the coating arises from water uptake and electrochemical reactions. The accumulation of water and dissolved species at the metal–polymer interface, together with the resulting osmotic pressure and mechanical stresses, reduces the adhesion of the coating to the metallic substrate and leads to interfacial delamination [47–52].

Erosion–corrosion processes

The processes described above, whose combined action leads to degradation of the protective polymer coating, proceed at a substantially accelerated rate when the coating is additionally exposed to flowing fluid during service. In [53], a comparison was made between the deterioration of barrier properties under flow conditions and under static immersion, using an experimental setup whose schematic arrangement is shown in Fig. 10.

The barrier properties of the coating during testing were evaluated using electrochemical impedance spectroscopy (EIS). The EIS measurements showed that the impedance modulus of the coating decreases much more significantly under flow, indicating that fluid motion along the protective coating accelerates water ingress into the coating [53]. A similar conclusion – that degradation of an organic coating accelerates when immersed in two different working fluids (DI water and 3.5 wt. % NaCl solution) under laminar-

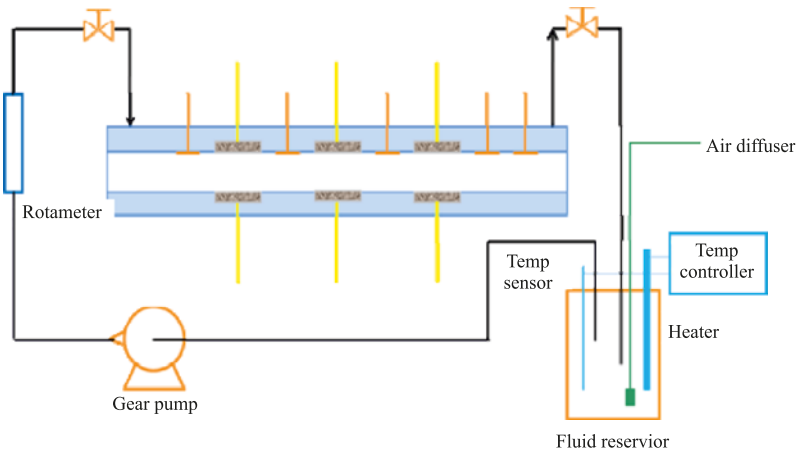

Fig. 10. Schematic diagram of the setup used to simulate fluid-flow effects on a polymer coating [53]

Рис. 10. Принципиальная схема установки, моделирующей условия воздействия потока жидкости на полимерное покрытие [53]

flow conditions compared with static immersion – was also reported by the authors of [54].

A review presented in [55] summarized existing research on tribocorrosion of coatings, i.e., their behavior under simultaneous action of erosive wear and corrosion. Under erosive flow, the authors distinguish three coating-damage mechanisms:

– surface damage, in which a defect in the passive film triggers repassivation and film reconstruction on the coating surface (Fig. 11, *a*):

– corrosive wear of hard coatings on metallic substrates, leading to the formation of pits and blistering of the protective coating, followed by mechanical damage and delamination (Fig. 11, *b*);

– abrasive action on the coating surface caused by the potential difference between the metallic substrate beneath the coating and entrained abrasive particles, which accelerates surface wear (Fig. 11, *c*).

In [56], the authors described the degradation mechanism of protective epoxy–novolac coatings exposed to erosion–corrosion. At the first stage, erosive attack produces microcracks exclusively around filler particles. These microcracks create a porous structure that allows the electrolyte to gradually penetrate deeper into the coating. At this stage, however, the coating still maintains sufficient barrier performance to prevent corrosion initiation.

At the second stage, the cracks begin to widen, and the barrier properties of the coating weaken under aggressive conditions (high temperature, low pH, presence of CO_2 and chlorides). The electrolyte penetrates further and reaches the metal–polymer interface. As a result, local corrosion initiates and produces corrosion products (iron oxides) within the pores of the coating. This decreases the coating resistance, as detected by electrochemical measurements.

At the third stage, the mechanical integrity of the coating is severely compromised. As underfilm corrosion continues to deepen and spread, the coating delaminates and its structure becomes increasingly porous. As a result, the access of aggressive species to the metallic substrate increases, leading to the initiation of new corrosion sites, and the coating ultimately loses its barrier functionality. All three stages of coating degradation are shown in Fig. 12.

Thus, the principal stages and regularities of polymer-coating degradation under high-pressure and high-temperature conditions, as well as under exposure to abrasive particles, have been examined. In most cases, the studies were conducted in atmospheric environments or in ionized water, where oxygen is the predominant corrosion-active species.

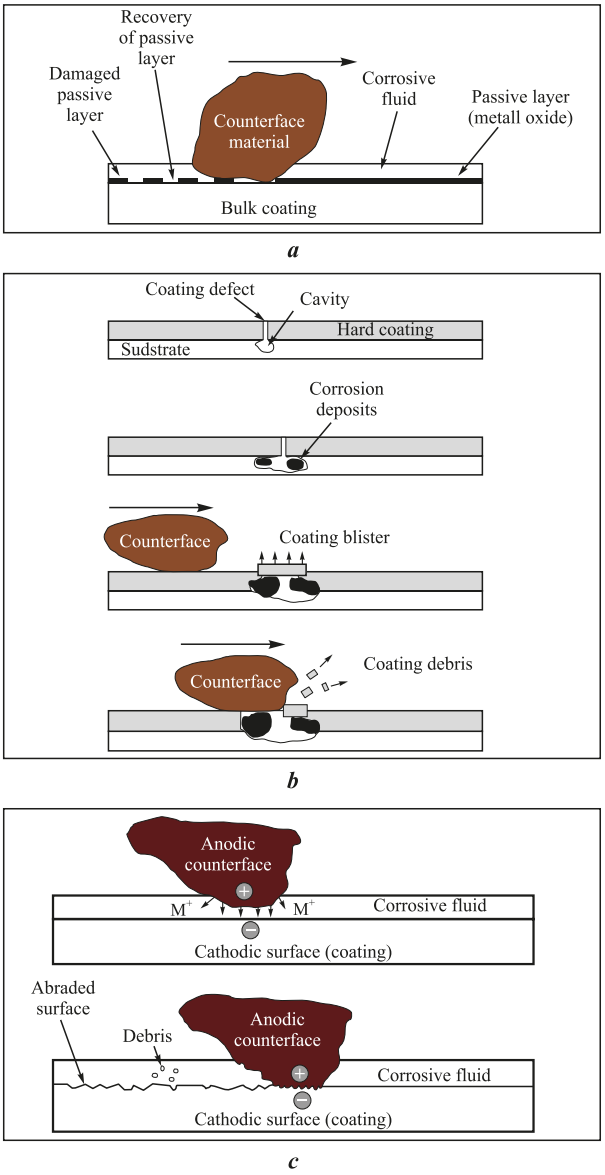

Fig. 11. Three coating–failure mechanisms under erosive conditions [55]

a – type-1 wear: corrosion of hard coatings on metallic substrates, in which damage to the passive film leads to its repassivation and regeneration on the coating surface;
b – corrosive wear of hard coatings on a metallic surface, resulting in pitting and blistering of the protective coating, followed by mechanical damage and delamination;
c – abrasive action on the coating surface caused by the potential difference between the metallic substrate beneath the coating and entrained abrasive particles, which activates surface wear of the coating

Рис. 11. Три механизма разрушения покрытия в условиях эрозионного воздействия [55]

a – износ 1-го типа: коррозия твердых покрытий на металлических подложках, при которой повреждение пассивной пленки приводит к повторной ее пассивации и регенерации на покрытии;
b – коррозионный износ твердых покрытий на металлической поверхности, приводящий к образованию питтингов и вздутию защитного покрытия и в результате – к его механическому разрушению и отслоению;
c – абразивное воздействие на поверхность покрытия, вызванное разнозаряженностью металлической подложки под покрытием и абразивными частицами, в результате чего происходит активация истирания поверхности покрытия

Degradation of internal anticorrosion coatings in oil pipelines

A review of degradation mechanisms of internal anticorrosion coatings (IACCs) used in oil-gathering collectors, water pipelines, and production tubing strings was previously carried out in [57]. All coatings examined were based on epoxy–novolac systems with different ratios of epoxy film-forming components to novolac resin. Powder coatings were applied by electrostatic spraying, whereas liquid coatings were applied using airless spraying followed by drying or polymerization.

Several processes occur simultaneously within the coating: diffusion of corrosion-active species, degradation of interfacial adhesion, and destructive changes within the polymer matrix that lead to a reduction of cohesive strength. The intensity of these processes depends strongly on temperature and increases sharply as the temperature approaches the glass-transition temperature (*Tg*) (taking into account its depression caused by water uptake). Therefore, the behavior of these coatings must be considered specifically in their glassy state [58].

At the present stage of research, coating degradation can be represented by the following sequence (Fig. 13). In the first stage, the polymer undergoes water uptake, accompanied by significant changes in its physical and mechanical properties: Tg decreases by approximately 30 °C at 1.5 wt. % water uptake, while tensile strength decreases by about 20 % [58]. This initial stage proceeds relatively rapidly and can be described by the diffusion equation [26]:

$$q(t) = 1 - \frac{8}{\pi^2}\sum_{n=0}^{\infty}\frac{1}{(2n+1)^2}\exp\left\{-\frac{(2n+1)^2\pi^2 D}{4l^2}t\right\},$$

where $q(t)$ is the average concentration of the penetrant across the polymer layer at time t, s; D is the diffusion coefficient for a constant source into a polymer layer of thickness l, cm^2/s.

The values of D lie in the range of $1.0\cdot10^{-9}$ to $5.0\cdot10^{-8}$ cm^2/s and depend on the chemical composition of the film-forming component and curing agent, the degree of crosslinking, the type and loading of fillers, as well as the pressure and temperature of the environment.

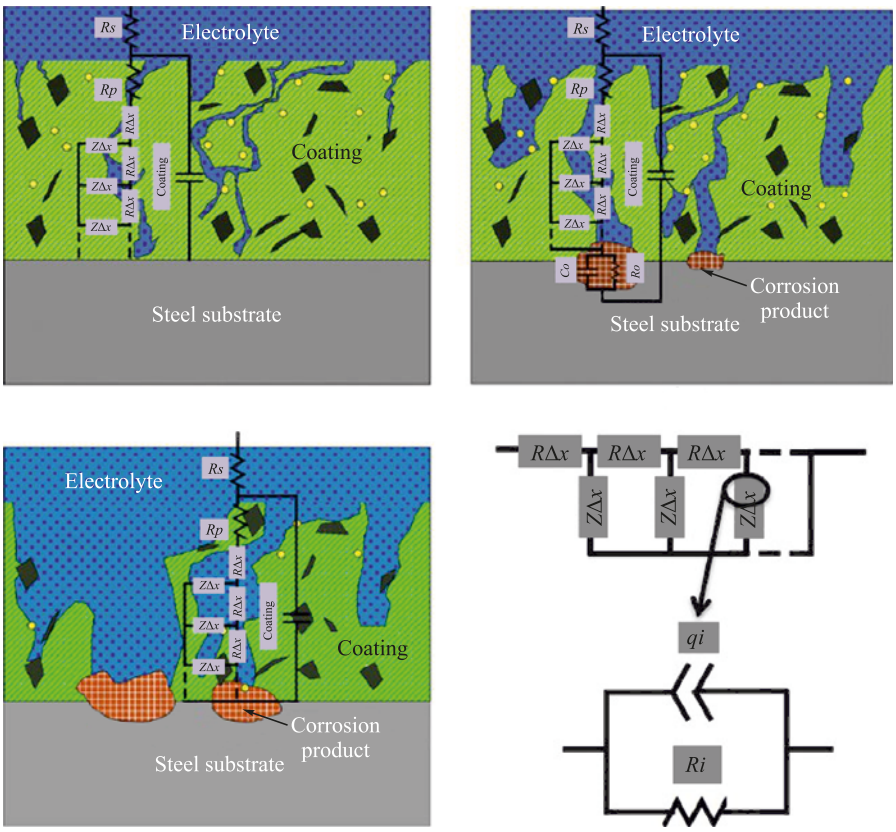

Fig. 12. Stages of polymer-coating degradation under erosive wear, together with the corresponding EIS equivalent circuits for each stage [56]

Рис. 12. Стадии разрушения полимерного покрытия в результате эрозионного износа, а также эквивалентные схемы EIS, соответствующие этим стадиям [56]

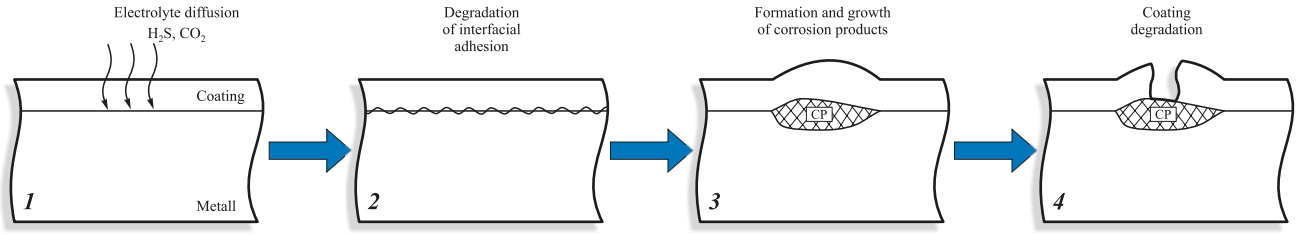

Fig. 13. Staged degradation process of internal protective coatings

Рис. 13. Стадийность процесса разрушения внутренних защитных покрытий

At the second stage, the coating undergoes degradation of interfacial adhesion, which is typically localized and appears as spots with a diameter of approximately ten coating-thicknesses (Fig. 14). This process is prolonged when the coating operates at temperatures below the wet glass-transition temperature (wet *Tg*) of the polymer and when no application defects are present. The key durability criteria include the initial adhesion strength, the diffusion coefficient, and the coating's resistance to chemical and physical degradation under service conditions – i.e., the retention of intrinsic coating properties that determine its barrier performance. For example, destructive changes in the polymer structure may produce microcracks that enable not only electrolyte diffusion but full mass transport through the coating.

During failure analysis of internal polymer coatings, it is often found that a significant reduction in service life results from violations introduced either during application or during operation. A common example illustrating how application technology influences the durability of internal coatings is the frequent occurrence of defects at the ends of production tubing. The application of coatings to tubing ends involves specific operations – make-up of the coupling and cleaning of the tube end and threads from factory lubricant (Fig. 15).

Conventional removal of lubricant by solvent cleaning and mechanical treatment is often incomplete, resulting in localized blistering and coating failure, even though the coating remains intact over the rest of the pipe surface (Fig. 16). In practice, complete removal of lubricant is reliably achieved only by high-temperature treatment (furnace heating or laser-based heat treatment). Characteristic features of this type of failure are its localization within approximately 100 mm of the pipe end and the presence of large blisters caused by the lack of adhesion in this region.

In this case, overheating is associated with operation at temperatures above the wet-state *Tg* of the coating. Visually, this failure mode differs little from the normal degradation mechanism; however, the service life may be reduced by more than a factor of ten under elevated-temperature operation.

The thermokinetic characteristics of the internal coating were determined in order to assess the degree of cure of the powder-based material using differential scanning calorimetry (DSC). Tests were carried out on specimens before and after conditioning at 90 °C for 24 h to remove moisture from the coating. The corresponding results are summarized in the table, and the DSC thermograms of the coating material are presented in Fig. 17.

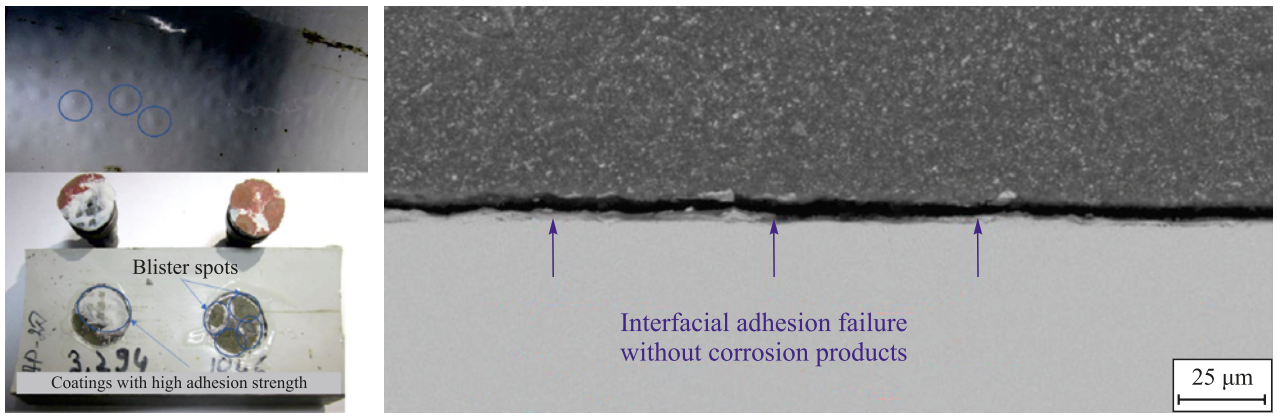

Fig. 14. Localized blistering of the coating after service (2nd degradation stage)

Рис. 14. Локальные вздутия покрытия после эксплуатации (2-я стадия разрушения)

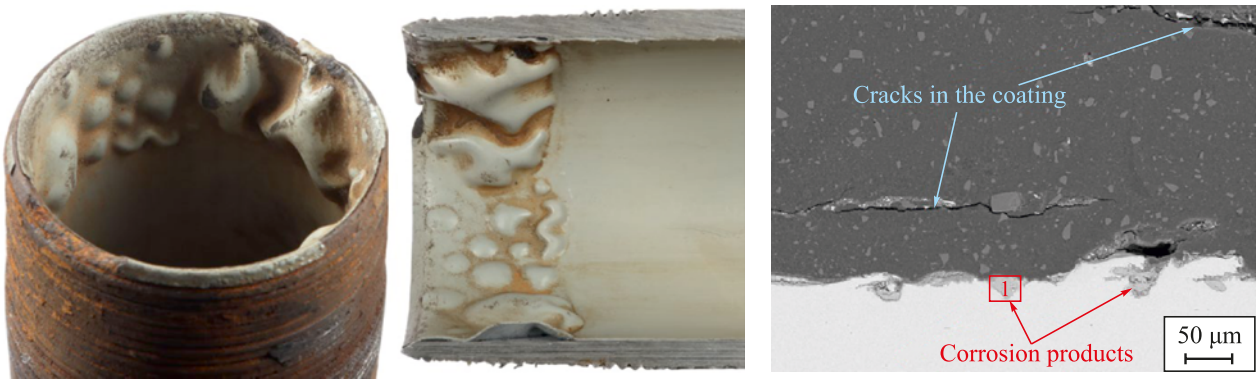

a *b*

Fig. 15. Appearance of damage to the internal coating of production tubing in the nipple region caused by improper surface preparation prior to abrasive blasting (***a***), and microstructure of the damaged zone showing areas with corrosion products and cracking within the coating (***b***)

Рис. 15. Внешний вид разрушения внутреннего покрытия НКТ в ниппельной части, обусловленного нарушением технологии подготовки поверхности перед дробеструйной обработкой (***a***), и микроструктура зоны разрушения с участками образования продуктов коррозии и трещин в покрытии (***b***)

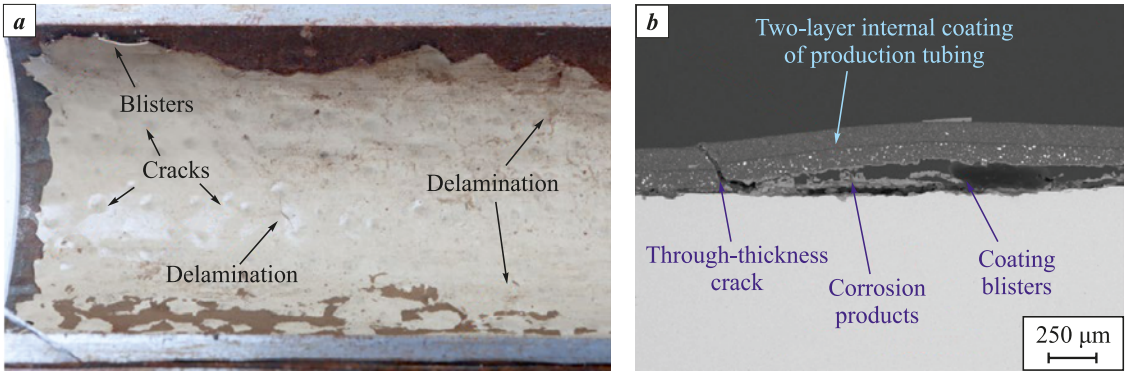

Fig. 16. Appearance of the internal coating of production tubing, Ø73×5.5 mm (after 512 days of service) (***a***), and the structure of the coating and corrosion products in the damaged region (***b***)

Рис. 16. Внешний вид внутреннего покрытия НКТ Ø73×5,5 мм (наработка 512 сут) (***a***) и структура покрытия и продуктов коррозии в области разрушения (***b***)

Based on the test results, the observed difference between the glass-transition temperatures determined in the first and second heating cycles for the as-received specimens is +13.8 and +12.7 °C, respectively, whereas after conditioning the difference decreases to +1.5 and +2.9 °C. This indicates that the coating absorbs moisture during service, which is a typical process for polymeric materials [58]. The absence of a curing peak in the DSC curves confirms that polymerization of the coating had been completed. The *Tg* values after conditioning (111–113 °C) match those of the as-received coating, demonstrating that no thermo-oxidative degradation occurred.

The third degradation stage is governed by the growth of corrosion products and depends on the diffusion coefficient and the corrosion resistance of the steel. This is a long-term process, and its duration is determined not only by the properties of the environment and the coating but also by the absence of mechanical loading on the internal coating, which could otherwise rupture the blister (Fig. 18).

The composition and morphology of the corrosion products correspond to the governing corrosion pro-

Results of determining the degree of coating curing

Результаты определения степени отверждения покрытия

Specimen	Tg_1, °C	Tg_2, °C	$\Delta Tg = Tg_2 - Tg_1$, °C
1 (as-received)	95,8	109,6	13,8
1 (conditioned)	107,8	109,3	1,5
2 (as-received)	99,8	112,5	12,7
2 (conditioned)	108,9	111,8	2,9
Requirements of GOST R 58346–2019			$-5 \le \Delta Tg \le +5$

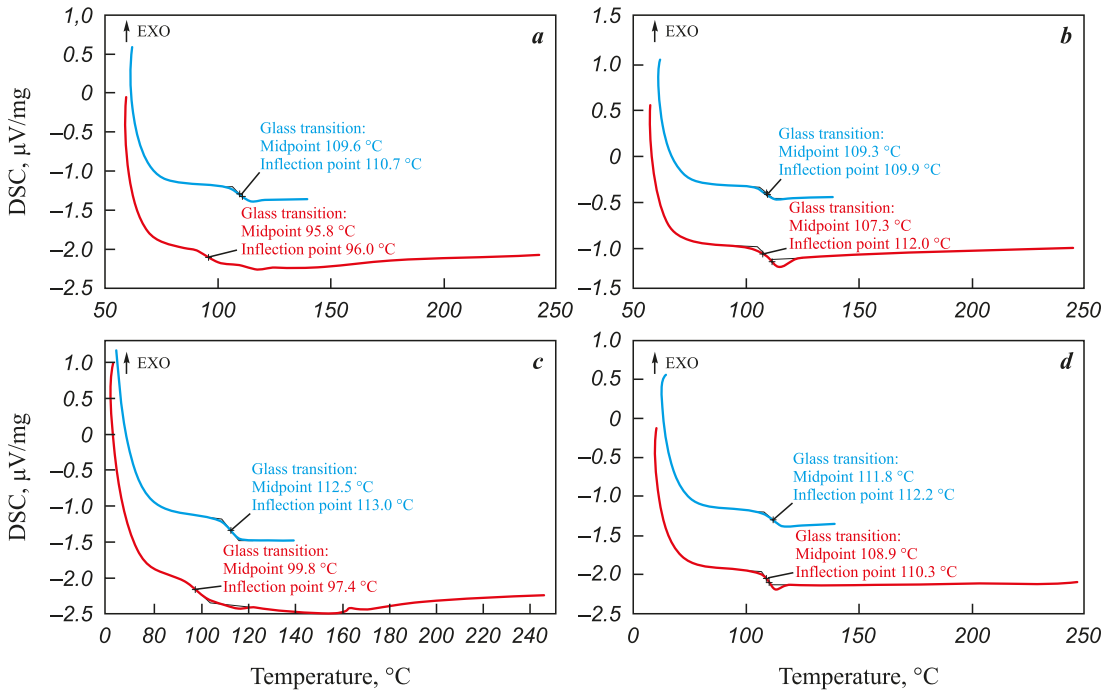

Fig. 17. DSC thermograms of the coating specimens:

a, ***c*** – specimens in the as-received state; ***b***, ***d*** – specimens after conditioning
Tg_1 – red curves, Tg_2 – blue curves

Рис. 17. Термограммы ДСК образцов покрытий

a, ***c*** – образцы в исходном состоянии; ***b***, ***d*** – образцы после кондиционирования
Tg_1 – красные кривые, Tg_2 – синие кривые

cesses. In CO_2 corrosion, the formation of $FeCO_3$ is observed; the carbonate inherits the steel microstructure because the reaction $Fe_3C + CO_2$ does not proceed, whereas α-Fe (ferrite) reacts with CO_2 to form iron carbonate (Fig. 19, *a*). Blister formation always precedes the growth of the corrosion-product layer, because this layer does not experience mechanical loading and cannot expand freely in the confined space. A corrosion-product layer enriched in chlorine is localized at the metal/corrosion-product interface (Fig. 19, *b*), which is characteristic of corrosion processes occurring in oilfield tubing. The identical composition and morphology of the corrosion products indicate the absence of selective diffusion or differences in the diffusion rates of individual components through the coating.

The height of coating blisters may reach ten times the coating thickness, which indicates minimal destructive changes and preservation of elasticity. In the authors' experience, failures preceded by significant plastic deformation have not been observed even after long service periods (over 10 years); therefore, adhesion loss and blister formation always proceed

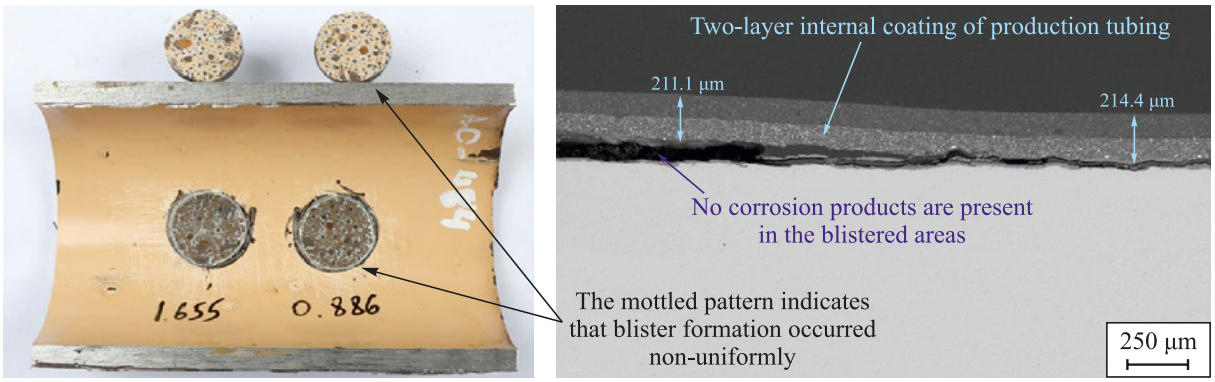

Fig. 18. A typical example of the appearance and structure of the coating at the third destruction stage

Рис. 18. Характерный пример внешнего вида и структуры покрытия на третьей стадии разрушения

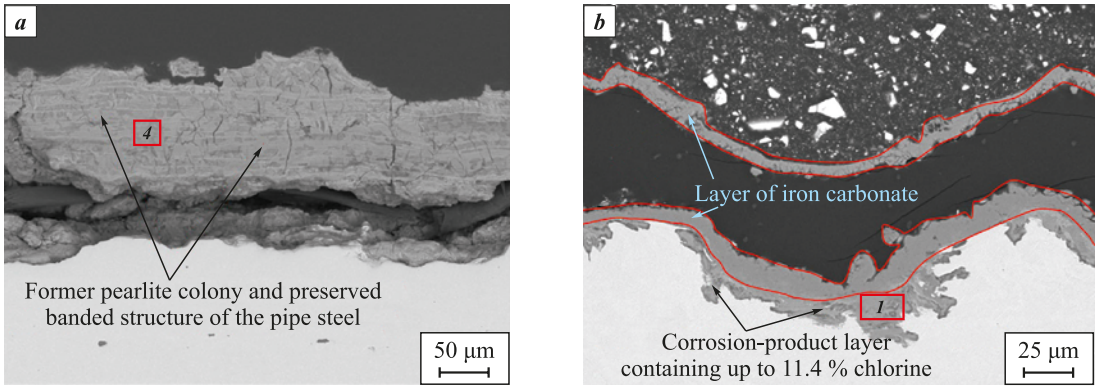

Element	O	Si	Fe	C	Na	Cr	Ca	Mn	V	Mg	Ni	Cu
wt. %	29.44	6.02	49.88	7.33	2.03	1.18	0.70	1.62	0.32	0.36	0.52	0.60

Element	C	O	Si	S	Cl	Cr	Mn	Fe
wt. %	5.57	24.80	0.78	0.13	11.46	0.56	0.82	55.87

Fig. 19. Structures of corrosion products beneath the coating: iron carbonate (***a***) and chlorine-rich corrosion products (***b***)
The red rectangle marks the area of SEM-EDS elemental analysis

Рис. 19. Структуры продуктов коррозии под покрытием – карбоната железа (***a***) и хлора (***b***)
Красным прямоугольником обозначена зона элементного анализа в режиме СЭМ-ЭДС

faster than aging processes accompanied by a reduction in ductility.

The fourth degradation stage is associated with the rapid development of through-thickness pits. If the coating has not been exposed to elevated temperatures, then by the time this stage is reached substantial destructive changes have often occurred, causing the coating to become brittle and fail easily (Fig. 20). In the presence of coating defects, corrosion damage is intensified for two reasons:

– formation of a galvanic couple in which the blister center acts as the anode, followed by accelerated corrosion after pit initiation and the formation of an additional cathode–anode pair;

– all corrosive activity is concentrated in a single local area; the medium contains no Fe^{2+} ions (typically released during corrosion of uncoated pipe), which otherwise act as inhibitors for corrosion processes. In such cases, the characteristic failure mode is through-wall pitting corrosion, whereas the coating remains intact on remote sections of the pipe (Fig. 21).

Conclusions

1. A comprehensive review of the degradation mechanisms of polymer coatings on metallic substrates has been conducted, including water diffusion and absorption within the polymer matrix, disruption of molecular interactions in the polymer network, adhesion loss and interfacial delamination, interfacial corrosion, cathodic delamination, blister formation, and erosion-driven damage.

2. It has been shown that the degradation of internal anticorrosion coatings in oil pipelines can be divided into four stages. At the first stage, water uptake and

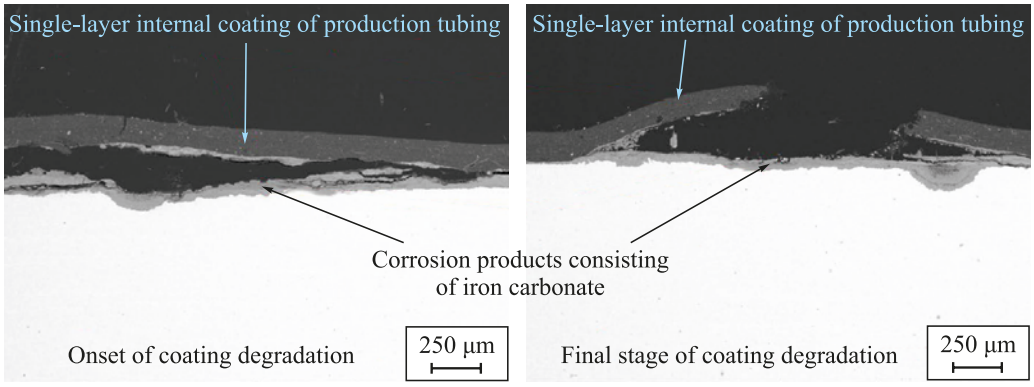

Fig. 20. Structure of a single-layer internal coating of production tubing, Ø73×5.5 mm, after 934 days of service, and morphology of corrosion products

Рис. 20. Структура однослойного внутреннего покрытия НКТ Ø73×5,5 мм с наработкой 934 дня, а также продуктов коррозии

Fig. 21. Consequences of operating a pipeline with a degraded internal coating

Рис. 21. Последствия эксплуатации трубопровода с разрушенным внутренним покрытием

diffusion of transported species occur throughout the coating thickness. This is the shortest stage and can be described using Fick's diffusion equation. During the second stage, interfacial adhesion is degraded; this is the longest and the life-limiting stage in coating performance. The third stage involves blister formation and the development of corrosion products at the metal–coating interface. At the final stage, the blister ruptures, followed by the onset of aggressive through-wall pitting corrosion.

3. Based on the analysis of the composition and morphology of corrosion products beneath the coating and their comparison with corrosion products formed on similar pipe steels operated under comparable conditions, it has been established that diffusion selectivity is absent. No substantial limitation on the transport of any specific corrosion-active species was observed.

4. It has been demonstrated that visual inspection alone cannot reliably identify the root cause of coating failure, because overheating by only a few degrees above the wet-state glass-transition temperature of the polymer may significantly contribute to degradation. Although such overheating does not intensify thermo-oxidative processes and is not detectable by DSC or FTIR analysis, its presence reduces the coating service life by approximately an order of magnitude.

References / Список литературы

1. Zhao L., Ren J., Dunne T. R., Cheng P. Surface engineering solutions for corrosion protection in CCUS tubular applications. In: *Surface engineering – foundational concepts, techniques and applications*. Wang J., Li C. (eds.). China: InTech, 2025. P. 1–27. http://dx.doi.org/10.5772/intechopen.1007112
2. Zargarnezhad H., Asselin E., Wong D., Lam C.C. A critical review of the time-dependent performance of polymeric pipeline coatings: Focus on hydration of epoxy-based coatings. *Polymers*. 2021;13(9):1517. https://doi.org/10.3390/polym13091517
3. Odette N.F., Soboyejo W. Failure mechanisms in pipeline epoxy coatings. *Advanced Materials Research*. 2016; 1132:366–384. https://doi.org/10.4028/www.scientific.net/AMR.1132.366
4. Zumelzu E., Ortega C., Rull F., Cabezas C. Degradation mechanism of metal–polymer composites undergoing electrolyte induced delamination. *Surface Engineering*. 2011;27(7):485–490. https://doi.org/10.1179/026708410X12687356948
5. Shreepathi S. Physicochemical parameters influencing the testing of cathodic delamination resistance of high build pigmented epoxy coating. *Progress in Organic Coatings*. 2016;90:438–447. https://doi.org/10.1016/j.porgcoat.2015.11.007
6. Nazarov A.P., Thierry D. Mechanism of the corrosion exfoliation of a polymer coating from a carbon steel. *Protection of Metals and Physical Chemistry of Surfaces*. 2009;45:735–745. https://doi.org/10.1134/S2070205109060173
7. Leidheiser Jr H., Wang W., Igetoft L. The mechanism for the cathodic delamination of organic coatings from a metal surface. *Progress in Organic Coatings*. 1983:11(1):19–40. https://doi.org/10.1016/0033-0655(83)80002-8
8. Watts J.F. Mechanistic aspects of the cathodic delamination of organic coatings. *The Journal of Adhesion*. 1989;31(1):73–85. https://doi.org/10.1080/00218468908048215
9. Kendig M., Addison R., Jeanjaquet S. The mechanism of cathodic disbonding of hydroxy-terminated polybutadiene on steel from acoustic microscopy and surface energy analysis. *Journal of the Electrochemical Society*. 1990;137(9):2690. https://doi.org/10.1149/1.2087011
10. Pud A.A., Shapoval G.S. Electrochemistry as the way to transform polymers. *Journal of Macromolecular Science, Part A*. 1995;32(sup1):629–638. https://doi.org/10.1080/10601329508018952
11. Kendig M., Mills D.J. An historical perspective on the corrosion protection by paints. *Progress in Organic Coatings*.

2017;102:53–59.
https://doi.org/10.1016/j.porgcoat.2016.04.044

12. Sander J., Manea V., Kirmaier L., Shchukin D., Skorb E. Anticorrosive coatings: Fundamental and new concepts. Hannover, Germany: Vincentz Network, 2014. 216 p. https://doi.org/10.1515/9783748602194
13. Haji-Ghassemi M., Gowers K.R., Cottis R. Hydrogen permeation measurement on lacquer coated mild steel under cathodic polarisation in sodium chloride solution. *Surface Coatings International*. 1992;75:277–80. https://doi.org/10.1038/s41598-022-21941-7
14. Cupertino-Malheiros L., Duportal,M., Hageman T., Zafra A., Martínez-Pañeda E. Hydrogen uptake kinetics of cathodic polarized metals in aqueous electrolytes. *Corrosion Science*. 2024;231:111959. https://doi.org/10.1016/j.corsci.2024.111959
15. Petrunin M.A., Maksaeva L.B., Gladkikh N.A., Yurasova T.A., Maleeva M.A., Ignatenko V. E. Cathodic delamination of polymer coatings from metals. Mechanism and prevention methods. A review. *International Journal of Corrosion and Scale Inhibition*. 2024;10(1):1–28. https://doi.org/10.17675/2305-6894-2021-10-1-1
16. Nazarov A., Thierry D. Application of Scanning Kelvin probe in the study of protective paints. *Frontiers in Materials*. 2019;6:192. https://doi.org/10.3389/fmats.2019.00192
17. Funke W. Blistering of paint films and filiform corrosion. *Progress in Organic coatings*. 1981;9(1):29–46. https://doi.org/10.1016/0033-0655(81)80014-3
18. Sabet-Bokati K., Plucknett K. Water-induced failure in polymer coatings: Mechanisms, impacts and mitigation strategies – A comprehensive review. *Polymer Degradation and Stability*. 2024;230:111058. https://doi.org/10.1016/j.polymdegradstab.2024.111058
19. Cristoforetti A., Izquierdo J., Souto R.M., Deflorian F., Fedel M., Rossi, S. In-situ measurement of electrochemical activity related to filiform corrosion in organic coated steel by scanning vibrating electrode technique and scanning micropotentiometry. *Corrosion Science*. 2024; 227:111669. https://doi.org/10.1016/j.corsci.2023.111669
20. Liu Y., Wang J., Liu L., Li Y., Wang F. Study of the failure mechanism of an epoxy coating system under high hydrostatic pressure. *Corrosion Science*. 2013;74:59–70. https://doi.org/10.1016/j.corsci.2013.04.012
21. Knudsen O.O., Bjørgum A., Kvernbråten, A.K. Internal coating of multiphase pipelines-requirements for the coating. In: Corrosion 2010 (March 14–18, 2010). San Antonio, Texas: NACE CORROSION, 2010. 10004 p.
22. Zargarnezhad H., Wong D., Lam C.C., Asselin E. Long-term performance of epoxy-based coatings: Hydrothermal exposure. *Progress in Organic Coatings*. 2024; 196:108697. https://doi.org/10.1016/j.porgcoat.2024.108697
23. Rajagopalan N., Weinell C.E., Dam-Johansen K., Kiil S. Degradation mechanisms of amine-cured epoxy novolac and bisphenol F resins under conditions of high pressures and high temperatures. *Progress in Organic Coatings*. 2021;156:106268. https://doi.org/10.1016/j.porgcoat.2021.106268
24. Rajagopalan N., Weinell C.E., Dam-Johansen K., Kiil S. Influence of CO_2 at HPHT conditions on the properties and failures of an amine-cured epoxy novolac coating. *Industrial & Engineering Chemistry Research*. 2021;60(41):14768–14778. https://pubs.acs.org/doi/10.1021/acs.iecr.1c02713
25. Rajagopalan N., Olsen M., Larsen T.S., Fjælberg T.J., Weinell C.E., Kiil S. Protective mechanisms of siloxane-modified epoxy novolac coatings at high-pressure, high-temperature conditions. *ACS omega*. 2024;9(28):30675–30684. https://doi.org/10.1021/acsomega.4c02986
26. Yang C., Xing X., Li Z., Zhang S. A comprehensive review on water diffusion in polymers focusing on the polymer–metal interface combination. *Polymers*. 2020;12(1):138. https://doi.org/10.3390/polym12010138
27. Bratasyuk N.A., Latyshev A.V., Zuev V.V. Water in epoxy coatings: Basic principles of interaction with polymer matrix and the influence on coating life cycle. *Coatings*. 2023;14(1):54. https://doi.org/10.3390/coatings14010054
28. Nogueira P., Ramirez C., Torres A., Abad M.J., Cano J., Lopez J., López-Bueno I., Barral L. Effect of water sorption on the structure and mechanical properties of an epoxy resin system. *Journal of Applied Polymer Science*. 2001;80(1):71–80. https://doi.org/10.1002/1097-4628(20010404)80:1<71::AID-APP1077>3.0.CO;2-H
29. Chiang M.Y., Fernandez-Garcia M. Relation of swelling and Tg depression to the apparent free volume of a particle – filled, epoxy – based adhesive. *Journal of Applied Polymer Science*. 2023;87(9):1436–1444. https://pubs.acs.org/doi/10.1002/app.11576
30. Luo S., Leisen J., Wong C.P. Study on mobility of water and polymer chain in epoxy and its influence on adhesion. *Journal of Applied Polymer Science*. 2002;85(1):1–8. https://doi.org/10.1002/app.10473
31. Mallarino S., Renaud A., Trinh D., Touzain S. The role of internal stresses, temperature, and water on the swelling of pigmented epoxy systems during hygrothermal aging. *Journal of Applied Polymer Science*. 2022; 139(46):53162. https://doi.org/10.1002/app.53162
32. Alessi S., Toscano A., Pitarresi G., Dispenza C., Spadaro G. Water diffusion and swelling stresses in ionizing radiation cured epoxy matrices. *Polymer Degradation and Stability*. 2017;144:137–145. https://doi.org/10.1016/j.polymdegradstab.2017.08.009
33. Croll S.G. Stress and embrittlement in organic coatings during general weathering exposure: A review. *Progress in Organic Coatings*. 2022;172:107085. https://doi.org/10.1016/j.porgcoat.2022.107085
34. Abdelkader A.F., White J.R. Curing characteristics and internal stresses in epoxy coatings: Effect of crosslinking agent. *Journal of Materials Science*. 2005;40:1843–1854. https://doi.org/10.1007/s10853-005-1203-9
35. Krauklis A.E., Gagani A.I., Echtermeyer A.T. Long-term hydrolytic degradation of the sizing-rich composite interphase. *Coatings*. 2019;9(4):263. https://doi.org/10.3390/coatings9040263
36. Capiel G., Uicich J., Fasce D., Montemartini P.E. Diffusion and hydrolysis effects during water aging on an

epoxy-anhydride system. *Polymer Degradation and Stability*. 2018;153:165–171. https://doi.org/10.1016/j.polymdegradstab.2018.04.030

37. Göpferich A. Mechanisms of polymer degradation and erosion. *Biomaterials*. 1996;17(2): 103–114. https://doi.org/10.1016/0142-9612(96)85755-3
38. Grujicic M., Sellappan V., Omar M.A., Seyr N., Obieglo A., Erdmann M., Holzleitner J. An overview of the polymer-to-metal direct-adhesion hybrid technologies for load-bearing automotive components. *Journal of Materials Processing Technology*. 2008;197(1-3):363–373. https://doi.org/10.1016/j.jmatprotec.2007.06.058
39. Schmidt R.G., Bell J.P. Epoxy adhesion to metals. Epoxy Resins and Composites II. *Advances in Polymer Science*. 2005;72:33–71. https://doi.org/10.1007/BFb0017914
40. Posner R., Ozcan O., Grundmeier G. Water and ions at polymer/metal interfaces. *Design of Adhesive Joints Under Humid Conditions. Advanced Structured Materials*. 2013;25:21–52. https://doi.org/10.1007/978-3-642-37614-6_2
41. Fan X., Zhang G.Q., Van Driel W.D., Ernst L.J. Interfacial delamination mechanisms during soldering reflow with moisture preconditioning. *IEEE Transactions on Components and Packaging Technologies*. 2008;31(2):252–259. https://doi.org/10.1109/TCAPT.2008.921629
42. Chen F., Jin Z., Wang E., Wang L., Jiang Y., Guo P., Gao X., He X. Relationship model between surface strain of concrete and expansion force of reinforcement rust. *Scientific Reports*. 2021;11:4208. https://doi.org/10.1038/s41598-021-83376-w
43. Saarimaa V., Virtanen M., Laihinen T., Laurila K., Väisänen P. Blistering of color coated steel: Use of broad ion beam milling to examine degradation phenomena and coating defects. *Surface and Coatings Technology*. 2022;448:128913. https://doi.org/10.1016/j.surfcoat.2022.128913
44. Sørensen P.A., Kiil S., Dam-Johansen K., Weinell C.E. Influence of substrate topography on cathodic delamination of anticorrosive coatings. *Progress in Organic Coatings*. 2009;64(2-3):142–149. https://doi.org/10.1016/j.porgcoat.2008.08.027
45. Sørensen P.A., Dam-Johansen K., Weinell C.E., Kiil S. Cathodic delamination of seawater-immersed anticorrosive coatings: Mapping of parameters affecting the rate. *Progress in Organic Coatings*. 2010;68(4):283–292. https://doi.org/10.1016/j.porgcoat.2010.03.012
46. Jorcin J.B., Aragon E., Merlatti C., Pébère N. Delaminated areas beneath organic coating: A local electrochemical impedance approach. *Corrosion Science*. 2006;48(7):1779–1790. https://doi.org/10.1016/j.corsci.2005.05.031
47. Yang X.F., Tallman D.E., Bierwagen G.P., Croll S.G., Rohlik S. Blistering and degradation of polyurethane coatings under different accelerated weathering tests. *Polymer degradation and stability*. 2002;77(1):103–109. https://doi.org/10.1016/S0141-3910(02)00085-X
48. Kotb Y., Serfass C.M., Cagnard A., Houston K.R., Khan S.A., Hsiao L.C., Velev O.D. Molecular structure effects on the mechanisms of corrosion protection of model epoxy coatings on metals. *Materials Chemistry Frontiers*. 2023;7(2):274–286. https://doi.org/10.1039/D2QM01045C
49. Prosek T., Nazarov A., Olivier M.G., Vandermiers C., Koberg D., Thierry D. The role of stress and topcoat properties in blistering of coil-coated materials. *Progress in Organic Coatings*. 2010;68(4):328–333. https://doi.org/10.1016/j.porgcoat.2010.03.003
50. Effendy S., Zhou T., Eichman H., Petr M., Bazant M.Z. Blistering failure of elastic coatings with applications to corrosion resistance. *Soft Matter*. 2021;17(11): 9480–9498. https://doi.org/10.1039/D1SM00986A
51. Hoseinpoor M., Prošek T., Mallégol J. Mechanism of blistering of deformed coil coated sheets in marine climate. *Corrosion Science*. 2023;212:110962. https://doi.org/10.1016/j.corsci.2023.110962
52. Bi H., Sykes J. Cathodic disbonding of an unpigmented epoxy coating on mild steel under semi-and full-immersion conditions. *Corrosion Science*. 2011;53(10):3416–3425. https://doi.org/10.1016/j.corsci.2011.06.021
53. Meng F., Liu L., Liu E., Zheng H., Liu R., Cui Y., Wang F. Synergistic effects of fluid flow and hydrostatic pressure on the degradation of epoxy coating in the simulated deep-sea environment. *Progress in Organic Coatings*. 2021;159:106449. https://doi.org/10.1016/j.porgcoat.2021.106449
54. Zhou Q., Wang Y., Bierwagen G.P. Flow-accelerated coating degradation: Influence of the composition of working fluids. In: Corrosion 2012 (March 11–14, 2012). Salt Lake City, UT: NACE INTERNATIONAL; 2012. C2012-01656 p.
55. Wood R.J. Tribo-corrosion of coatings: A review. *Journal of Physics D: Applied Physics*. 2007;40(18):5502. https://doi.org/10.1088/0022-3727/40/18/S10
56. Wang D., Sikora E., Shaw B. A study of the effects of filler particles on the degradation mechanisms of powder epoxy novolac coating systems under corrosion and erosion. *Progress in Organic Coatings*. 2018;121:97–104. https://doi.org/10.1016/j.porgcoat.2018.04.026
57. Yudin P.E. Functional coatings of submersible oilfield equipment for protection against corrosion, asphalt, resin, paraffin and salt deposits: Review. *Powder Metallurgy and Functional Coatings*. 2025;19(1):58–74. https://doi.org/10.17073/1997-308X-2025-1-58-74

    Юдин П.Е. Функциональные покрытия погружного нефтепромыслового оборудования для защиты от коррозии, асфальтосмолопарафиновых и солевых отложений: Обзор. *Известия вузов. Порошковая металлургия и функциональные покрытия*. 2025; 19(1):58–74. https://doi.org/10.17073/1997-308X-2025-1-58-74
58. Bogatov M.V., Yudin P.E., Maidan D.A. Influence of the water absorption process on the physical and mechanical properties of the free coating film. *Neftegazovoe delo*. 2025;23(1):77–90. (In Russ.). https://doi.org/10.17122/ngdelo-2025-1-77-90

    Богатов М.В., Юдин П.Е., Майдан Д.А. Влияние процесса водопоглощения на физико-механические свойства свободной пленки покрытия. *Нефтегазовое дело*. 2025;23(1):77–90. https://doi.org/10.17122/ngdelo-2025-1-77-90

Information about the Authors

Pavel E. Yudin – Cand. Sci. (Eng.), Associate Professor of the Department of metal science, powder metallurgy, nanomaterials of Samara State Technical University; Director of Science of Samara Scientific and Production Center, LLC
ORCID: 0000-0002-4517-3744
E-mail: yudin@npcsamara.ru

Aleksandr S. Lozhkomoev – Dr. Sci. (Eng.), Leading Researcher of Institute of Strength Physics and Materials Science of SB RAS
ORCID: 0000-0002-1564-0858
E-mail: asl@ispms.ru

Сведения об авторах

Павел Евгеньевич Юдин – к.т.н., доцент кафедры «Металловедение, порошковая металлургия, наноматериалы» Самарского государственного технического университета; директор по науке ООО «НПЦ «Самара»
ORCID: 0000-0002-4517-3744
E-mail: yudin@npcsamara.ru

Александр Сергеевич Ложкомоев – д.т.н., вед. науч. сотрудник Института физики прочности и материаловедения СО РАН
ORCID: 0000-0002-1564-0858
E-mail: asl@ispms.ru

Contribution of the Authors

P. E. Yudin – development of the main concept, formulation of the aim and objectives of the study, experimental testing of specimens, analysis of the research results, and formulation of the conclusions.
A. S. Lozhkomoev – preparation of the manuscript text and editorial revision.

Вклад авторов

П. Е. Юдин – формирование основной концепции, постановка цели и задачи исследования, проведение испытаний образцов, анализ результатов исследований, формулировка выводов.
А. С. Ложкомоев – подготовка текста статьи, корректировка текста.

Received 14.04.2025
Revised 20.04.2025
Accepted 21.04.2025

Статья поступила 14.04.2025 г.
Доработана 20.04.2025 г.
Принята к публикации 21.04.2025 г.

Зарегистрирован Федеральной службой по надзору
в сфере связи, информационных технологий
и массовых коммуникаций.
Свидетельство о регистрации ПИ № ФС77-79230

Журнал распространяется агентством «Урал-Пресс»
Подписной индекс: 80752 (печатная версия)
05108 (электронная версия)